Ultrafast dynamics of graphite oxide and semiconductor saturable absorber

Dissertation zur Erlangung des Doktorgrades

des Fachbereiches Physik

der Universität Hamburg

vorgelegt von

Amul Shinde

aus

Saswad, INDIA

Hamburg

2018

Gutachter der Dissertation:	Prof. Dr. Nils Huse
	Prof. Dr. R. J. Dwayne Miller
Gutachter der Disputation:	Prof. Dr. Michael Rübhausen
	Prof. Dr. Gabriel Bester
	Dr. Oliver Mücke
Datum der Disputation:	12.04.2018
Vorsitzender des Fach-Promotionsausscuhsses:	Prof. Dr. Michael Rübhausen
Leiter des Fachbereiches Physik:	Prof. Dr. Michael Potthof
Dekan der Fakultät für Mathematik, Informatik und Naturwissenschaften:	Prof. Dr. Heinrich Graener

Zusammenfassung

Im zwanzigsten Jahrhundert wurden ultraschnelle Prozesse, welche in der Natur vorkommen zugänglich. Dies ist Dank der Entwicklung des Lasers 1960 und darauffolgende Verbesserungen der Pulslänge von Nanosekunden zu Femtosekunden möglich geworden. Einige Beispiele, die auf diesen kurzen Zeitskalen Dynamiken zeigen sind Wasserstoffbrücken, Proteinstrukturen, intra- oder intermolekularer Energie-Austausch von Vibrationsmoden und chemische Austauschprozesse in Molekülen. Solche Prozesse können mit Strahlung im mittleren Infrarot (MIR) untersucht werden, die durch optisch-parametrische Verstärkung (optical parametric amplification, OPA) und Differenzfrequenzmischung (DFG) erzeugt werden. Dieser Wellenlängenbereich erstreckt sich von ca. 2-20 µm. Zwei solcher OPAs wurden für Zwei-Farben-Spektroskopie und für zukünftige 2D-Infrarotspektroskopie aufgebaut. Als Pumplaser der OPAs wurde ein verstärkter Titan:Saphir Laser mit einer Zentralwellenlänge von 800 nm und 100 fs Pulsdauer genutzt. Die erzeugte MIR-Strahlung besitzt eine Pulsenergie von 0.5 bis 2 µJ und eine Pulslänge von 100 bis 150 fs. In dem Pump-Tast-Spektrometer, mit dem frequenzaufgelöste transiente Differenzspektren gemessen werden können, wurden größtenteils reflektive Optiken benutzt. Ein BaF_2-Keil wurde verwendet, um Tast und Referenzpuls zu erhalten. Um das jetzige Spektrometer in eine 2D Konfiguration zu überführen, muss nur ein Block eingesetzt werden, auf dem ein Mach-Zehnder-Interferometer aufgebaut ist. Im Pumpstrahlengang eingesetzt, ergibt dies zwei kollineare Pumpstrahlen. Die Software für die Verschiebestufe, den Monochromator und die Datenakquisition wurden ebenfalls programmiert.

Mit diesem Spektrometer, der im MIR operiert, wurden Ladungsträger und Vibrationsdynamiken von Graphitoxid (GO) untersucht. Dieses geschichtete Material ist hy-

groskopisch, hydrophil, und Wassermoleküle können sich zwischen den Lagen befinden. Lineare Infrarot-Absorptionsspektren zeigen, dass sich während des Spülens der Probekammer mit trockener Luft, die Wasserabsorptionsbande verkleinert, was durch Verlust der Wassermoleküle aus der Membran erklärt werden kann. Dadurch kommt die C=C Streckungsmode (1550-1610 cm^{-1}) zum Vorschein. Dies wurde mit Pump-Tast-Messungen weiter untersucht. Es wurden verschieden Pump-Tast-Messungen an der $\sim$14 µm dicken Membran mit Pumpwellenlängen vom UV bis ins IR durchgeführt. Die Tastwellenlänge lag im IR Bereich. In den transienten Absorptionsspektren konnten bei Wellenzahlen zwischen 1573 und 1670 cm^{-1} Signale identifiziert werden, die der C=C Streckschwingung und der Enol-Karbonyl-Streckschwingung (C=COHCH3) entsprechen. Die erzeugten Ladungsträger sind nach den jetzigen Messungen in ihrem Relaxationsverhalten weitestgehend unabhängig von der Pumpwellenlänge. Es scheint so, als ob graphenartige Domänen der Membran für die ultraschnelle Antwort des Systems zuständig sind und die funktionellen Gruppen Energieübertrag und Relaxationsprozesse beeinflussen. Ein abgeändertes Zwei-Temperatur-Modell wurde zur Kurvenanpassung verwendet, bei dem drei Zeitkonstanten jeweils der Elektron-Elektron und der Elektron-Phonon-Streuung sowie der Ladungsträger-Rekombination über Fehlstellen zugeordnet werden können. Die Interpretation sollte mit Vorbehalt betrachtet werden, da sie in der Literatur debattiert wird.

Bei einem anderen Experiment wurde die Relaxationsdynamik eines Halbleiters, um genauer zu sein, eines sättigbaren Absorber-Spiegels (saturable absorber mirror, SESAM), angeschaut, der von unseren Projektpartnern als Endspiegel in einem passiv-modengekoppelten Oszillator benutzt werden sollte. Die ausgekoppelte Wellenlänge sollte knapp unter 2 µm liegen und mittels eines Ho:YLF-Kirstalls als Gain-Material genutzt werden. Die Untersuchung zeigte, dass die Relaxationszeiten des SESAM (bei 130 fs liegend) nicht zur Pulslänge im Resonator (500 fs betragend) passt, die aufgrund der geringen Bandbreite des Gain-Materials begrenzt ist. Daher ist der hier verwendete SESAM nicht für die Verwendung als Auskoppelspiegel in einem Ho:YLF Resonator geeignet.

Abstract

In the 20^{th} century ultrafast processes became accessible for scientific studies. This was due to the laser development in 1960 and subsequent development in its pulse duration from nanoseconds to femtoseconds. The hydrogen bond dynamics, the protein structural dynamics, the intramolecular and/or intermolecular coupling of vibrational modes and chemical exchange processes in molecules are some examples to uncover reactions pathways happening at ultrafast time scales. To study such processes, mid-infrared light sources of capability of tuning the wavelength from 2-20 μm spectral range have been developed using the combination of optical parametric amplification (OPA) and difference frequency mixing (DFG) techniques. Two of such OPAs with DFG stages have been built for two-color pump-probe and future two-dimensional infrared experiments. The output of a Ti:sapphire amplifier at 800 nm, 100 fs pulse duration was used for the generation of signal and idler pulses in OPAs using a nonlinear BBO crystal. These signal and idler pulses were then further used for mid-infrared light generation using the DFG stage in a nonlinear $AgGaS_2$ crystal. The mid-infrared light pulses generated in the frequency range of 2-20 μm, having energies in the range of 0.5-2 μJ and pulse durations of 100-150 fs. The pump-probe spectrometer to measure frequency resolved transient absorption changes in samples have been developed using reflective optics, except for a BaF_2 wedge, which is used to generate probe and reference pulses. This spectrometer is designed in a way so that it could be transformed into a two dimensional infrared spectrometer in the future by adding one compact block in the pump beam path, which hosts a Mach-Zehnder interferometer to generate two collinear pump beams. The software to control the delay stage, monochromator and data acquisition has also been developed.

We have made an attempt to study the carrier and phonon dynamics of graphite oxide (GO) using the home-built mid-infrared light sources and pump-probe spectrometer. Graphite oxide is a layered material, is hygroscopic and hydrophilic in nature. The water molecules are intercalated between the graphene oxide sheets. The linear differential infrared absorption measurements have shown, that the water absorption bands diminish while purging the sample with dry air, which is an indication of some loss of water molecules and eventually resulting into the appearance of the prominent C=C stretching band hidden under a broad water bending peak (1550-1610 cm^{-1}). However, when the linear infrared spectrum measured in the pump-probe spectrometer which was heavily purged with dry air, the C=C stretching mode (1570 cm^{-1}) becomes more pronounced and the water bending peak almost vanished. Time resolved single and two color pump-probe measurements have been performed to provide insights into the interplay of in plane stretching vibrations of C=C and enone bond motifs, the carrier and phonon relaxation mechanism, and intercalated water dynamics of graphite oxide. Four different pump-probe measurements were performed by exciting the 14 μm thick graphite oxide membrane with femtosecond pulses from the UV to the mid-infrared and probed the sample response in the mid-infrared spectral range.

In the transient absorption spectrum, we observed peculiar signatures at 1573 cm^{-1} and at 1670 cm^{-1} which are respectively indication of the C=C stretching and enone's carbonyl (C=COHCH3) stretching band vibrations of the graphite oxide. We have observed that the carrier dynamics are largely independent of pump frequency. It appears that the graphene-like domains majorly influences the ultrafast optical response while the functional groups may contribute to energy transfer or loss mechanisms in the carrier relaxation processes. After line shape analysis of the transient absorption curves, we found stiffening in C=C stretching vibration which is responsible factor for reducing carrier-phonon coupling. It leads to the renormalization of the C=C stretching vibration energy. We used a modified two-temperature model to fit the time traces, the shortest two time constants assigned to carrier-phonon and phonon-phonon scattering, respectively, and a third time constant of tens of picoseconds for population of mid-gap states. It should be noted that these assignments are still a subject of ongoing debates.

In another ultrafast pump-probe experiment, we studied the carrier relaxation dynamics of a specific semiconductor saturable absorber mirror (SESAM) which was used by our collaborator as one of the cavity end mirrors to generate passively mode locked output at 2 μm wavelength from a Ho:YLF laser cavity. The carrier relaxation dynamics helped us to decipher the problems behind the unstable performance of the Ho:YLF laser cavity to generate the mode-locked output. We found that the carriers relaxation happens at fast time scales of 130 fs which is much faster than the intra-cavity pulse duration supported by the narrow gain bandwidth of Ho:YLF laser medium which typically supports pulses of 500 fs. Thus, it makes this SESAM type unsuitable to deliver stabilized mode locked pulses from the Ho:YLF laser cavity.

Publication List

The work of this thesis will lead to the following three publications in the near future.

1. Graphite-like dynamical behavior of graphite oxide. Amul Shinde, Katrin Adamczyk, Christoph Testud and Nils Huse (*Manuscript under preparation*).

2. Excitation-dependent charge carrier and phonon relaxation in graphite oxide. Katrin Adamczyk, Amul Shinde, Christoph Testud and Nils Huse (*Manuscript will be prepared soon*).

3. Dynamical modification of carrier relaxation in graphite oxide by resonant excitation of intercalated water. Christoph Testud, Amul Shinde, Katrin Adamczyk and Nils Huse (*Manuscript will be prepared soon*).

Eidesstattliche Versicherung / Declaration on oath

Hiermit versichere ich an Eides statt, die vorliegende Dissertationsschrift selbst verfasst und keine anderen als die angegebenen Hilfsmittel und Quellen benutzt zu haben.

Die eingereichte schriftliche Fassung entspricht der auf dem elektronischen Speichermedium.

Die Dissertation wurde in der vorgelegten oder einer ähnlichen Form nicht schon einmal in einem früheren Promotionsverfahren angenommen oder als ungenügend beurteilt.

Hamburg, den

Unterschrift der Doktorandin / des Doktoranden

Acknowledgment

First and foremost, I am highly indebted to my thesis adviser Prof. Dr. Nils Huse for encouraging and enlightening me with the field of optics, lasers, and ultrafast molecular dynamics. I had the honor to be the first member of his research group. He has been very keen to bring the precision in the work, specially in optics designs and autocad drawings that grossly influenced me to take note of every single thing while doing my work. I owe him a deep sense of gratitude for being very friendly throughout my PhD years and discussing any range of topics from science, philosophy, sports to politics.

I would like to thank Mrs. Ute Kaluza and Ms. Nadja Bardenheuer of Max Planck Institute for Structure and Dynamics of Matter, Mrs. Sylke Strien of Hamburg University, and Mrs. Steffi Killough, Mrs. Nicole Kosian, Mrs. Gabriella Kirstein and Mrs. Anna Kazakova of Guest Services, International office, DESY, Hamburg for smoothing administrative procedures to get my induction into the institute and to provide services to help me out in getting resident permit, health insurance and housing facilities.

The thesis work had began with the building optical setups in an empty laser laboratory. During the initial two years of PhD days, Hamburg university machine workshop employees helped at a greater length. Without their support, it could have taken few more months to start the very first time resolved pump-probe measurement. Particularly, I am grateful to Mr. Stephan Fleig and Mr. Frank Jonas for providing duly needed technical support.

I would like to acknowledge and thanks, members of the UMoDyne Group; Katrin Adamczyk, Christoph Testud, Miguel Ochmann, Abid Hussain, Matthias Ruppert, Inga von Ahnen, Stephen Niebling, Niko Höppel and Nazanin Davoudi for sharing knowledge,

advice and wonderful discussions on various topics and maintaining a friendly environment.

I appreciate the efforts of administrative members of PIER and CUI graduate schools and thanks them for arranging myriads of courses and for providing support whenever required.

I would take an opportunity to express the feeling of gratitude towards my friends at DESY campus and Indian community in Hamburg. I am honored to have friends like Alessandra Picchiotti, Andreas Rossos, Maria Katsiaflaska, Masaki Hada, Régis Gengler, Daniel Badali, Ling Ren, Khalid Siddiqui, Julian Hirscht, Günther Kassier, Krishna Murari, Pankaj Mishra, Santosh Jangam, Indranil Sarkar, Udya Kumar Tiruttani, Rashmi Singla, Moon Chatterjee, Sumit Tripathi, Gopinath Muruganandam, Balakumaar Baskaran, Shirin Gangal, Anand Kamlapure, Vijay Singh, and Ganjedra Kumar Sahoo who's support and advice I value a lot.

I wish to thank my parents and family members for providing endless love, support and encouragement.

Finally, I would like to thank Prof. Dr. R.J. Dwayne Miller for yearly evaluating the progress of my thesis work and genuinely providing pieces of advice on the state of the work.

Contents

List of Figures

List of Tables

Chapter 1

Introduction

Till date, there have many spectroscopies been developed to explore atomic-scale phenomena. Techniques such as electron diffraction, X-ray diffraction, UV-visible, and infrared absorption spectroscopies are examples of some of them. With an electron diffraction technique, atomic-scale structural dynamics in condensed matter can be investigated with the easily available 100 fs time resolution electron pulses [1]. X-ray spectroscopy has many variants such as X-ray absorption spectroscopy (XAS), X-ray emission spectroscopy (XES), Auger emission spectroscopy (AES), X-ray fluorescence spectroscopy (XFS), electron spectroscopy for chemical analysis (ESCA) and X-ray diffraction spectroscopy (XDS). Some of these X-ray spectroscopic techniques are very feasible to interrogate biological samples to explore the dynamic structures of proteins during processes such as unfolding or refolding [2,3], fast proton or electron transfer [4], light induced conformational changes [5], and enzyme activities [6]. The X-ray spectroscopy is also used in the detection of local electronic structure [7] and temporal evolution of the system under investigation [8]. UV-visible absorption is commonly used to probe the excited state intramolecular proton transfer, photodissociation and relaxation processes [9, 10]. Ultrafast infrared spectroscopy is widely used to study vibrational population dynamics [11], coherent wavepacket generation in anharmonically coupled low-frequency modes [12], hydrogen bond dynamics [13], vibrational energy relaxation [14] and many other infrared active phenomena in molecules [15]. Very often, a combination of different frequencies of

light pulses are used to detect ultrafast phenomena [16].

To unravel the ultrafast processes exemplified above at the fundamental time-scales requires light sources which are able to generate extremely short 10-100 fs light pulses. The invention of the mode-locked laser has resolved this barrier in the development of ultrafast spectroscopy. The first laser was invented by Theodore Maiman in 1960 [17], since then there is an extensive improvement in the time resolution, from nanosecond to few femtosecond of the laser pulses directly obtained from the laser oscillator in the visible and near-infrared spectral region [18]. In 2001, Hentschel et al. reported the first attosecond light source of 250 attosecond time resolution in the ultraviolet spectral region. They had generated attosecond light pulses by focusing few optical cycle visible light laser pulses onto a neon gas jet [19]. The light pulses of femtosecond temporal resolution are useful in the investigation of structural dynamics. However, the attosecond pulses directly access electronic motions in an atom. The temporal pulse duration and center frequency of the pulse determines their application in telecommunication and ultrafast spectroscopy.

The 1999 Nobel prize in chemistry was awarded to Prof. Ahmed H. Zewail for his research on the "transition states of chemical reactions using femtosecond spectroscopy". Conventional linear optical spectroscopies probe atomic or molecular level transitions which are termed as static linear interactions. The core idea of femtosecond spectroscopy is to study dynamics instead of static states [20]. Dynamics often include nuclear wavepackets which are defined as a coherent superposition of a set of stationary wavefunctions of an atomic or molecular systems. The minimum temporal width of a wavepacket is inversely proportional to its spectral bandwidth $\Delta t \cdot \Delta \omega \geq 1$.

During the initial period of this thesis, the very first idea was to explore the photoreduction dynamics of graphene oxide suspended in water using a UV pump and MIR probe technique inspired by the photoreduction mechanism of graphene oxide proposed by Gengler et al. [21]. We probed the epoxy functional group at 1090 cm^{-1} to monitor its evolution with change in a pump-probe delay. But, we could not detect any change in the pump-probe signal. However, it sparked an idea to study dynamics of charge carriers and the role of water molecules intercalated in graphene oxide layers. Due to its oxygen functionalities, graphene oxide is a hydrophilic and hygroscopic in nature, which incorpo-

rates water molecules in its lamellar structure. The fluctuating hydrogen bond network of water molecules in bulk water is different compared to intercalated water molecules, due to its nanoconfinement and interactions with graphene oxide functional groups [22, 23]. The interlayer distance between the two-dimensional lamellar structures depends on the hydration level [23]. The interfacial water dynamics has a significant role in chemical and biological systems compared to bulk water [24]. In general, the water molecules can form four hydrogen bonds with its nearest neighbors in a bulk water environment. However, the interfacial water molecule has restricted orientational degrees of freedom. Baker et al. had reported pump-probe results on dynamics of confined water molecules in acetone environment. It had been claimed that the hydrogen-bond and orientational dynamics were much slower in an acetone environment compared to bulk liquid water [25]. In another study of a water nanodroplet, Baker had shown the –OH stretch vibration lifetime of 0.85 ± 0.1 ps, which is three times slower than in bulk liquid water [26].

To study ultrafast dynamics of matter, time-resolved third-order nonlinear infrared spectroscopy is widely used in the research community. Two-color pump-probe and four-wave mixing spectroscopy are the examples of third-order nonlinear techniques. Both are fundamentally the same techniques with different geometries (figure 1.1) to measure ultrafast molecular dynamics, carrier dynamics and many other ultrafast phenomena on femtosecond time scale. Using pump-probe experiments, population dynamics of excited states and coherent wavepacket dynamics of anharmonically coupled low-frequency modes can be studied. In photon echo experiments coherence loss and spectral diffusion due to vibrational transitions are generally studied [27, 28]. The relation between the lifetime and coherence times is given below in equation 1.1.

$$\frac{1}{T_2} = \frac{1}{2T_1} + \frac{1}{T_2^*} \tag{1.1}$$

The T_1 is the population relaxation time of the excited state, T_2 is homogeneous dephasing time of transition states and T_2^* is the pure dephasing which is caused by fluctuations of the environment. We used the two-color pump-probe technique to study molecular and carrier dynamics in graphene oxide and the semiconductor saturable absorber mirror (SESAM).

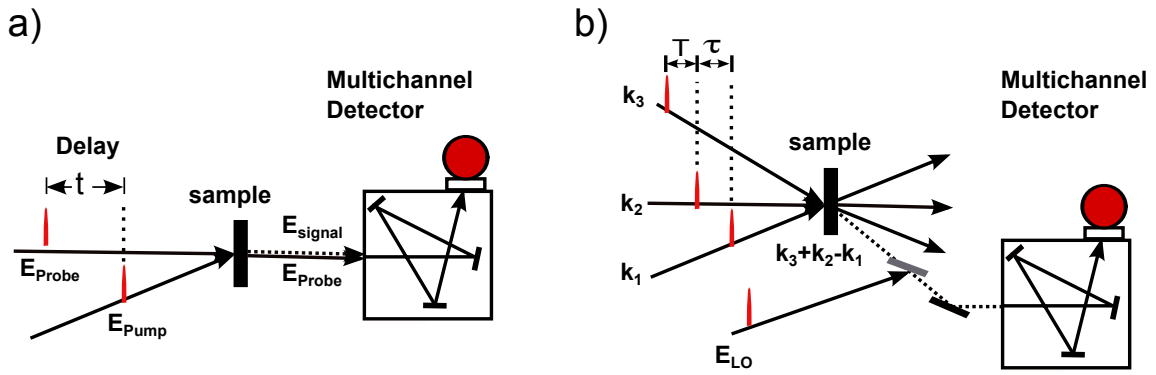

Figure 1.1: Schematic representation of third-order nonlinear infrared spectroscopy techniques to measure ultrafast dynamics in matter. a) Two-color pump-probe set up. 't' is the delay between pump and probe pulses. b) Heterodyne detected three pulse photon-echo set up. 'τ' is the coherence time and 'T' is the population time.

The organization of the thesis is as follows:
In the second chapter, the theoretical background of light propagation in nonlinear media, and the third order nonlinear spectroscopy are presented. In the third chapter, the experimental techniques are discussed. In this chapter, the frequency tripler, mid-infrared light generation using optical parametric amplification (OPA) and the difference frequency generation processes, the design of two color pump-probe set up and laser pulse characterization techniques are presented in detail. In the fourth chapter, we studied ultrafast dynamics in graphite oxide using single-color and two-color pump-probe spectroscopy. The effect of pump frequency and pump fluence on the carrier-phonon scattering in graphite oxide are discussed. Also, the results on intercalated water dynamics in graphite oxide are presented. The fifth chapter demonstrates results on the carrier relaxation dynamics of the SESAM. In this chapter, the pump-probe set-up is rearranged to measure the differential reflective changes in the SESAM. The last chapter summarizes the experimental techniques and ultrafast measurements on graphite oxide and SESAM with future perspectives.

Chapter 2

Theoretical background: Nonlinear Spectroscopy

2.1 Introduction

Optical spectroscopy is a powerful technique to study light-matter interactions. Linear spectroscopy provides static information on the system under studies such as resonance frequencies, spectral amplitudes, and lineshapes. All these phenomena are detected by averaging the system's response over all time scales. However, the advancement in laser technology made it possible to generate high intensity light pulses, which led to the birth of nonlinear spectroscopy. Multiple interactions of laser pulses with matter allow to discern the nonlinear optical response of the system to understand molecular dynamics, coupling mechanisms and transition structures on ultrafast time scales.

This chapter is based on Shaul Mukamel's book on nonlinear optical spectroscopy [29], Robert W. Boyd's book on nonlinear optics [30] and the PhD thesis of Prof. Nils Huse [31].

2.2 Maxwell's equations

The basic equations of classical electrodynamics developed by Carl Friedrich Gauss, André-Marie Ampère, Michael Faraday, Charles-Augustin de Colomb, Hans Christian Ørsted, Jean-Baptiste Biot and Félix Savart had been integrated by James Clerk Maxwell into a set of four partial differential equations known as Maxwell's equations. These

equations, along with Lorentz force law, established the foundation of classical electromagnetism, classical optics, and electronic circuits. The following equations 2.1-2.2 are the inhomogeneous electric and magnetic field[1] equations, which can be used to describe the wave behavior of light in space due to sources and the equations 2.3-2.4 are the homogeneous equations describe field circulation around its sources.

$$\bigtriangledown \cdot \vec{E} = 4\pi\rho \qquad \cdots \text{(Gauss's law of electricity)} \tag{2.1}$$

$$\bigtriangledown \cdot \vec{B} = 0 \qquad \cdots \text{(Gauss's law of magnetism)} \tag{2.2}$$

$$\bigtriangledown \times \vec{E} = -\frac{1}{c}\frac{\partial \vec{B}}{\partial t} \qquad \cdots \text{(Faraday's law of induction)} \tag{2.3}$$

$$\bigtriangledown \times \vec{B} = \mu_0 \left(4\pi\vec{J} + \varepsilon_0 \frac{\partial \vec{E}}{\partial t}\right) \qquad \cdots \text{(Ampere's law)} \tag{2.4}$$

where, $\vec{E}$, $\vec{B}$, ρ, μ_0, ε_0 and $\vec{J}$ denote the electric field, magnetic field, charge density, permittivity, permeability and current density respectively. The detailed description of above Maxwell's equations can be found in any books on classical electrodynamics [32]. The wave equation in nonlinear optical media is derived using above Maxwell's equations[2]:

$$\left(\bigtriangledown^2 - \frac{n^2}{c^2}\frac{\partial^2}{\partial t^2}\right)\vec{E} = \frac{1}{\varepsilon_0 c^2}\frac{\partial^2}{\partial t^2}\vec{P}_{NL} \tag{2.5}$$

where $\bigtriangledown$ is the gradient operator which describes divergence of the field from a source point and c is the speed of light[3] which is equal to $1/\sqrt{\mu_0\varepsilon_0}$ in free space. n is the linear refractive index. The $\vec{P}_{NL}$ is a time-varying polarization, which acts as a source to generate nonlinear optical waves in third-order nonlinear spectroscopy. The electric and magnetic

[1] The electric and magnetic field vectors are denoted by $\vec{E}$ and $\vec{B}$ respectively throughout this thesis.

[2] The vector calculus identity: the curl ($\bigtriangledown \times$) of curl ($\bigtriangledown \times (\bigtriangledown \times \vec{A}) = \bigtriangledown (\bigtriangledown \cdot \vec{A})$ - $\bigtriangledown^2 \vec{A}$) of the equations 2.3 and 2.4 is used to derive wave equation in nonlinear optical media.

[3] speed of light in free space: $c = 1/\sqrt{\mu_0\varepsilon_0} = 299\ 792\ 458$ m/s

field of a plane wave propagates in phase in space and their directions are perpendicular to each other in isotropic media.

The electric field of a plane electromagnetic wave traveling in space is specified by its respective wave-vector $\vec{k}$ as follows:

$$\vec{E}(t) = \vec{E}_0(t)\left(e^{-i\omega t+i\vec{k}r} + e^{+i\omega t-i\vec{k}r}\right) \tag{2.6}$$

where E_0 is the amplitude and ω is the frequency of the propagating wave.

The equation of the magnetic field of an electromagnetic wave is analogous to equation 2.6. In an electromagnetic wave, the magnetic field amplitude component is usually negligible compared to the electric field amplitude as the speed of light in free space is also described as $c = \left|\frac{\vec{E}}{\vec{B}}\right|$.

2.3 Light-matter interaction

Electric fields that interact with matter can induce transient polarizations. Depending upon the electric field strength of light either linear or nonlinear processes are induced in the material. Generally, to induce nonlinear processes, high electric field strengths above 10^8 V/m are required. In linear spectroscopy, weak intensity light sources are used, which do not exceed an electric field strength above 10^5 V/m. The modern technology of laser light sources made it possible to exceed this limit to interrogate nonlinear processes in matter. In the following sections, linear and nonlinear interactions of light with matter are discussed.

2.3.1 Linear interaction

In linear media, weak intensity light pulses induce polarization in the material which is explained using the following equation 2.7:

$$P_i(\omega) = \varepsilon_o \chi_{ij}^{(1)}(\omega) E_j(\omega) \tag{2.7}$$

where, P_i is the induced polarization, ε_o is the vacuum permittivity, $\chi_{ij}^{(1)}$ is the electric

susceptibility tensor of order 1. The indices i and j denote the Cartesian components of the polarization and the incoming incident field respectively. E_j is applied electric field.

Equation 2.7 shows the induced polarization which is linearly proportional to the incident electric field. This interaction can be viewed from the perspective of linear absorption of a vibrationally active molecule where the molecule is excited from ground state to the excited state associated with a change in the dipole moment of a molecule.

2.3.2 Non-linear interaction

In nonlinear media, the high-intensity laser field interacts with matter that induces the dielectric polarization $\vec{P}$ which is nonlinearly proportional to the electric field $\vec{E}$. Such induced polarization acts as a source of propagation of electromagnetic fields. The measurement of these electromagnetic fields is the determination of the induced polarization which is directly linked to quantum mechanical properties of the object. The equation 2.7 is then expanded using Taylor's series of the dielectric polarization density $\vec{P}(\omega)$ in powers of the electric field $\vec{E}(\omega)$ as follows:

$$\begin{aligned} P_i(\omega) =& \varepsilon_o \chi^{(1)}_{ij}(\omega) E_j(\omega) + \varepsilon_o \chi^{(2)}_{ijk}(\omega, \omega_1, \omega_2) E_j(\omega_1) E_k(\omega_2) \\ &+ \varepsilon_o \chi^{(3)}_{ijkl}(\omega, \omega_1, \omega_2, \omega_3) E_j(\omega_1) E_k(\omega_2) E_l(\omega_3) + ... \\ =& P^{(1)}_i(\omega_1) + P^{(2)}_i(\omega_2) + P^{(3)}_i(\omega_3) + \cdots \end{aligned} \tag{2.8}$$

where P_i and E_i are the polarization and electric field components, respectively.

$\chi^{(n)}$ is the electric susceptibility tensor of order n.

ε_o is the vacuum permittivity.

Nowadays, the nonlinearity can be easily induced due to the development of pulsed laser sources. The laser pulses can be easily focused down to generate intensity of the electric field on the order of 10^9 V/m which is comparable to the electrical fields exist between electrons and nuclei in atoms which constitute the matter.

In general, the n^{th} order nonlinearity leads to (n+1) wave mixing. Let's, look at the second-order nonlinear phenomena induced by electromagnetic field oscillating at two frequencies ω_1 and ω_2. The second order polarization $\vec{P}^{(2)}$ in equation 2.8 has the following form:

$$\vec{P}_i^{(2)}(\omega_3) = \varepsilon_o \chi_{ijk}^{(2)} \vec{E}_j(\omega_1) \cdot \vec{E}_k(\omega_2) \tag{2.9}$$

The induced second-order polarization oscillates not at ω_1 and ω_2, but at new frequencies $\omega_3 = 2\omega_1, 2\omega_2, \omega_1+\omega_2, |\omega_1 - \omega_2|$ which correspond to the second harmonic generation (SHG), sum frequency generation (SFG), difference frequency mixing (DFM), and optical rectification(OR, $\omega_3 = 0$).

The intensity I_i, of the emitted field $E(\omega_3)$ by the induced polarization $P_i^{(2)}(\omega_3)$ at a frequency ω_3 has the following form [30]:

$$I_i(\omega_3) \propto |\chi_{ijk}^{(2)}|^2 I_j I_k L^2 \mathrm{sinc}^2 \left(\frac{\left|\Delta\vec{k}\right| L}{2} \right) \tag{2.10}$$

where, $\mathrm{sinc}(x) = \sin(x)/x$, L is the optical path length and Δk is the difference between propagation wavevector of the incident and generated optical fields.
The difference in wavevector Δk is known as phase mismatch:

$$\Delta\vec{k} = \vec{k}_{out} - \sum \vec{k}_{in} \tag{2.11}$$

where, $\vec{k}_{out}$ is the wavevector of the generated new wave
and $\sum \vec{k}_{in}$ is the summation of wavevectors of the incident optical fields.

The wave-vector has the expression : $\left|\vec{k}\right| = k = \frac{n(\omega)\cdot\omega}{c}$. $n(\omega)$ is the refractive index of the material which depends upon the frequency and polarization of the incident field. At each point in nonlinear media where fields $E_j(\omega_1)$ and $E_k(\omega_2)$ overlap, strong second-order response is generated, if the $\Delta\vec{k} = \vec{k}_{out} - \sum \vec{k}_{in} = 0$. Since, the photon momentum $\vec{p}$ ($\vec{p} = \hbar\vec{k}$) is related to the wave-vector $\vec{k}$, this implies the conservation of the momentum of interacting fields.

The detailed examples of second-order nonlinear effects with momentum conservation is presented in section 3.3 of the experimental chapter of this thesis, where the optical parametric amplifier and frequency tripler are discussed.

In isotropic media, nonlinear effects scale only with odd orders of the electric field due to the existence of inversion symmetry, it vanishes even order terms in Taylor expansion series in equation 2.8. Generally, inversion symmetry exists in liquid solutions. Hence, the third order term in the equation 2.8 is the lowest nonlinear response and the expression of the third order nonlinear polarization is given by:

$$P_i^{(3)}(\omega_4) = \chi_{ijk}^{(3)} E_j(\omega_3) \cdot E_k(\omega_2) \cdot E_l(\omega_l) \tag{2.12}$$

As we know, the induced third-order polarization acts as a source of an electromagnetic field. The intensity of the emitted third order field of frequency ω_4 depends upon the frequencies of the incident fields and geometry of the experiment [30]. The enhancement of the third order field is largest when $\Delta\vec{k} = 0$. The expression for the intensity of the third order field is as follows:

$$I_i(\omega_4) \propto |\chi_{ijk}^{(3)}|^2 I_j I_k I_l L^2 \mathrm{sinc}^2 \left(\frac{\left|\Delta\vec{k}\right| L}{2} \right) \tag{2.13}$$

This thesis is aimed to build a pump-probe spectrometer for the mid-infrared spectral region. Pump-probe spectroscopy is a third order process which involves the interaction of three electric fields in material, which then results in the generation of a third order signal. However, in the pump-probe spectroscopy two beams interact in the material, the strong pump is a high-intensity beam which is considered to generate two interactions in the sample.

2.3.3 The quantum mechanical polarization and density matrix

The systems response to the external field is measured by detecting emission field. The excitation laser field (E(t)) is coupled with the system according to the interaction term $\mu \cdot E(t)$. The macroscopic polarization of the system is defined as the expectation value of the dipole moment operator μ. However, the systems state is conveniently described by

the density operator $\rho_{(t)}$. The time-dependent macroscopic polarization is then given by

$$P_i(t) = \langle \mu_i \rho(t) \rangle \tag{2.14}$$

where $\langle\ \rangle$ is the trace of the corresponding matrix representation.
The density matrix of pure states is defined as follows:

$$\rho = \sum_k P_k \cdot |\Psi_k\rangle\langle\Psi_k| \tag{2.15}$$

where $P_k \geq 0$ and $\sum_k P_k = 1$ (normalization). P_k is the probability of the system in a pure state $|\Psi_k\rangle$.

However, in condensed matter systems we deal with the statistical ensemble rather than pure states. If we consider the state $|\Psi_k\rangle$ has a basis set $\{|n\rangle\}$ then the state $|\Psi_k\rangle$ can be written as $|\Psi_k\rangle = \sum_n c_n(t)|n\rangle$ and its complex conjugate is written as $\langle\Psi_k| = \sum_m c_m^*(t)\langle m|$ then the density matrix has the elements:

$$\rho_{nm} = \sum_k P_k \langle n|\Psi_k\rangle\langle\Psi_k|m\rangle \tag{2.16}$$

Equation 2.16 depicts, when n=m then the diagonal elements of the density matrix ρ_{nn} represents probability of the system to be found in the state $|m\rangle$ or $|n\rangle$ also known as population.

$$\rho_{nm} = \sum_k P_k \langle n|\Psi_k\rangle\langle\Psi_k|m\rangle = \sum_k P_k |\langle n|\Psi_k\rangle|^2 \geq 0 \tag{2.17}$$

The off-diagonal elements, ρ_{nm} with $n \neq m$ represents the coherence of the system. Generally, these elements are complex numbers and constitute information about the phase.
The temporal evolution of density matrix of quantum system is described by the Liouville von Neumann equation :

$$i\hbar\frac{\partial}{\partial t}\rho(t) = [H(t), \rho(t)] \tag{2.18}$$

where [ ] is a commutator operator. The equation 2.18 is derived using the Schrödinger equation, $\frac{\partial}{\partial t}|\Psi_k(t)\rangle = -\frac{i}{\hbar}H(t)|\Psi_k(t)\rangle$, and density matrix formulation.

Then, the total Hamiltonian H(t) has the following form, which comprises components of the unperturbed, H_0 and the perturbed, $\mu_i \cdot E(t)$ contributions of the system.

$$H(t) = H_0 + \mu \cdot E(t) \tag{2.19}$$

The perturbation term arises when the (time-dependent) electric field of laser pulse interacts with the system, is also known as interaction energy.

2.3.4 The nonlinear optical response functions

To interpret the nonlinear optical response of the quantum systems, interaction picture is used which visualizes the dynamics of the system induced by laser pulses and in between the laser pulses hence intrinsic to the system itself. The interaction energy $\mu_i \cdot E$ is smaller compared to the transient energies of the isolated molecules. The perturbation theory is useful here to expand density operator which is linked to the higher order polarization terms of equation 2.8. To converge the cumulant expansion, the transformation of the Schödinger picture to the interaction picture is to be made by the use of the Unitarian time evolution operator. In interaction picture the dipole operator has the following form:

$$\mu_i(t) = U_0(t, t_0)^\dagger \cdot \mu_i \cdot U_0(t, t_0) \tag{2.20}$$

where $U_0(t, t_0)$ is an unitary time dependent operator. In stationary state the Hamiltonian is H_0 which is time independent and when light pulse interacts with the system it becomes time dependent. The system evolution is expressed by time evolution operator with respect to the stationary state Hamiltonian H_0 as follows:

$$U_0(t, t_0) = \exp\left[-\left(\frac{i}{\hbar}\right) H_0(t - t_0)\right] \tag{2.21}$$

then the density matrix becomes:

$$\rho_I(t) = U_0(t, t_0)^\dagger \rho(t) U_0(t, t_0) \tag{2.22}$$

The Liouville-Von Neumann equation 2.18 can be integrated and substituted iteratively into itself and expanded in the powers of the electric field. In the interaction

picture, the cumulative expansion of the n^{th} order density matrix is as follows:

$$\rho_I(t) = \rho^{(0)}(t_0) + \sum_n \rho^{(n)}(t) \tag{2.23}$$

$$\begin{aligned}\rho^n(t) = \left(-\frac{i}{\hbar}\right) \int_{t_0}^{t} d\tau_n \int_{t_0}^{\tau_n} d\tau_{n-1} \cdots \\ \int_{t_0}^{\tau_2} d\tau_1 E(\tau_n) \cdot E(\tau_{n-1}) \cdots E(\tau_1) U_0(t, t_0) \cdot \\ \Big[\mu_i(\tau_n), \Big[\mu_i(\tau_{n-1}), \cdots \Big[\mu_i(\tau_1), \rho_{t_0}\Big] \cdots \Big]\Big] \cdot U_0^{\dagger}(t, t_0)\end{aligned} \tag{2.24}$$

The first term $\rho^{(0)}(t_0)$ in equation 2.23 is the density matrix at equilibrium which doesn't evolve over time when subjected to system Hamiltonian H_0, and hence $t_i \longrightarrow -\infty$. We put equation 2.24 in equation 2.14 and obtain the n-th order polarization:

$$\begin{aligned}P_i^{(n)}(t) = \left(-\frac{i}{\hbar}\right) \int_{-\infty}^{t} d\tau_n \int_{-\infty}^{\tau_n} d\tau_{n-1} \cdots \\ \int_{-\infty}^{\tau_2} d\tau_1 E_{i1}(\tau_1) \cdots E_{in}(\tau_n) \\ \times \langle \mu_i(t) \left[\mu_{in}(\tau_n), \cdots [\mu_{i1}(\tau_1), \rho(-\infty)] \cdots\right] \rangle\end{aligned} \tag{2.25}$$

Very often a coordinate transformation is applied as follows:

$$\begin{aligned}\tau_0 &= 0 \\ t_1 &= \tau_2 - \tau_1 \\ t_2 &= \tau_3 - \tau_2 \\ &\cdot \\ &\cdot \\ &\cdot \\ t_n &= t - \tau_n\end{aligned}$$

The τ's represent absolute time points, while t's denote time intervals as explained in below figure 2.1

Using set of above time variables, the nonlinear polarization equation 2.25 can be written as a convolution of n electric fields:

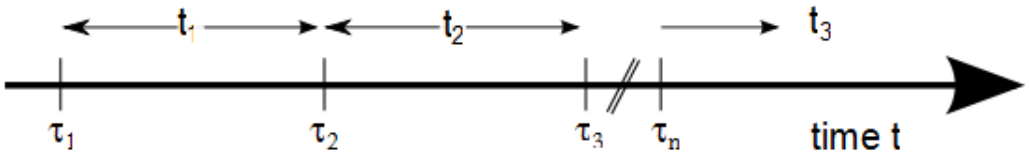

Figure 2.1: Time variables: the τ's refer to absolute times, and t's to time intervals.

$$P_i^{(n)}(t) = \int_{-\infty}^{\infty} dt_n \int_{-\infty}^{\infty} dt_{n-1} \cdots \int_{-\infty}^{\infty} dt_1 S^n(t_n, t_{n-1}, ..., t_1) \cdot \\ \cdot E(t - t_n) \cdot E(t - t_n - t_{n-1}) \cdots E(t - t_n - t_{n-1} - \cdots - t_1) \tag{2.26}$$

with the n-th order response function:

$$S_i^n(t_n, t_{n-1}, ..., t_1) \equiv \left(-\frac{i}{\hbar}\right)^n \Theta(t_1)\Theta(t_2) \cdots \Theta(t_n) \cdot \\ \cdot \langle \mu_i(t_n + \cdots + t_1) \left[\mu_i(t_{n-1} + \cdots + t_1), \cdots [\mu_i(0), \rho(-\infty)]\right]\rangle \tag{2.27}$$

$S^{(n)}$ is the n-th order nonlinear optical response function in the time domain. It comprises microscopic information about the induced polarization by incident electric fields in matter. It obeys the causality principle, so the response function is 0 when $t_0 < 0$

$$S_i^n(t_n, t_{n-1}, ..., t_1) = 0 \tag{2.28}$$

corroborated by Heaviside function's $\Theta(t_i)$ existing in equation 2.27.

Feynman diagrams

The nonlinear response function in the above equation 2.27 can provide all information about the origin of nonlinear signals from the molecular system, but the entire function itself is almost impossible to measure. Terms in above equation 2.27 are difficult to understand when numerous electric fields interact with a molecular system having multiple quantum states, it requires the huge number of permutations when performing experiments on such systems. The response function is a tensor which is a sum of 2^{n-1} real tensors of rank n+1. There are n interactions of the incident electric fields with the matter which lead to emit the radiative signal. The radiative signal and the incident n

electric fields generate n+1 light matter interactions so this n order spectroscopy is also known as n+1 wave mixing. For two-level systems, the interaction of three fields with the dipole operator provides four possible tensors as explained below with Feynman diagrams (figure 2.2) and corresponding response function can be defined as follows:

$$\begin{aligned} S^{(3)} &= \left(-\frac{i}{\hbar}\right)^3 \Theta(t_1)\Theta(t_2)\Theta(t_3) \\ &\quad \langle \mu(t_3+t_2+t_1)\,[\mu(t_2+t_1),[\mu(t_1),[\mu(0),\rho(-\infty)]]]\rangle \\ &= \left(-\frac{i}{\hbar}\right)^3 \Theta(t_1)\Theta(t_2)\Theta(t_3) \sum_{\alpha=1}^{4} \left\{R_\alpha - R_\alpha^\dagger\right\} \end{aligned} \tag{2.29}$$

where, R_α and $R_\alpha^\dagger$ are the response functions and $R_\alpha^\ddagger$ is the complex conjugate of the R_α. The response functions in the above equation 2.29 can be written as follows:

$$\begin{aligned} R_1 &= \langle \mu(t_3+t_2+t_1)\mu(0)\rho(-\infty)\mu(t_1)\mu(t_2+t_1)\rangle \\ R_1^\dagger &= \langle \mu(t_3+t_2+t_1)\mu(t_2+t_1)\mu(t_1)\rho(-\infty)\mu(0)\rangle \\ R_2 &= \langle \mu(t_3+t_2+t_1)\mu(t_1)\rho(-\infty)\mu(0)\mu(t_2+t_1)\rangle \\ R_2^\dagger &= \langle \mu(t_3+t_2+t_1)\mu(t_2+t_1)\mu(0)\rho(-\infty)\mu(t_1)\rangle \\ R_3 &= \langle \mu(t_3+t_2+t_1)\mu(t_2+t_1)\rho(-\infty)\mu(0)\mu(t_1)\rangle \\ R_3^\dagger &= \langle \mu(t_3+t_2+t_1)\mu(t_1)\mu(0)\rho(-\infty)\mu(t_2+t_1)\rangle \\ R_4 &= \langle \mu(t_3+t_2+t_1)\mu(t_2+t_1)\mu(t_1)\mu(0)\rho(-\infty)\rangle \\ R_4^\dagger &= \langle \mu(t_3+t_2+t_1)\rho(-\infty)\mu(0)\mu(t_1)\mu(t_2+t_1)\rangle \end{aligned} \tag{2.30}$$

In these Feynman diagrams, the density operator is represented by two vertical lines: it symbolizes the temporal evolution of the bra and ket of the ensemble states and the time runs from the bottom to the top. The left line represents the temporal evolution of the ket and similarly, the right line represents the temporal evolution of the bra. The field interactions are represented with arrows: those pointing inward represent photon absorption and those pointing outwards represent photon emission. An arrow pointing to the left represents a complex electric field interaction with phase factor $e^{-i(\omega t+k_i r_i)}$, and arrows pointing to the left of phase diagram represents the complex conjugate. Between the pair of vertical lines, the representation of the temporal evolution of ensemble states

are represented in terms of the density matrix in the corresponding time interval. For two level system, there exist four density matrix elements as $\rho = \begin{pmatrix} \rho_{00} & \rho_{01} \\ \rho_{10} & \rho_{11} \end{pmatrix}$. The subscripts 0 and 1 denote the ground and excited states respectively. The diagonal elements represent population states and off-diagonal elements represent coherent states. The overall sign of each diagram depends on the number of field interactions on the right side n, which is given as: $(-1)^n$. The last interaction is represented by a dashed arrow always pointing outwards, which representing the dipole operator in equation 2.14. It represents the emission of a field whose k-vector and frequency depends on the preceding field interactions. The last interaction always represents the return of the system in ρ_{00} population state which contributes to the signal. Above rules for the construction of double-sided Feynman diagrams are convenient to establish the relevant terms of the optical response function.

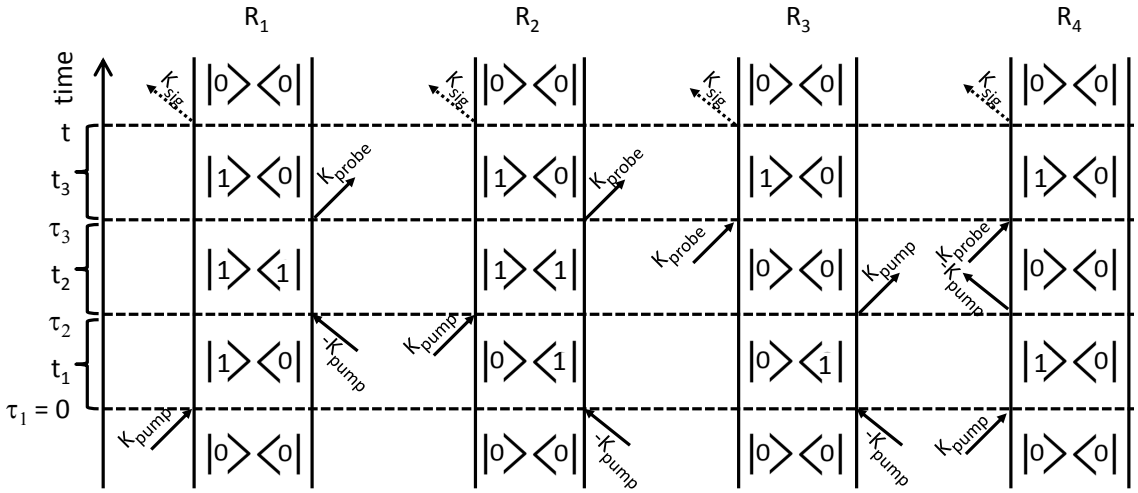

Figure 2.2: The representation of third-order nonlinear response of a two-level system with double-sided Feynman diagrams.

2.4 Pump-probe spectroscopy

In pump-probe spectroscopy, the strong pump pulse E_{pu} induces an optical transition in the sample. The temporal evolution of the sample is monitored by a weak pulse E_{pr} called probe. The pump pulse E_{pu} precedes the probe pulse E_{pr}. These two pulses non-collinearly pass through the sample with some angle which allows only certain Liouville space path-ways that contribute to the third order nonlinear signal. The pump pulse passes over a delay stage to create a temporal delay relative to the probe pulse. The induced transient third order polarization, $P^{(3)}$ generates an electromagnetic field E_{signal}, which propagates in the same direction as that of the transmitted probe pulse, as shown in the following figure 2.3. The emitted signal E_{signal} and probe pulse E_{pr} are passed over into the spectrometer, where these pulses are spectrally dispersed using grating optics and their interference measured on a spectral array of a multichannel detector.

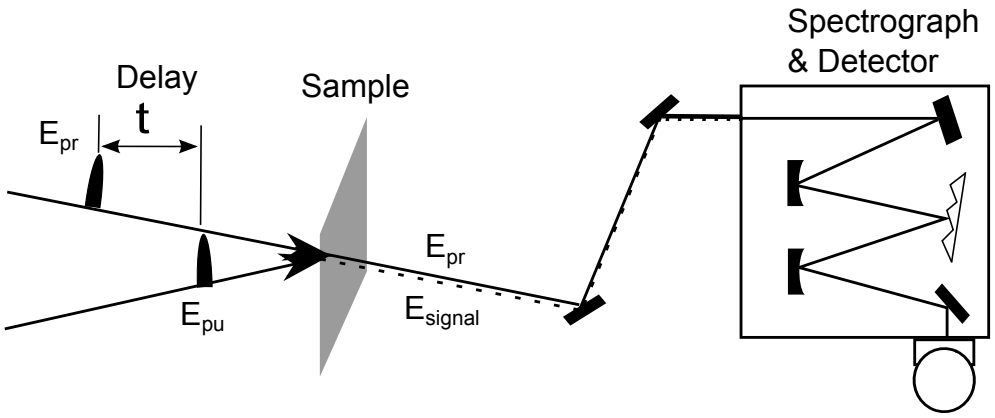

Figure 2.3: Schematic representation of non-collinear pump-probe set up with a frequency resolving spectrometer.

By varying the delay between the pump and probe pulses, the transient transmission changes in the sample are measured by monitoring probe pulse intensity on the multichannel detector as a function of temporal delay 't' and frequency 'ω'. For an emitted signal which is weaker compared to the probe pulse, the corresponding transmission change is

given by:

$$\begin{aligned}\Delta T\left(t,\omega\right) =& \frac{I\left(t,\omega\right) - I_0\left(\omega\right)}{I_0\left(\omega\right)} = \frac{\int_G dt \left|E_{probe}(\omega) + E_{signal}\left(t,\omega\right)\right|^2}{\int_G dt \left|E_{probe}(\omega)\right|^2} - 1 \\ \approx& \frac{2\int_G dt \Re\left\{E_{probe}(\omega)E^*_{signal}\left(t,\omega\right)\right\}}{\int_G dt \left|E_{probe}(\omega)\right|^2}\end{aligned} \tag{2.31}$$

where I and I_0 are the intensities of transmitted probe pulses with and without sample excitation by a pump pulse respectively. R is the real part of the complex expression and G is the time gate of the electronic integrators. While performing pump-probe experiments, the absorbance change ΔA is measured which is retrieved by applying the logarithmic function to the equation 2.31. The decreased transmission change renders a positive absorbance change and similarly, increased absorption renders negative absorption change.

For a three-level system, where the pump pulse precedes the probe pulse and since the geometry of pump-probe field interactions is non-collinear, the possible Liouville pathways are understood with the help of Feynman diagrams (figure 2.4).

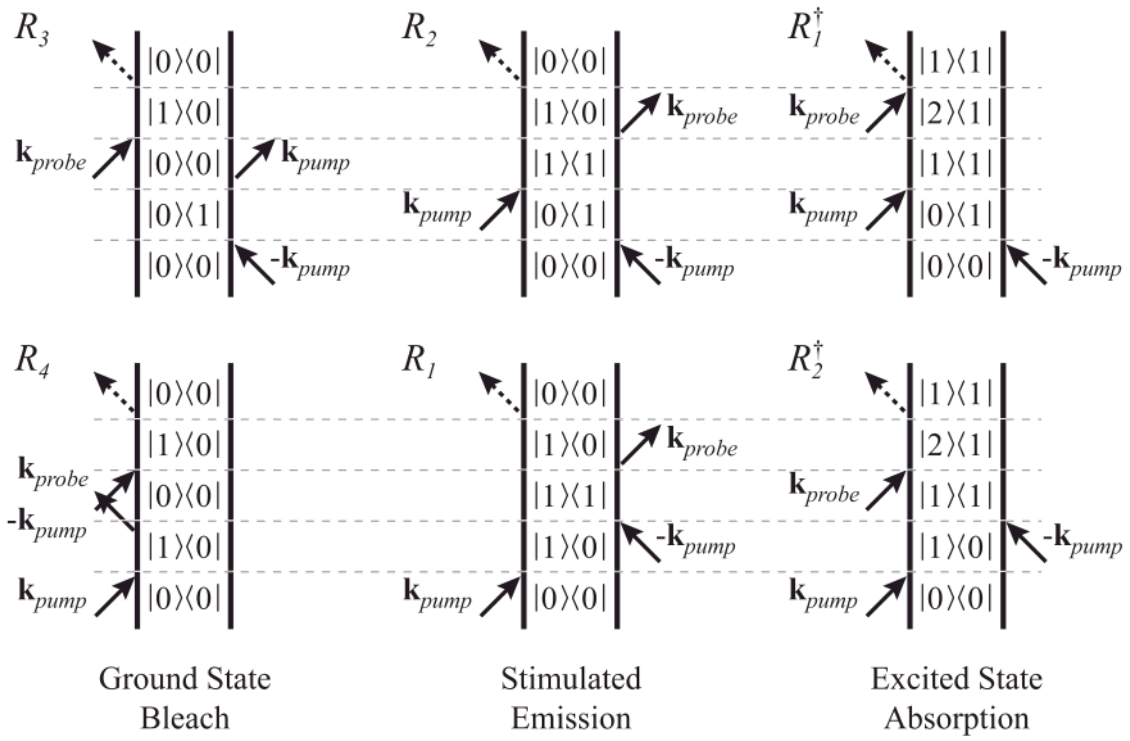

Figure 2.4: Representation of third-order nonlinear response of a three-level system with double-sided Feynman diagrams.

In the semi-impulsive limit, that is when incident optical fields are much shorter compared to the time scale of the system and but longer than the oscillation period of the incident field. In this case, the laser pulses which can be approximated as δ functions, still carries information a carrier frequency and a wavevector. In this limit, the 3^{rd} order response function can be simply obtained as: $\mathrm{P}^{(3)}(\mathrm{t}) = \mathrm{S}^{(3)}(\mathrm{t}_1, \mathrm{t}_2, \mathrm{t}_3)$. For the spectrally broad and temporally short pump pulse (shorter than the response of the system) which excites the system from the ground state ($\nu = 0$) to the first excited state ($\nu = 1$) to form a coherent superposition state. The temporally separated probe pulse then monitors the ground state bleach, stimulated absorption and excited state absorption.

The total response function induced by δ-like pump pulses according to ref. [33] is given as follows:

$$S^{(3)}(t_3, t_2, t_1) = \sum_{i=1}^{6} S_i^{(3)}(t_1, t_2, t_3) \propto \frac{i}{\hbar^3} \left(4\mu_{10}^4 e^{-i(\omega_{10}/\hbar)t_3} - 2\mu_{10}^2\mu_{21}^2 e^{-i(\omega_{21}/\hbar)t_3}\right) e^{-\Gamma t_3} \tag{2.32}$$

where μ_{10} and μ_{21} are the transition dipole moments,

ω_{10} and ω_{21} are the transition frequencies,

Γ is the dephasing rate. Here it is assumed same for 01 and 12 transitions.

t_1, t_2 and t_3 are the relative delays between the laser field interactions.

In pump-probe experiments, the pump interacts twice with wavevectors $\vec{k}_{pump}$ and $-\vec{k}_{pump}$, hence, they cancel each other due to its opposite signs and momentum conservation fulfilled as $\vec{k}_{signal} = \vec{k}_{probe}$.

The emitted signal measured as an absorbance change on the spectrally resolved multichannel slow detection devices as function of time 't' by heterodyning with the probe pulse, is written as:

$$\Delta A(\omega) = -\log_{10}\left(\frac{\left|E_{pr}(t) + iP^{(3)}(t)\right|^2}{\left|E_{pr}(t)\right|^2}\right) \approx \frac{2\Re\left(E_{pr}(t) \cdot P^{(3)}(t)\right)}{\left|E_{pr}(t)\right|^2} \tag{2.33}$$

The spectrometer performs a Fourier transform of the electric fields with respect to time 't' to obtain the pump-probe spectrum:

$$\Delta A(\omega) \propto -2\Re\left(P^{(3)}(\omega)\right) = -\frac{8\mu_{10}^4\Gamma}{(\omega_{10}-\omega)^2+\Gamma^2} + \frac{4\mu_{10}^2\mu_{21}^2\Gamma}{(\omega_{21}-\omega)^2+\Gamma^2} \tag{2.34}$$

Here, the probe pulse was assumed to be a δ-pulse with a constant frequency spectrum. The negative term in the above equation represents the ground state bleaching (GSB) and stimulated emission (SE) and the positive term the excited state absorption (ESA). The ground state bleach and stimulated emission is spectrally indistinguishable. The stimulated emission is red-shifted due to anharmonicity. For a harmonic oscillator, the signal ΔA vanishes due to the equidistant spacings of the transition states.

However, when the probe pulse precedes the pump pulse, that is at negative time delays in a frequency resolved pump-probe measurement, the signal that is generated when pump

and probe pulse start overlapping is ascertained to the perturbed free induction decay process [34]. It is explained using Feynman diagrams in the following figure 2.5:

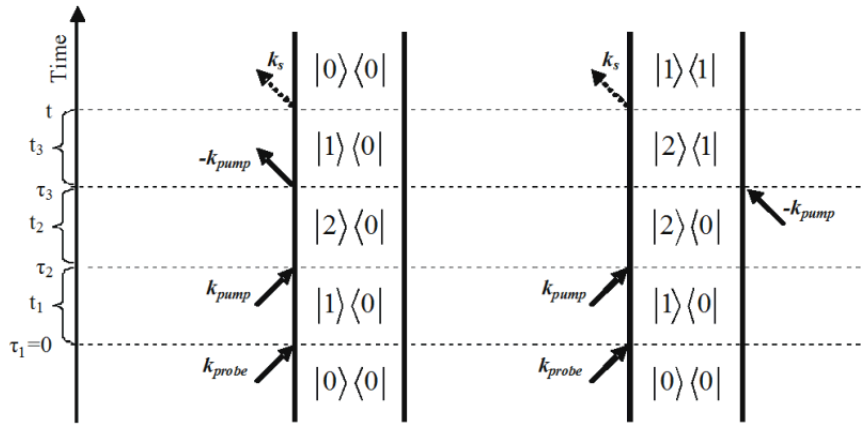

Figure 2.5: Illustration of perturbed free induction decay process by using Feynman diagrams.

The perturbed free induction decay originates from the quantum pathways when the probe interacts in between the pump interactions $\vec{k}_{\text{pump}} \rightarrow \vec{k}_{\text{probe}} \rightarrow \vec{k}_{\text{pump}}$. These contributions to the signal arises when pump and probe pulses starts overlapping are termed as 'coherent artifact'. Another contribution to the signal arises from optical Kerr effect induced refractive changes which shifts the probe spectrum [30].

The optical Kerr effect induced refractive index change phenomenon is known as cross-phase modulation, which is analogous to self-phase modulation, in which modulation of light fields occur in a media with large nonlinear coefficients.

Chapter 3

Experimental Techniques

When God said "Let there be light" he surely must have meant perfectly coherent light

- Charles Townes

3.1 Introduction

In this thesis, pump-probe results on carrier dynamics in a semiconductor saturable absorber (SESAM) and a combined effect of the carrier and vibrational dynamics of graphene oxide on femto to picoseconds timescales will be discussed. Generally, carrier and vibrational dynamics investigations are carried out in the spectral range between 1000-5000 cm^{-1} for which intense, short light pulses generated from lasers are used.

The laser is an acronym for the 'Light Amplification by Stimulated Emission of Radiation'. It produces coherent, monochromatic, and collimated light pulses. Einstein introduced the concept of the light amplification by stimulated emission of radiation in 1917 [35]. Almost forty years later Charles H. Townes and his colleagues at Columbia University in 1953 [36] constructed a device to amplify microwaves by stimulated radiation which were termed as MASER (Microwave Amplification by Stimulated Emission of Radiation). The *Maser* was the foundation step to build the first *laser*. In the year 1960, the first optical *Laser* was developed by Theodre Maiman [17] using a synthetic

ruby crystal as an active medium. Shortly afterwards the first nanosecond laser was developed [37]. Subsequently the laser pulse duration was pushed via picoseconds [38, 39] to femtoseconds [40, 41]. Attosecond time resolution was achieved at the turn of the millennium [19, 42]. The femtosecond lasers are based on the technique of chirped pulse amplification (CPA) which provides high pulse intensities of several millijoules [43]. Titanium doped sapphire is a favorable material to build femtosecond laser pulses in the near infrared region due to the availability of large gain bandwidth from 600-1000 nm [44, 45]. Along with the lasers, widely tunable and very stable optical parametric amplifiers have been developed to generate light pulses from the ultraviolate (UV) to the mid-infrared (mid-IR) region [46–48]. Hitherto, there have been many techniques available to generate mid-Infrared light pulses such as plasma based, free electron laser (FEL) based, optical parametric amplification (OPA) based and cascade laser techniques are only few examples of it [49].

In the following sections, the working principle and details of optical parametric amplifier, difference frequency mixing, third harmonic generator (THG), pump-probe setup and pulse characterization techniques will be discussed.

3.2 The laser system

The scheme of the laser system is shown in the figure 3.1. It consists of a commercially available Ti:sapphire laser, the two home-built optical parametric amplifiers with subsequent DFG stages, the second & the third harmonic generator and the pump-probe setup. The Ti:sapphire based laser system incorporates three elementary units: Mai Tai SP oscillator, Empower 45 pump laser and Spitfire Ace regenerative amplifier. The intracavity doubled $Nd^{3+} : YVO_4$ output at 532 nm pumps the Ti:sapphire crystal of the Mai Tai SP oscillator which emits pulses centered at 800 nm with 100 nm bandwidth, 25 fs pulse duration at 84 MHz repetition rate. The oscillator is passively mode-locked by Kerr lensing [50, 51]. The oscillator output is used for further amplification in a regenerative amplifier. Before entering the Pockel cell-switched cavity the seed pulses were stretched temporally by a factor of 10^4 in order to avoid damage of optical components by the

pulse peak intensities. The population inversion in the second Ti: Sapphire crystal in the

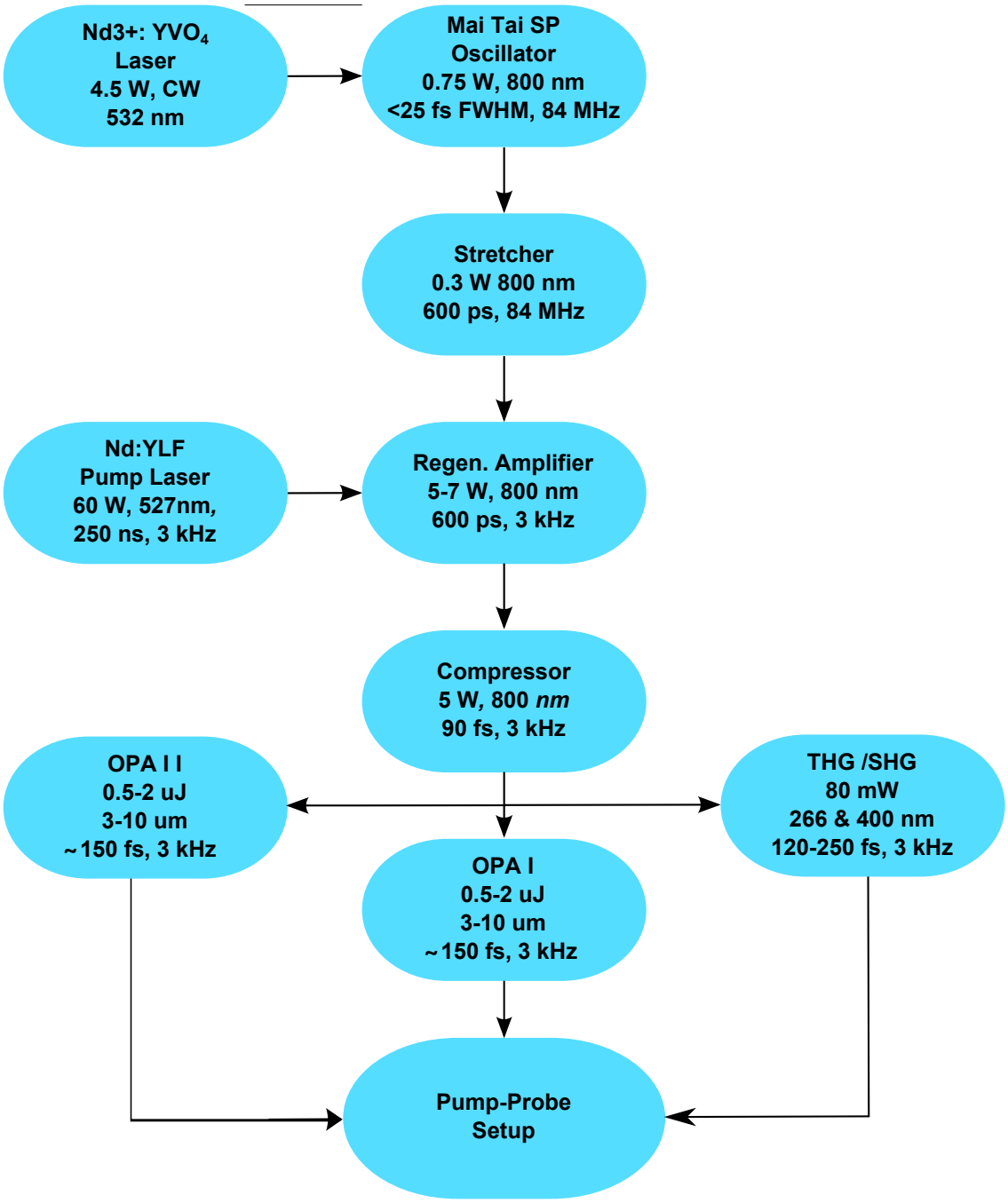

Figure 3.1: Schematic representation of the laser system which comprises the commercial Ti-Sapphire laser system, two optical parametric amplifiers (OPA), the second/third harmonic generator (SHG/THG) and the two-color pump-probe setup.

regenerative amplifier cavity is achieved by an intracavity doubled Q-switched Nd^{3+}:YLF

pump laser (Empower 45) that operates at 3 kHz repetition rate with 200 ns duration of pulses. After about 10 passes through the regenerative amplifier cavity, the amplified pulses are coupled out by the second Pockel cell and compressed to 100 fs having 1.66 mJ pulse energy. To pump the frequency conversion devices the fundamental near-infrared beam was split into three arms with different pulse energies - for details see figure 3.1.

3.3 Optical frequency conversion and amplification

Optical frequency conversion of 800 nm light pulses into UV-vis pulses (266 nm & 400 nm) and widely tunable mid-infrared pulses (3-10 μm) is achieved by using up-conversion and down-conversion of laser light pulses in birefringent crystals, which are having large second order nonlinear susceptibilities $\chi^{(2)}$ [52]. Typical examples of these crystals are KDP, KTP, BBO, $AgGaS_2$, GaSe etc[1]. In optical up-conversion processes, an energetic photon is formed by combining two photons and has therefore an energy which is the sum of the energies of the combining photons [53]. Second harmonic generation (SHG) and sum frequency generation (SFG) are up-conversion processes. In down-conversion processes, a photon is split into two photons having lower energy than the photon entering into nonlinear crystal. Both, difference frequency generation (DFG) as well as optical parametric amplification are down-conversion processes. In DFG, pump and seed waves have comparable energies whereas in OPA the seed wave is much weaker. In figure 3.2 up- and down-conversion processes are illustrated.

In optical parametric amplification, a strong pump wave (k_1,ω_1) and a weak seed wave (k_2,ω_2) generate a third wave (k_3,ω_3) at their difference frequency thereby amplifying the seed wave ω_2 (conventionally $\omega_1 > \omega_2 > \omega_3$) [48]. The light wave at frequency ω_1 is called the fundamental whereas ω_2 and ω_3 are termed signal and idler, respectively.

[1]KDP - Potassium dihydrogen phosphate, KTP - Potassium titanyl phosphate, BBO - Beta barium borate, $AgGaS_2$ - Silver thiogallate, GaSe - Gallium selenide

Energy and momentum are conserved during frequency conversion which requires the following equations to be fulfilled [52]:

$$\omega_p = \omega_s + \omega_i \tag{3.1}$$

$$k_p = k_s + k_i \tag{3.2}$$

Equation 3.2 represents the phase matching condition. The phase matching condition is achieved by exploiting the birefringence of the nonlinear crystal.

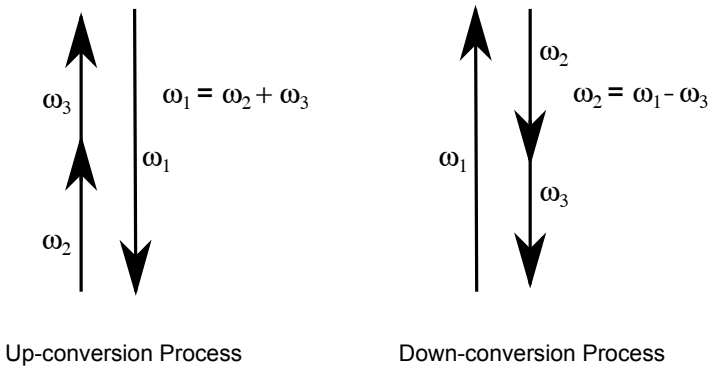

Figure 3.2: Photon frequency conversion processes.

We employed type-I and type-II phase matching crystals for frequency conversion. Birefringent crystals show a refractive index that depends on the direction of propagation and the direction of polarization with respect to the principle plane of the crystal. In order to generate the desired wavelength, the crystal needs to be rotated normal to the principal plane to match the refractive index for the extraordinary waves to constructively interfere with the ordinary waves over the crystal length according to:

$$\frac{n_p}{\lambda_p} = \frac{n_s}{\lambda_s} + \frac{n_i}{\lambda_i} \tag{3.3}$$

Two nonlinear crystals are employed for frequency conversion. Those were BBO and $AgGaS_2$. The BBO crystals with different specifications were used for the generation of

UV pulses as well as generation of signal and idler pulses. The $AgGaS_2$ was used for the generation of mid-IR pulses.

3.4 Generation of UV pulses

UV pulses were generated by collinear frequency tripling of the fundamental near-infrared (800 nm) laser pulses from the regenerative amplifier. A two-stage process was needed to efficiently generate the UV pulses: second harmonic generation (SHG) in the first stage is followed by a third harmonic generation (THG) in the second stage. These high harmonics were generated using the beta-BBO crystals of type I with different specifications[2,3]. The sum frequency process between second harmonic and residual fundamental is shown in the figure 3.3. The generated p-polarized second harmonic pulses were orthogonally polarized to the fundamental laser pulses. This characteristic is exploited for adjusting the timing between the two pulses for THG. To fulfill the phase-matching condition for THG, the polarization of the fundamental is rotated by 90^o using a dual half-wave plate. The residual fundamental precedes the SH due to group velocity mismatch in the SHG

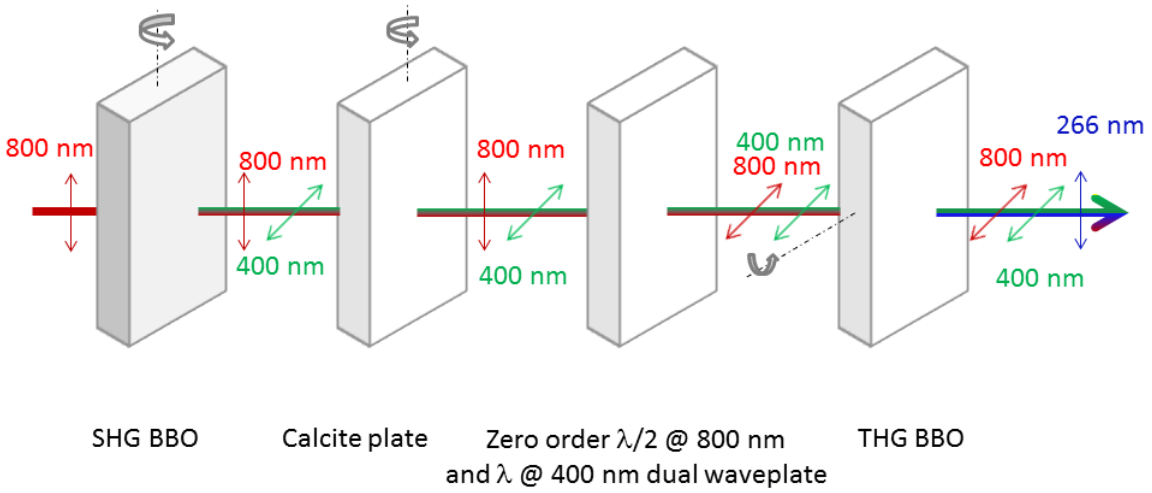

Figure 3.3: Schematic of UV pulse generation

BBO crystal. The time delay between the fundamental and the second harmonic was

[2]BBO crystal, type-I, thickness = 0.5 mm, $\vartheta = 29.2^o$ and $\varphi = 90^o$ for second harmonic generation
[3]BBO crystal, type-I, thickness = 0.2 mm, $\vartheta = 44.2^o$ and $\varphi = 90^o$ for third harmonic generation

corrected by placing a negative uniaxial crystal (also known as group velocity compensation plate) before the wave-plate. Typical examples of negative uniaxial crystals are α-BBO and Calcite [54]. The negative uniaxial crystal has a lower refractive index for the extraordinary wave. Hence, the fundamental wave experiences a lower refractive index than the second harmonic wave. By turning the compensation plate the delay between the fundamental and second harmonic can be adjusted. The frequency tripler delivers 25 μJ s-polarized UV pulses when pumped by 100 μJ, near-IR 800 nm pulses with 100 fs pulse duration. Apart from the high conversion efficiency (15 %), the design of frequency tripler offers the benefit for easy and quick exchange of pump wavelengths (266 nm, 400 nm, and 800 nm).

3.5 Generation of mid-IR pulses

The intense, highly stable and widely tunable mid-infrared laser pulses were generated using a combination of optical parametric amplification and difference frequency mixing. Figure 3.4 depicts the experimental setup of an optical parametric amplifier with difference frequency stage. It is based on the design introduced by Kaindl et al [48]. The fundamental 800 nm laser pulses (90 fs and 250 μJ) from the regenerative amplifier were used as an input to generate signal and idler pulses with 47 μJ combined energy by optical parametric amplification. The fundamental beam was split into three separate beams. First the 1% of the main fundamental beam focused into a 1 mm thick sapphire plate using a plano-convex (f=100 cm) lens to generate seed pulses. The process is also knows as a generation of white light continuum (spectral range 398-1000 nm) encompassing frequencies for seed amplification [55]. Before focusing the beam the wave-plate is added to rotate the polarization by 90°. A filter is added after the sapphire plate which removes the ultraviolet and visible part and transmits only the near-infrared part of the main spectrum which later amplified by refocusing the seed pulses using a plano convex lens (f=4 cm) into a type II second order nonlinear BBO[4] crystal. For amplification of the seed signal pulses, 10% of the fundamental beam was tightly focused into the BBO crystal

[4]BBO (β-BaB_2O_4) crystal, thickness = 4 mm, $\vartheta = 27^o$ and $\varphi = 30^o$)

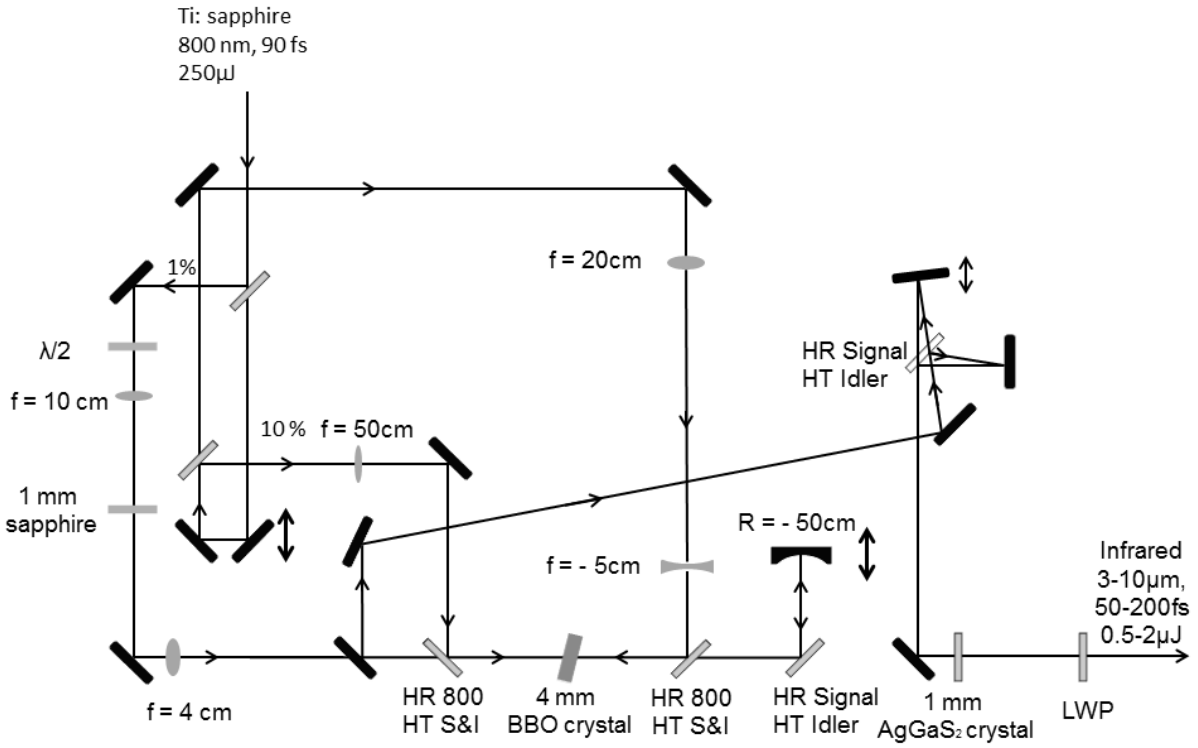

Figure 3.4: The design of experimental setup for the generation of tunable mid-infrared pulses. The BBO crystal is used for amplification and generation of signal and idler pulses. Please note that the fundamental beam pumping the first and second amplification stages are displaced in height. λ/2: half wave plate, HR/HT:high transmission/ high reflection, LWP: long pass filter, S&I: signal & idler

and spatially as well as temporally overlapped with the collinear seed pulses. In order to achieve temporal overlap, the fundamental passes over a manual delay stage. The residual fundamental pulses were filtered using a dichroic mirror (HT Idler & Signal and HR fundamental). The amplified signal and newly generated idler pulses were separated using another dichroic mirror (HT idler and HR signal). Only the signal pulses were used for further amplification. The amplified signal pulses were reflected from the dichroic mirror and collimated by a spherical gold mirror (f = -50 cm) thereby sending the signal back into the BBO crystal at a slightly different height. The third strong split portion (90%)

of the fundamental, of beam-size was changed to 2 mm using a 4:1 telescope to match the beam size of the collimated signal beam and to avoid white light generation in the BBO crystal. The strong fundamental beam was overlapped spatially and temporally with the signal in the BBO crystal. To adjust the time delay between fundamental and signal pulses, the spherical gold mirror was mounted onto a manual translation stage. After the second pass through the BBO crystal, the signal and idler pulses were separated from residual fundamental and picked up using a gold mirror. By rotating the BBO crystal manually the frequency of signal (1.2-1.6 μm) and idler (2.4-1.6 μm) pulses can be tuned to generate the desired mid-IR frequency pulses.

Signal and idler pulses were separated using a dichroic beam-splitter (HT Idler and HR Signal). Due to group velocity mismatch signal and idler pulses are separated temporally while emerging from the BBO crystal. Because of the different polarizations of signal and idler pulses they experience different refractive indices while propagating through the BBO crystal and other transmissive optics. The idler beam was reflected by a gold mirror mounted on a manual translation stage to adjust the temporal delay between them. Both beams were overlapped spatially and temporally in the type I second order nonlinear $AgGaS_2$[5] crystal to generate mid-IR pulses. The signal(extraordinary) and idler(ordinary) polarizations are suitable for type I phase matching in $AgGaS_2$ crystal. By tilting the $AgGaS_2$ crystal, the optimal phase matching was achieved to generate intense mid-IR pulses. The mid-IR pulses are tunable from 2.5-20 μm with pulse energies that vary from 0.5 to 2 μJ depending on the mid-IR wavelength. The conversion efficiency was found to be decreasing with increasing mid-IR wavelength. The spectra of mid-IR pulses in the wavelength range from 2.5-10 μm is shown in the figure 3.5 . The long wave pass filter was used to suppress the residual signal and idler pulses. For two-color pump-probe experiments, we have designed two OPAs with subsequent difference frequency mixing stages of similar specifications.

[5] $AgGaS_2$ crystal, thickness = 0.75 mm, $\vartheta = 39^o$ and $\varphi = 45^o$

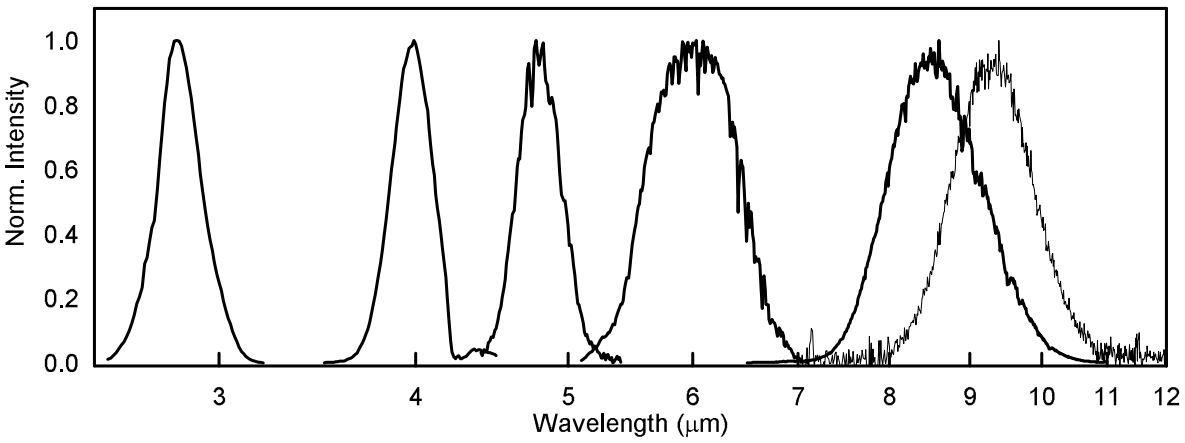

Figure 3.5: The normalized spectrum of tunable mid-IR pulses generated using OPA and DFG technique.

3.6 Pump-probe setup

Figure 3.6 depicts the experimental setup to perform pump-probe measurements. Tunable mid-IR and UV/VIS/NIR pulses can be used as a pump to excite the sample. The pump beam passes through blades of an optical chopper synchronized with the Q-switch of the regeneratively amplified Ti:sapphire laser. The chopper runs at half the frequency of the repetition rate (3 kHz) of the laser thereby blocking every second pump pulse. Mechanical delay stages[6] were used to control the temporal delay between pump and probe pulses.

The incoming mid-IR beam passes through a BaF_2 wedge ($< 1^o$). The BaF_2 wedge was tilted with respect to the incoming beam at an angle $< 40^o$. The small portion (4%) of the main beam reflected due to Fresnel reflection from the front and back surfaces of the wedge serve as the probe and reference beams. The beam size of the probe and reference beams were enlarged 1.5 times using a 2:3 reflective telescope which leads to a tighter focus of the probe beam (nearly 100 μm spot size when focused using 30^o off axis mirror) with respect to the pump beam (spot sizes when focused 150-175 μm). As a result the probing of a homogeneously excited sample volumes is realized. Probe and reference beams were transmitted through the same BaF_2 wedge for further propagation in the pump-probe setup. The major portion of the mid-IR beam transmitted through the wedge could be

[6]The delay stage for the UV/VIS/NIR pump beam has not shown in the schematic figure.

either used as pump beam for single color pump-probe experiments or dumped in case of two-color pump-probe experiments. For mid-IR pump-probe experiments[7], pump, probe

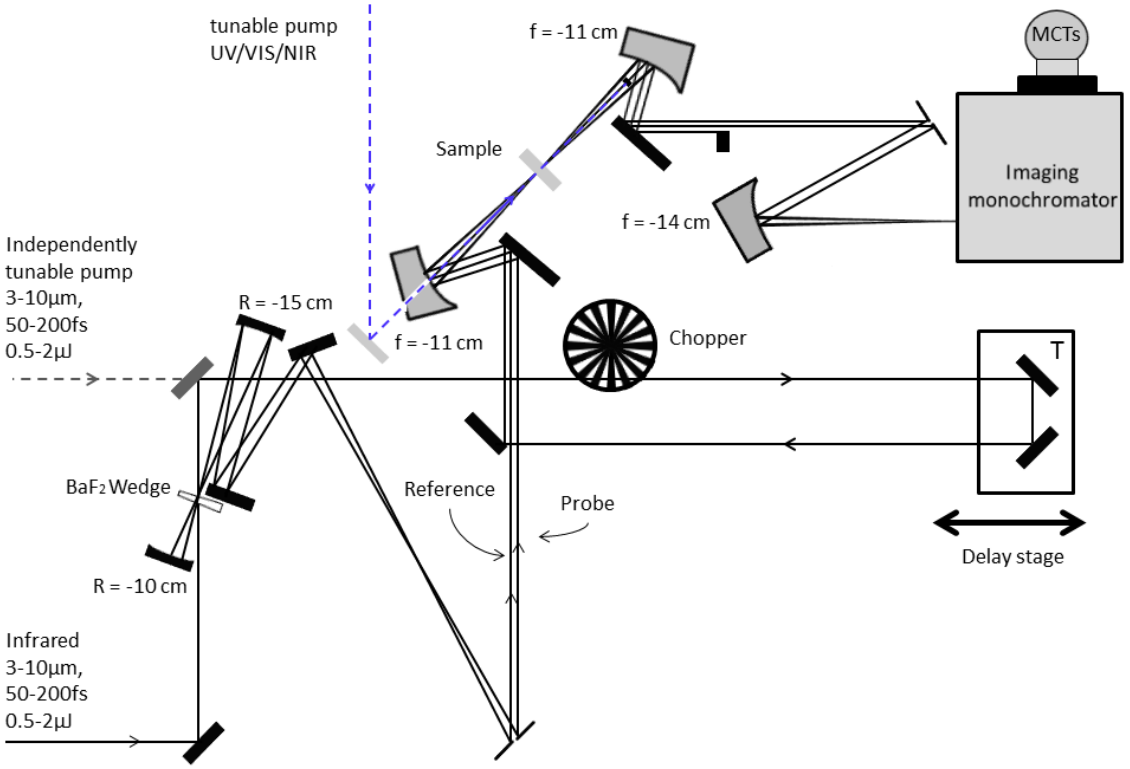

Figure 3.6: Sketch of the infrared pump-probe setup. The dashed blue and grey lines represent the pump beam path for UV/mid-IR-pump and mid-IR probe experiments. UV/Vis/NIR pump beam after passing through the sample blocked before the second parabolic mirror.

and reference pulses were focused into the sample and re-collimated afterwards using the 30° off-axis parabolic mirrors (f = 11 cm). After the sample interaction, the pump beam was blocked. The collimated probe and reference beams are focused into the entrance slit of the monochromator using the third 30° off-axis parabolic mirror (f = 14 cm). The 30° off-axis parabolic mirrors help to reduce astigmatism as mid-IR pulses have a

[7] In case of pumping in the UV/VIS spectral range, the pump pulses were focused into the sample using a plano-convex lens. Hereby, the pulses propagate through a hole in the center of the 30° off-axis parabolic mirror.

typical bandwidth of 250 cm^{-1}. Probe and reference pulses were spectrally dispersed in the monochromator and each spectral component was detected on a cryogenically cooled double array of 32-pixel infrared sensitive mercury cadmium telluride (MCT).

When UV/VIS/NIR pulses were used as a pump beam, the beam was focused using a plano-convex lens which passes through the through hole of 30^{o} off-axis parabolic mirror.

The pump and probe pulses were overlapped spatially in the sample, the reference beam was transmitted through the sample at a slightly off region from the pump-probe overlap. This helps to reduce signal fluctuations due to sample inhomogeneity and shot to shot variation of probe pulses. We calculate the absorbance change on a shot-to-shot basis as a function of delay time 't' and probe frequency 'ω' according to equation 3.4:

$$\Delta A(t,\omega) = -\log_{10}\left[\left(\frac{I(t,\omega)}{I_o(t,\omega)}\right)_{\text{Probe}} \cdot \left(\frac{I_o(t,\omega)}{I(t,\omega)}\right)_{\text{Reference}}\right] \tag{3.4}$$

Here I and I_o indicate intensities with and without pump excitation.

Absorption changes as small as 10^{-4} can be easily detected. The mid-IR pulses were as short as 100 fs. In order to avoid pulse dispersion, reflective optics was used except for the long-wave pass (LWP) filter and the BaF_2 wedge. It offers the additional advantage that the alignment of the pump-probe setup can be done using a Helium-Neon laser.

The pump-probe setup is enclosed in a box and was purged with N_2 gas to prevent infrared absorption by water vapor or carbon dioxide which would distort the pulse spectrum during the pulse propagation. The absorbance spectrum of ambient air at room temperature is shown in figure 3.7.

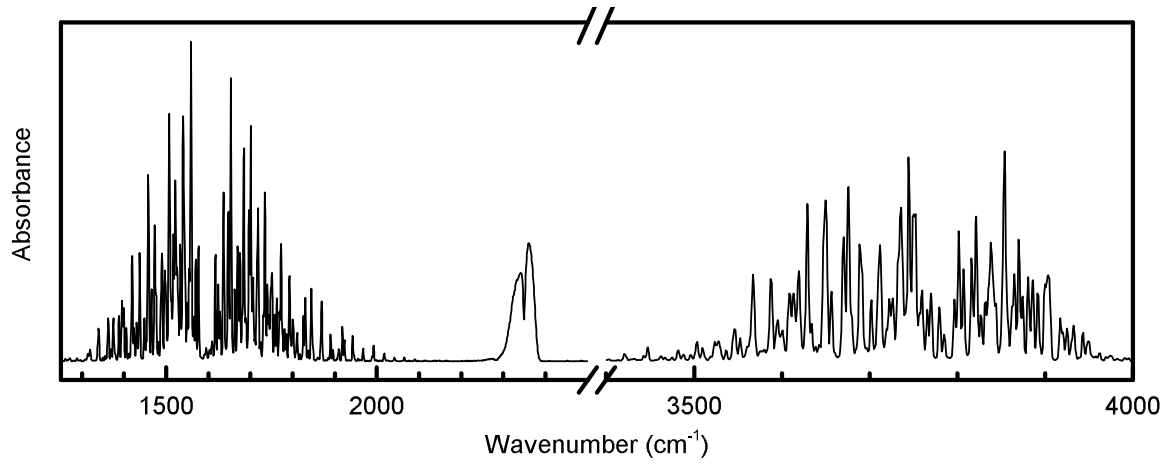

Figure 3.7: The infrared absorbance spectrum of air at ambient room temperature. The symmetric and asymmetric stretching vibrations of water vapor are centered at 3700 cm^{-1}. The water vapor bending vibrations are centered at 1600 cm^{-1}. The asymmetric stretching vibration of carbon dioxide (CO_2) absorbs around 2349 cm^{-1}.

The pump-probe set-up which has been shown in the figure 3.6 will be transformed into the two-dimensional infrared spectrometer (2DIR) in a pump-probe fashion. The technical parts necessary for building the 2DIR set-up had been designed and were ready to install. However, due to the lack of time and urgency of measuring graphite oxide and SESAM samples, the installation of 2DIR was put on hold. A proposed diagram of a 2DIR spectrometer in pump-probe geometry is shown in the following figure 3.8. It is sketched using Autodesk Inc. software package. The compact solid block which would house a Mach-Zehnder interferometer and customized mirror mounts were designed using the Autodesk Inc. software package. The Mach-Zehnder interferometer splits the entering mid-IR pulses into pump pulse 1 and 2 and collinearly combines them in the second beam splitter. The green line in the figure 3.8 represents Mach-Zehnder interferometer. The Mach-Zehnder spectrometer houses two beam-splitters, one for mid-IR and other for Visible light pulses and were displaced vertically in height as shown in the figure 3.9.

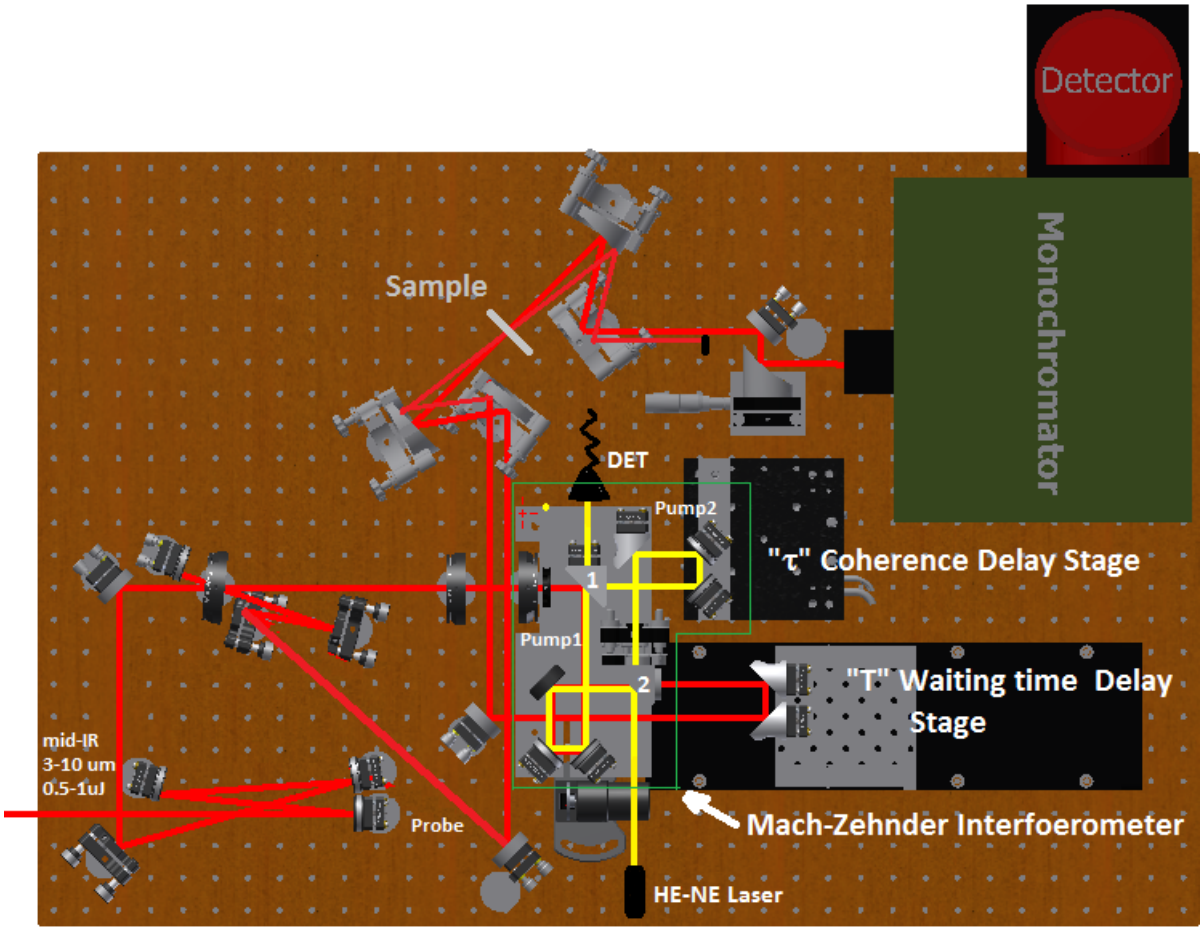

Figure 3.8: The proposed transformation of pump-probe set-up (cf. figure 3.6) into 2DIR set-up in pump-probe geometry. The red color line represents mid-IR beam path. The edifice within the green color lines is the Mach-Zehnder interferometer. The number 1 is beam splitting mount to generate the two pump beams. The number 2 is the beam combing mount which collinearly unites the two pump beams. The yellow line is the He-Ne laser beam propagation path which was displaced in height in comparison to the mid-IR beam path.

The He-Ne laser would help to measure very precise delay between the pump 1 and pump 2 pulses generated by coherent delay stage by monitoring interference pattern on the detector. The 50-50% beam splitters will be used in the beam splitting and combining mounts 1 and 2 respectively which loses 50% power of the beam entering into the spectrometer.

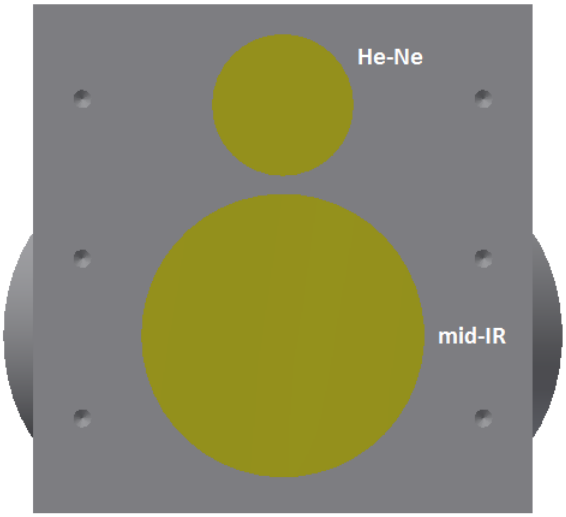

Figure 3.9: Mirrors mount for beam splitting and recombining. The path for He-Ne and mid-IR light pulses are separated vertically.

3.7 Characterization of ultrashort laser pulses

The precise pulse characterization has vital importance to estimate dynamics accurately on an ultrafast time scale as in some cases resonant and non-resonant contributions distort the signal resulting from the sample and sample enclosing windows. There are many ways of pulse characterizations: intensity autocorrelation, interferometric autocorrelation, frequency-resolved optical gating, spectral phase interferometry for direct electric-field reconstruction etc.

For the investigation of carrier relaxation dynamics in a semiconductor saturable absorber (SESAM), the 2 μm idler pulses were used in the single color pump-probe experiments had to be characterized first. The pulse characterization was accomplished with the help of an intensity autocorrelator (figure 3.10), the results are shown in the figure 3.11. In an autocorrelator, the incoming beam was split by a 50:50 beam splitter. These two beams were focused into a nonlinear crystal. In the autocorrelator design the beams propagate in a non-collinear fashion through the crystal. One of the beam passes over a delay stage for creating a temporal delay between the pulses. Spatial and temporal overlap between two ultrashort pulses in a second-order nonlinear crystal[8] leads to SFG

[8]BBO crystal, thickness = 1 mm, $\vartheta = 30^{o}$ and $\varphi = 90^{o}$

(sum frequency generation).

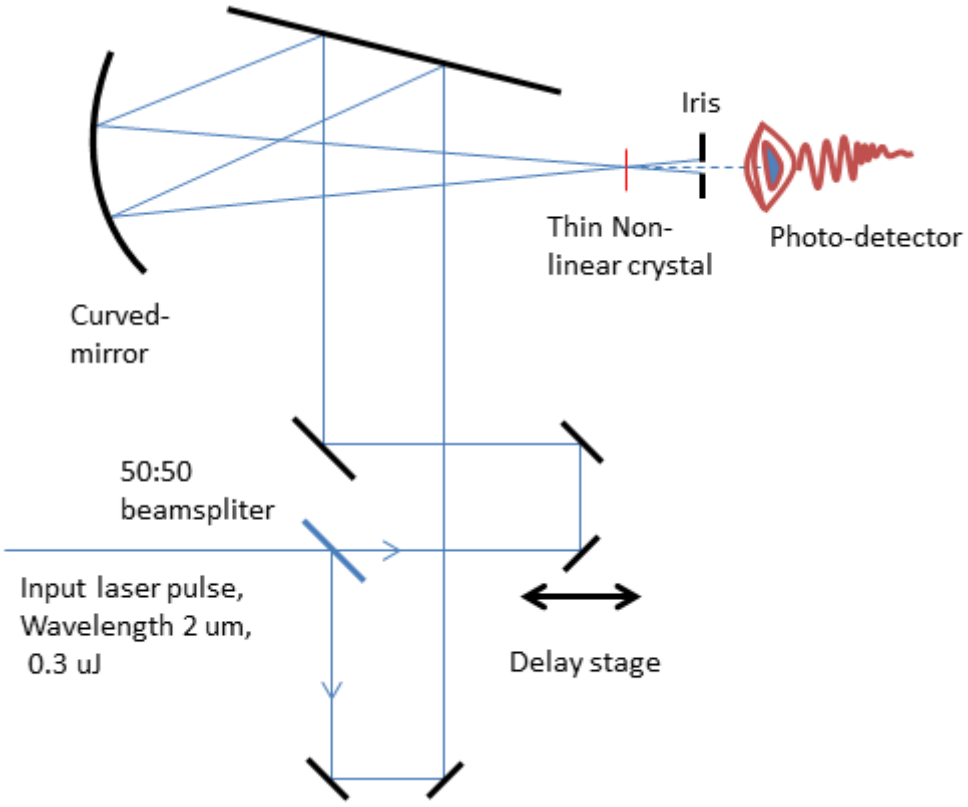

Figure 3.10: Typical autocorrelation set-up.

The SFG intensity depends on the temporal (mis)match between both beams. By scanning the relative time delay the pulse duration of the initial pulse can be retrieved. The SFG signal dependence on the temporal delay is given by

$$I_{ac}(\tau) = \int_{-\infty}^{\infty} I(t)I(t-\tau)dt \tag{3.5}$$

For Gaussian-shaped pulses, the autocorrelation signal $I_{ac}(\tau)$ will also be a Gaussian shape with pulse width σ that is $\sqrt{2}$ - times the width of the original I(t) incoming beam.

Spectrally resolved cross-correlation measurements were performed to determine the experimental time resolution and to find the temporal overlap between pump and probe pulses. Two materials [9] were used to measure cross-correlations: zinc selenide (ZnSe)

[9] ZnSe (zinc selenide crystal 0.5 mm thickness) and Ge (germanium crystal 0.05 mm thickness) crystals

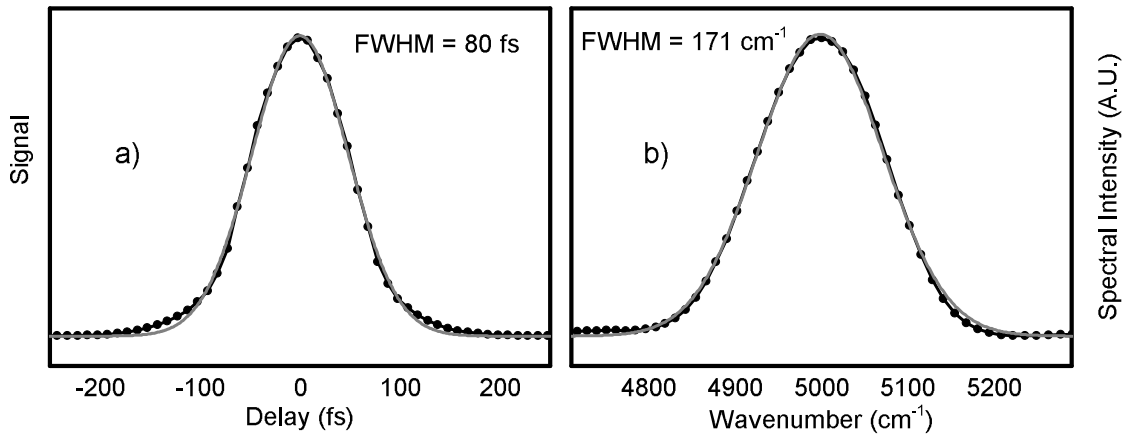

Figure 3.11: a) Autocorrelation of 2 μm pulses. b) The corresponding pulse spectrum.

in case of UV/VIS/NIR- pump/IR-probe experiments and germanium in case of mid-IR pump-probe experiments.

In ZnSe the interaction of UV/VIS/NIR pulses leads to the instantaneous excitation of charge carriers. The transient electron plasma can be probed by mid-IR pulses. In Ge two-photon absorption of intense and short mid-IR pulses had exploited for cross-correlation experiments.

The observed signal I(τ) is a temporal convolution of the response function of ZnSe/Ge R(t) with the cross convolution of pump and probe pulses as given in the following equation 3.6.

$$I(\tau)_{cc} = \int_{-\infty}^{\infty} R(t-\tau)G(t)dt \tag{3.6}$$

The response function R(t) is described by a Heaviside step function H(t), H(t)=R(t), with $H(t) = 0$ for $t < 0$ and $H(t) = 1$ for $t >$ or $= 0$. Assuming both pump and probe pulses are Gaussian in shape their convolution will also be a Gaussian shape. The measured cross-correlation of UV (266 nm) pump and mid-IR (1650 cm^{-1}) probe has shown in the following figure 3.12.

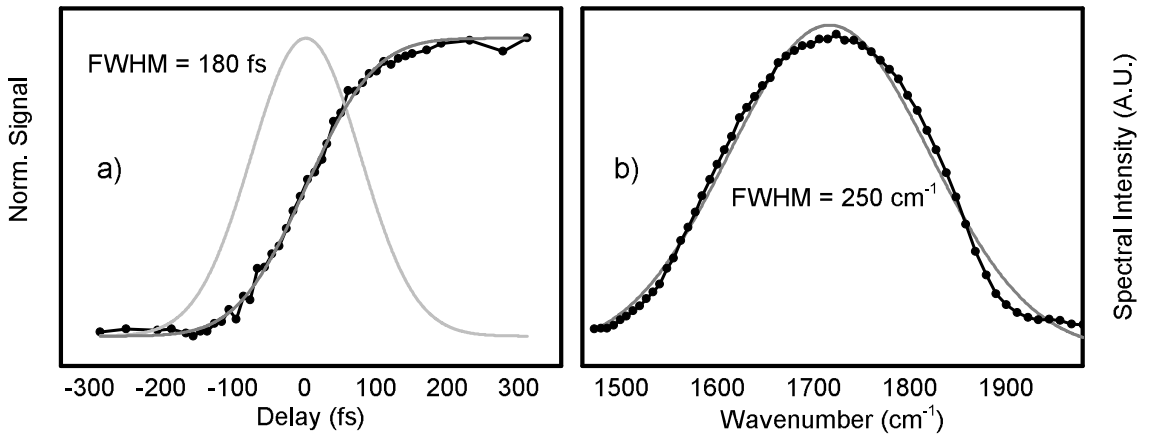

Figure 3.12: a) Cross-correlation signal measured in a 500 μm thick ZnSe crystal using a UV-pump and IR-probe experiment. The probe pulses were centered at 1650 cm^{-1} and had pulse width of 250 cm^{-1}. The corresponding instrument time resolution of pump-probe experiment was 180 fs. The time derivative of the cross-correlation signal is shown in a gray line. b) The corresponding probe pulse spectrum with a superimposed Gaussian fit.

Chapter 4

Ultrafast dynamics of graphite oxide

4.1 Introduction

Graphene is an interesting two-dimensional material due to its mechanical, electrical, thermal and optical properties and its potential applications in future electronics and photonics technologies. The research on graphene has increased substantially since the year 2010 when the Nobel prize in Physics was awarded to Andre Geim and Konstantin Novoselov for their discovery of fabricating single layer graphene from graphite using scotch tape. Insofar, many methods have been developed to synthesize graphene mainly grouped into six which are: mechanical cleavage, epitaxial growth, chemical vapor deposition, total organic synthesis and chemical method. All these methods have more or less some disadvantages. However, the chemical method is suitable for low cost and mass production of graphene. The disadvantage of it is that the synthesized graphene has many defects, which have to be removed later using various reduction methods. Defective graphene is known as graphene oxide which is a derivative form of graphene. The history of graphene oxide synthesis goes dates back to 1855; B. C. Brodie of Oxford University was the first to report graphite oxide synthesis by treating graphite with a mixture of potassium chloride and fuming nitric acid. He reported graphite oxide sheets of 0.05 mm thickness [56]. A similar approach was espoused by Staudenmair in 1898 and Hummer in 1958 for the production and characterization of graphite oxide [57, 58]. The graphite oxide further treated with basic solutions followed by ultrasonication to extract single-layer

sheets of graphene oxide [59]. The cartoon of the chemical synthesis route of the graphene oxide single layer membranes have been shown in the following figure 4.1. Graphene oxide has many oxygen functional groups attached to its basal plane and edges. Scientists have reported that graphene oxide can be chemically transformed by reduction methods into a graphene-like material [59–61].

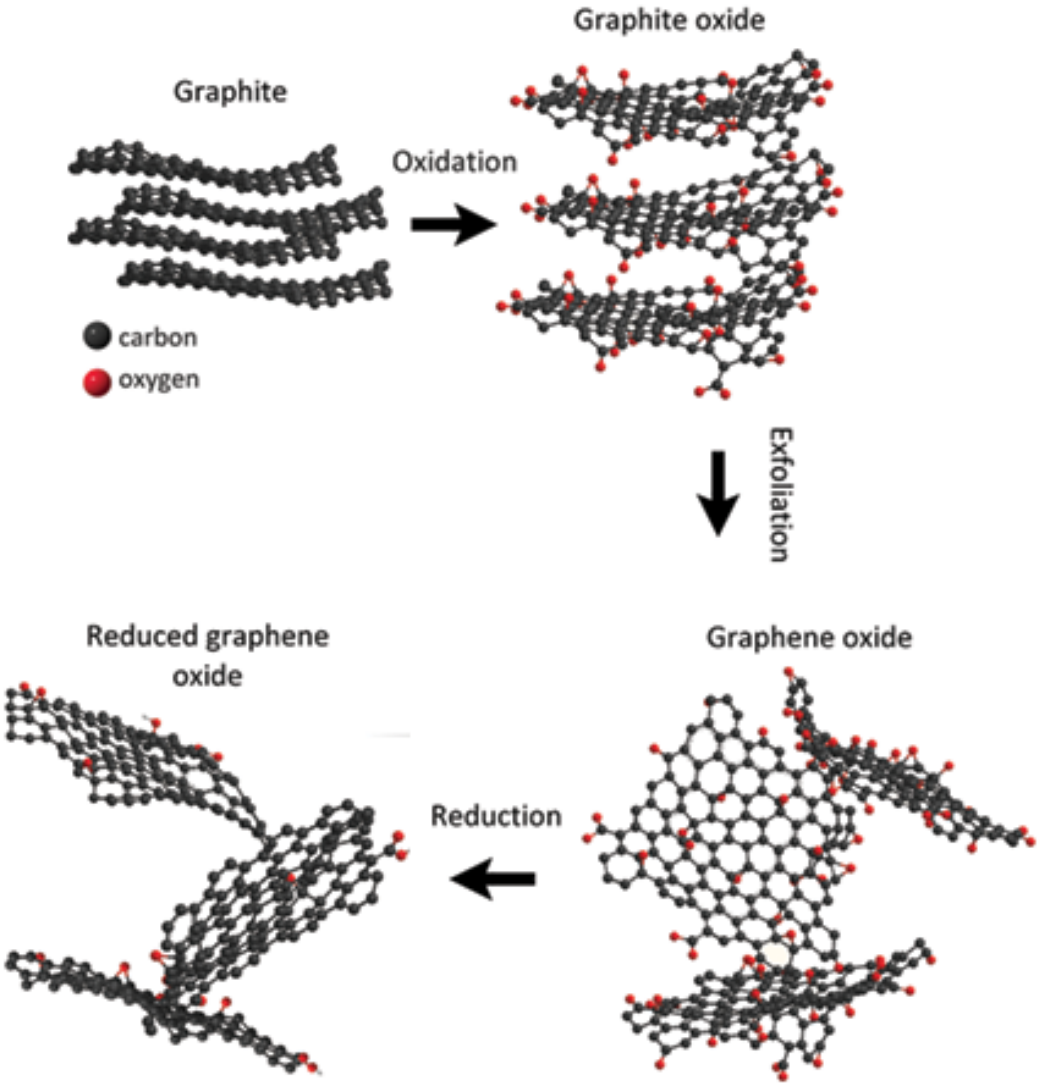

Figure 4.1: Schematic representation of graphene synthesis mechanism using a chemical route. Figure adopted from [62].

4.2 Molecular and electronic band structure

4.2.1 Graphene

Graphene is a two-dimensional honeycomb lattice structure of carbon atoms. The lattice constant is the closest distance between the two carbon atoms which is 1.42 Å in graphene. The electronic configuration of carbon is 1s2 2s2 2p2. It can form four bonds with neighboring carbon atoms. In graphene, the carbon atoms are sp^2 hybridized in which 1s, 2px and 2py orbitals form in plane three strong covalent σ-bonds with nearest carbon atoms and the final 2pz orbital forms π bond out of plane of the lattice structure. The three strong sigma bonds render stability to the two dimensional graphene structure and the π bonds hybridize together with other π bond of carbon atom to form π and π^* bands. These bands are playing the major role in the electronic properties of graphene. Graphene is a zero band gap semiconductor, also known as a semimetal due to its valence band and conduction band which are meeting at Dirac point where it has zero electron density of state. There are in total six Dirac point locations in momentum space of the graphene Brillouin zone. The electronic band structure of graphene was calculated by Wallace [63] in 1947 using the tight binding model with the nearest neighbor approximation having the following form:

$$E = \pm\sqrt{\gamma_0^2\left(1 + 4\cos^2\frac{k_y a}{2} + 4\cos^2\frac{k_y a}{2}\cdot\cos^2\frac{k_x\sqrt{3}a}{2}\right)} \tag{4.1}$$

Where, γ_o is the nearest neighboring hopping energy, a is the lattice constant, k is the electron propagation wave vector.

The negative and positive signs of the above equation represent respectively the valence and conduction bands. At the Dirac point the conduction and valence bands meet without any gap as shown in the following figure 4.2.

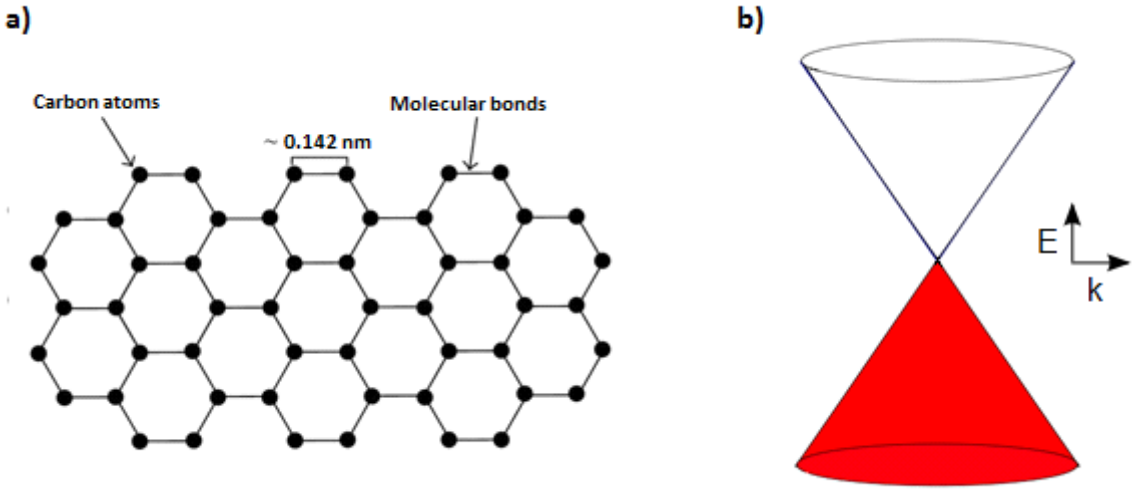

Figure 4.2: a) Two dimensional graphene structure and b) electronic band structure of two dimensional graphene at the Dirac point. The conical band in red color represents filled valence band and empty top band represents the conduction band [64].

4.2.2 Graphene oxide

Graphene oxide has a complex molecular structure compared to graphene. It has an irregular two dimensional honeycomb structure of carbon atoms [65]. Additionally, the oxygen functional groups are attached to the basal plane and outer edges of the two dimensional carbon structure as shown in the following figure 4.3. In graphene oxide, two types of carbons orbital hybridization, sp^2 and sp^3 exist. It clearly indicates there are some small graphene-like domains in graphene oxide structure. The carbon atoms which have oxygen functionalities attached are sp^3 hybridized [65]. These carbon atoms form four strong covalent σ-bonds, three with nearest carbon atoms and one with oxygen functional group. The structure of graphene oxide depends on the synthesis method and degree of oxidation. The typical layer thickness of 1.1±0.2 nm has been reported for graphene oxide sheets [66, 67]. The electronic structure of graphene oxide is also very complicated. Due to oxidation of the graphene by strong acids the gap between the valence and conduction bands opens and as a result of which the material becomes an

insulator. However, it has also been reported that due to the attachment of oxygen functionalities to carbon atoms the mid gap electron trapping states are formed between the valence and conduction bands [68, 69]. The interesting property of graphene oxide is its band gap which can be tuned by using reduction methods such as photo, thermal or chemical methods. The band gap of graphene oxide can be tuned from 5 to 1 eV by chemical reduction using hydrazine [70]. Another interesting property of graphene oxide is hydrophilicity, it absorbs water molecules when it comes in contact with the bulk water or water vapors [71]. The water intercalation in graphene oxide layers increases interlayer distance depending upon the degree of hydration [23]. However, complete water removal has not yet been reported.

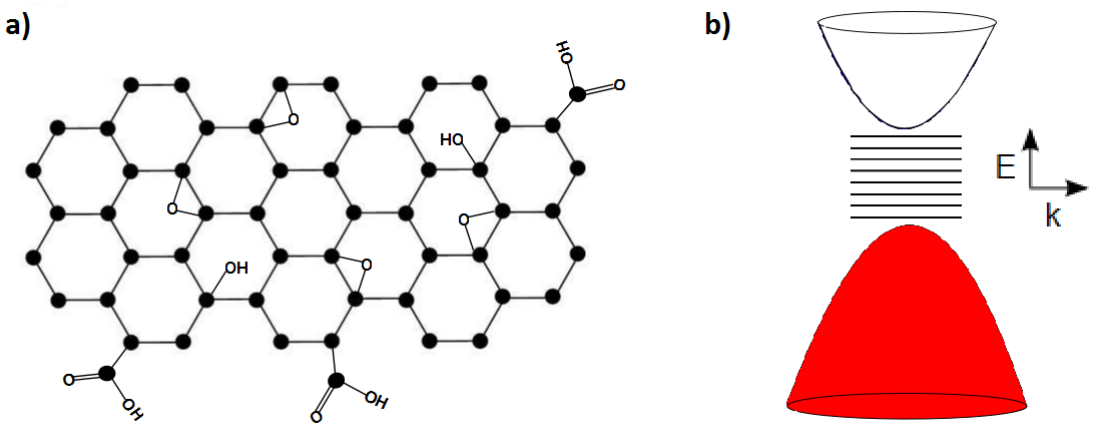

Figure 4.3: Graphene oxide a) two dimensional structure and b) schematic representation of electronic band structure. The oxidation of graphene generate gap between the valence and conduction band with intermediate states. The red cone represents the valence band and white cone represents the conduction band. [69].

4.3 Ultrafast processes in Graphene

Initially, our objective was to uncover the carrier dynamics and intercalated water dynamics in graphite oxide in mid-infrared spectral region. Since, the graphite oxide has graphene-like regions, it is imperative to understand what mechanisms or pathways exists

when carriers and or vibrationally active sites are excited to higher energy levels. In the following subsections, processes occurring in graphene upon photo-excitation on ultrafast timescales have been discussed.

Carrier-carrier scattering

In this process, the carriers excited into upper energy states of the conduction band, are cooled by carrier-carrier scattering. This process takes place at very fast time scale (within 10-30 fs) in graphene. In free standing thin (20-30 nm) graphite film the rapid intraband carrier equilibration takes place in 30 fs, which is studied using optical pump-probe technique with 7 fs time resolution [72]. For epitaxial bilayer graphene the intraband carrier-carrier scattering distribution has been reported on a 8±3 fs time scale [73]. Similarly, in exfoliated single layer graphene, a 10 fs time scale of carrier scattering has been reported using two pulse correlation technique [74]. However, Sunil Kumar et al. has reported 130 fs carrier scattering time for graphene oxide suspended in water using 80 fs time resolution of pump-probe experiment [22]. Since, carrier-carrier scattering processes are taking place at very fast time scales, very few reports are available due to the requirement of very high and precise time resolution of pump-probe experiments.

Carrier-optical phonon scattering

In this process, carriers in the conduction band transfer energy to the optical phononic vibrational modes of crystal lattice. The strong coupling between the carrier and optical phonon has measured in graphite with optical excitation [75]. The optical phonon scattering lifetimes in graphite and single layer graphene reported were 2.4 and 1.2 ps respectively measured at room temperature using time-resolved anti-Stokes raman scattering [76]. The few picoseconds carrier-optical relaxation time in monolayer and few layer graphene oxide has also been reported [77]. The optical phonon is one of the dominant mediation steps in the carrier relaxation pathway [78]. The electron-optical phonon scattering is frequency dependent reported by Jingzhi et al. performing experiments on the CVD grown graphene [79].

Carrier-acoustic phonon scattering

This scattering mechanism is analogous to the carrier-optical phonon scattering, the distinction here is that the carriers are coupled with acoustic phonon modes of the crystal lattice. Theoder Norris et al. has observed emission of high energy phonons and determined the electron cooling by electronic-acoustic phonon scattering on the time scale of 1 ps for highly doped layers, and 4-11 ps in undoped epitaxial graphene layers [80]. The electronic temperature in metallic graphene at high bias proportional to the square-root of bias voltage which illustrates the 2D acoustic phonon cooling mechanism [81]. The electron-acoustic phonon scattering is independent of carrier density in monolayer graphene on SiO_2 substrate. Nika et al. discussed in his article on two dimensional phonon transport in graphene, the acoustic phonons are the main carriers of heat at room temperature [82].

Optical phonon-acoustic phonon scattering

In few hundred femtoseconds after photo-excitation the carriers lose most of their energy to the generation of hot optical phonons which then present the main bottleneck to subsequent cooling mechanism via acoustic phonons [83]. Shang et al. reported carrier dynamics results using pump-probe spectroscopy on graphene films on CaF_2 in mid-infrared region, it had been proposed that the relaxation kinetics has two decay times, the fast time component $\sim$ 200 fs has attributed to ultrafast intra-band and inter-band decay channels and slow time component $\sim$ 1.5 ps assigned to an optical phonon-acoustic phonon scattering [84].

Auger processes

There are three main auger processes that can occur in graphene. First process: when an electron in a conduction band de-excite into a valence band, the released energy is absorbed by the other electron in the conduction band to reach a higher state in the band known as Auger recombination. Second process: after de-excitation of electrons from the conduction band to the valence band, the electron in the valence band absorbs the released

energy and moves to the conduction band and the process is known as impact ionization. Third process: the electron in an upper level in conduction band releases energy and reaches to a lower levels in the conduction band. Then, the electron in the valence band absorbs this energy and moves to the lower state in the conduction band which is known as carrier multiplication. Andrea Tomadin et al. used semi-classical Boltzmann equation and with collision integral to understand the nonequllibrium electron dynamics in graphene via collinear scattering, Auger processes and impact of screening [85]. Brida et al. has reported the carrier multiplication process in CVD grown monolayer graphene on copper foil [86]. The carrier multiplication process in two dimensional graphene is a function of photon energy, graphene doping and dielectric constant [68].

Electron plasmon scattering

There have been abundant reports on the electron-plasmon scattering in graphene. Long Zu et al. demonstrated tuning of graphene plasmon resonance over broad terahertz range and light-plasmon coupling [87]. In addition, it has also been pointed out the potential of graphene based terahertz meta-materials [88]. Fei et al. has reported the gate voltage controls propagation of plasmons in graphene/SiO_2/Si structures [89]. The angle resolved photoemission spectroscopy on graphene has reported the states at the Dirac point found strongly interacting with plasmon frequencies [90]. The strong coupling of plasmons with electrons influence the band opening in epitaxially grown graphene layers on silicon carbide substrate [91]. In photo-excited graphene, Farhan Rana et al. determined the plasmon emission and absorption on few tens of femtoseconds to hundreds of picoseconds time scale which is dependent upon the carrier energy, carrier density, temperature and plasmon dispersion [92].

Electron-hole recombination

There are several pathways to electron-hole recombination which include electron-electron scattering, electron-phonon scattering, auger recombination, plasmon emission and photon emission. All these processes except photon emission have been discussed above.

The broadband photoluminescence in graphene under excitation of intense laser pulse has been demonstrated by Lui et al. [93]. As there exists no bandgap in graphene the idea of photoluminescence was farce to imagine. Wei-Tao Liu et al. endorsed the existence of photoluminescence in graphene induced by laser irradiation [94]. In graphene oxide the strong broadband photoluminescence in the visible range is reported by Donghe du et al. [95]. The reason of strong photoluminescence in graphene oxide is the opening of the gap between valence and conduction band and the formation of localized states in or at the bottom of the conduction band [95].

4.4 Literature study of graphene oxide

In this section, the historical evidences in the spectroscopic studies of graphene oxide have been presented.

Chemistry background

In 1858, B. Brodie first prepared graphitic oxide from Ceylon graphite [56]. Also, in 1958 Hummer and his coworkers modified Brodie's synthesis method to achieve large scale safe and fast production of graphite oxide [57]. Over the years, many methods have been developed to synthesize graphite oxide with little modifications in the three principal methods i.e. Brodie, Hummer and Staudenmaier [58]. The single layer graphene oxide production by dissolving graphite oxide in many solvents (e.g. H_2O, DMF, etc.) with ultra-sonication treatment has been reported by many [96–98]. The chemistry of graphene oxide is more involved in the reduction to graphene like material. The ultimate goal for every graphene oxide synthesizer would be to fabricate graphene in the end, since the zero band gap material is of not much use in semiconductor industry. Graphene oxide is a good start to change its optical properties by reduction methods to form reduced graphene oxide which has properties similar of graphene and easy to tune bandgap by reduction methods. For mass scale production of graphite oxide, thermal, chemical and photo-reduction methods have been reported [21, 70, 99–101]. The thermal and chemical exfoliation routes have been explored by Mucik et al., who claimed that the band gap and

oxygen content is tunable [60]. The vast accounts about the structure and properties is presented by Shun et al., where it has been shown that the graphene oxide properties are dependent on the type and distribution of functional groups, defects and holes from missing carbon atoms [102]. The structure of graphene oxide is debatable, different synthesis methods and models predict different C/O ratio and structure models [103]. The chemical structure proposed by Szabo et al. based on analytic spectroscopic techniques has predicted that graphene oxide has two kinds of regions trans-linked cyclohexane chains and ribbons of flat hexagons with C=C double bonds and functional groups such as tertiary hydroxyl (-OH), 1, 3 ether, ketone, quinone and phenol [104].

Density functional calculations suggest that the functional group induces interesting electronic properties in graphene [105]. In the same study, it has also been reported that the hydroxyl and ether groups aggregate on the graphene plane and the band gap can be tuned from 0-4 eV [105]. Another study using ab initio density functional calculations has been reported that the varying concentration of epoxy and hydroxyl functional groups from 25 to 75%, the plasmon spectra of $\pi + \sigma$ band shifts from 1-3 eV. The band gap opening due to adsorption of atomic oxygen on epitaxially grown graphene on SiC substrate distorts π bands at K-point of graphene electronic structure [106]. From the study of atomic and electronic structures of single and multilayer graphene oxide sheets using annular dark field imaging, it corroborates the graphene oxide has amorphous structure due to oxidation of aromatic carbon rings [107]. However, the controlled deoxygenation of graphene oxide leads to formation of increase in sp^2 domains also known as graphene like regions [108]. The functionalization of graphene sheet leads to opening of the gap at the Dirac points [109]. The bandgap tailoring of graphene oxide by infrared irradiation and defect assisted localized states is possible [110] and the Drude-like response in far infrared region and improved conductivity of electric mobility in reduced graphene oxide has studied in detail by [111].

Band gap tuning

The graphene oxide is a precursor material to synthesize reduced graphene oxide. The controlled stepwise reduction of graphene and its consequential evolution in band gap from

3.5 eV to 0.02 eV has been reported using chemical and thermal ways [70, 100, 101, 112, 113]. It has been suggested that there is a coupling of electronic states with asymmetric stretching modes of unreported structure probably of oxygen atoms aggregated at the edges cause defects in reduced graphene oxide. They further proposed the strong infrared absorption in phase with phonon mode due to removal of oxygen containing functional group and formation of graphene like regions [99]. Time resolved UV-pump and Visible-probe measurements on graphene oxide dissolved in water explains the photo-reduction of graphene oxide takes place on picoseconds time scale, where the strong UV-pump causes photoionization of solvent and the generated secondary electrons play major role in the photo-reduction mechanism of graphene oxide [21].

Luminescence characteristics

The luminescence spectroscopy of graphene oxide helps to understand its electronic band structure. The chemical reduction of graphene oxide transforms its electronic band structure as a result of which the emission spectrum gets modified [114]. The broadband photoluminescence spectrum of graphene oxide arises due to loss of sp^2 hybridized aromatic hexagonal carbon rings [114]. The blue photoluminescence from a monolayer graphene oxide has also been reported [115], where the photoluminescence intensity depends on the localized sp^2 domain in graphene oxide structure due to the removal of oxygen while progressive reduction [115]. The time resolved photoluminescence measurements on graphene oxide and reduced graphene oxide show the substantive energy redistribution and relaxation among the emission states occur at picoseconds time scale which leads to the red shift of the emission spectrum. On the contrary the blue shift in emission spectrum in case of time integrated spectra helps to understand the distribution of dipole coupled states [116].

The fluorescence measurements on graphene oxide have also been reported which occurs from electronic states generated due to defects formed into graphene like structure due to oxygen-like functionalities [117–121]. The photo-reduction dynamics of monolayer graphene oxide using time correlated single photon counting technology assigned fast lifetime of 0.14 ns to the confined sp^2 domains in graphene oxide and the longer

lifetime constant of 1.37 ns to the hydroxyl group which depended strongly on irradiation time [121]. The new derivative of graphene oxide that is carbon nanodots has been studied due to its interesting optical and electronic properties [122–124]. The carbon nanodots are fabricated by carving out the graphene like portions from graphene oxide [122]. The reasons mentioned by Lei Wang and others who studied fluorescence properties of nanodots are that the sp^2 domains and attachment of oxygen functionalities at the boundaries do passivate the nanodots. A femtosecond resolved up-conversion technique assigned four time constants. The fast relaxation time constant of 400 fs has assigned to the fast trappings of carriers from carbon nanodomains to the surface states, a few picoseconds attributed to optical phonon scattering, tens of picoseconds to acoustic phonon scattering and few nanoseconds to carrier recombination [123]. Apart from photoluminescence and fluorescence study of graphene oxide some people have reported chemiluminescence and thermoluminescence. Lixia Zhao et al. have reported chemiluminescence from carbon dots in presence of strong alkaline solutions such as KOH or NaOH. The mechanism of chemiluminescence arises due to radiative recombination of electrons injected by chemical reduction of carbon nanodots and thermally generated holes [125]. The thermoluminescence behavior of graphene oxide, reduced graphene oxide and graphene-nano ZnS compounds using different gamma (γ) radiation doses 1 Gy to 50 kGy has been studied. The thermoluminescence could not observed in reduced graphene oxide. The absence of thermoluminescence in reduced graphene oxide was not discussed there [126].

Intercalated molecular dynamics

The hydrophilic nature of graphene oxide is contrasting with the intercalation compound of graphite, the intercalation of water molecules between the layers of graphene oxide has been reported by many [23, 127–129]. Some researchers have studied hydration behavior and intercalated water molecular dynamics of graphene oxide. It has been claimed that the increase in the hydration level in the graphene oxide leads to increase in the interlayer distance between the graphene layers. In 2006, A. Lerf et al. studied the effect of the degree of hydration on the water dynamics and graphene oxide interlayer spacing using the time of flight neutron scattering and X-ray diffraction pattern, where they found,

when the relative humidity level varied from 45, 75 to 100 %, the interlayer distance between the graphene oxide layers changed from 8, 9 to 11.5 Å respectively. Further, they demonstrated three types of motions happening in a such environment due to the hydration level of the graphene oxide. At 100 % relative humidity, they had observed translation motion of water molecules. At 45 and 75 % relative humidity, they ruled out this proposition as with the water removal the interlayer spacing decreases. There assigned two types of localized motions of water molecules which have different activation energies at these two humidity levels, one of which were assigned to the confined water molecules intercalated between the graphene oxide layers where functional groups are attached to graphene [127]. Similar observations have been drawn by many researchers on hydrophilic nature of graphene oxide. Also, Alexander Buchsteiner et al. had reported the graphene oxide interlayer spacing varies from 6 to 12 Å with the increase of the humidity level [23]. The interlayer water remains bounded tightly and did not show translation motion while at high humidity levels, the excess water distributes over the non-interlayer space which acts like confined bulk water. An interesting article by Muge Acik et al. has reported that the reduction chemistry plays differently for monolayer graphene oxide and multilayer graphene oxide films due to the presence of water molecules between the layers of multilayer graphene oxide [99]. Like water, methanol can intercalate between the graphene oxide layers [130]. The intercalation of water-methanol mixture between graphene oxide layers has been reported where the graphene oxide is intercalated by methanol when exposed to water-methanol mixture and the methanol fraction found increased in the range of 20-100%, but insertion of water molecules occurs when water fraction increase up to 90% [130]. The role of hydrogen bonding of intercalated water with itself and functional groups of graphene oxide play a major role in tuning the mechanical properties of graphene oxide paper and their composites [131, 132]. The intercalation property of water in graphene oxide layers is well known, some researchers attempted to intercalate graphene oxide layers with gases [133, 134]. Among the CO_2, CH_4, H_2 and N_2 gas molecules only CO_2 intercalation in graphene oxide has been reported and the intercalation with rest other gases is possible when graphene oxide swelled with water [133]. Similarly, K. Rohini et al. has studied small molecules such as HF, H_2O and NH_3

intercalation in graphene and graphene oxide, where they found the interaction is stronger with bilayer structure than the monolayer substrate [134].

Time-resolved dynamics

The time resolved pump-probe measurements on graphene oxide helps to understand the carrier-carrier dynamics, carrier-phonon coupling and electron-hole recombination processes that occur on ultrafast time scale.

In 2011, Sreejith et al. used graphene oxide dispersion in water to shed light upon the carriers in the excited state using pump-probe experiment with 400 nm as a pump and visible light as a probe. There found all dynamics happened between 0.8 to >400 ps which is attributed to the phonon and trapping states. They had put more insights on the trapping states which are generated in graphene oxide during chemical exfoliation of graphite when treated with strong oxidizing acids [69]. Zhi-Bo Liu et al. had reported ultrafast relaxation dynamics in single and few-layered graphene oxide using degenerate pump-probe technique at 800 nm wavelength. They concluded that the pump intensity dependent contributions from sp^2 and sp^3 hybridized carbon atoms in graphene oxide are responsible for the pump-probe signal [77]. In a few-layered graphene oxide dispersed in organic solvent, the fast decay constants were assigned to the hot carrier relaxation and strong saturable absorption comparable to the reduced graphene oxide due to the presence of large fraction of sp^2 carbon domains [135]. Similar studies about the contribution of sp^2 carbon domains to the fast times scales of pump-probe traces have been corroborated in [122,136]. An optical pump and terahertz probe measurements on graphene oxide samples suggested the carrier decay is dominated by defect trapping states with monoexponential decay model. In annealed samples, contribution from auger recombination have been proposed which induced a second channel for carrier relaxation [68]. So, it shows that the graphene oxide carrier dynamics are mostly dominated by the defect trapping states due to oxygen functionalities. The above mentioned similar pump-probe techniques have been used for studying carrier relaxation dynamics. In the reduced graphene oxide, the trapping states can be removed during reduction process, which suggests the relaxation dynamics of reduced graphene oxide could be similar to that of graphene dynamics [22,

137–141]. The ultrafast phonon dynamics of NaOH treated graphene oxide have been reported which suggests due to NaOH treatment the epoxide group decomposes into hydroxyls and –ONa group. The two time constants 0.17 ps and 2 ps determined were attributed to the fast relaxation process of coupling of hydroxyl and –ONa groups and low energy acoustic phonon mediated scattering respectively [142]. The thermal transport in monolayer graphene oxide provides insights onto the phonon engineering, where the oxidation of carbon in graphene reduces the thermal conductivity and density of state of the phonon mode (C=C) have been reported [143].

Saturable absorption

The saturable absorption property of graphene oxide has been aptly used for the fabrication of saturable absorbers in the Q-switched laser development [144, 145]. Yong Wang et al. has demonstrated the graphene oxide saturable absorber for Q-switched Nd:$GdVO_4$ laser which generated 104 ns pulses and 1.22 W average output power [144]. Similar approach had been used by Grzegorz Sobon in the development of Er-doped passively mode locked fiber laser operated with 400 fs pulses centered at 1560 nm with 9 nm bandwidth [144]. Graphene oxide has been discussed severely for its application in solar cell industry. It has been used in combination with semiconductor nanoparticle composite materials to enhance efficiency of solar cells [146, 147].

4.5 Experimental

Sample details

The graphene oxide membranes were procured from Graphenea S.A. Spain. It were prepared using a specialized Hummers method. The millimeter sized natural graphite flakes were treated with concentrated sulfuric acid, sodium nitrate, and potassium permanganate. These strong oxidizing agents oxidize graphene layers as a result of which the distance between the layers increases. These oxidized graphene layers are exfoliated into single layer graphene oxide by ultrasonication in water followed by centrifugation to re-

move remaining few-layer crystals. Finally, the resulting graphene oxide suspension was used for the making of self-standing membranes by vacuum filtration method where the graphene oxide suspension passed through Anodisc alumina membranes. The thickness of the film can be controlled by varying the volume of the graphene oxide suspension. The graphene oxide membranes fabricated were 4 cm in diameter and 12-15 μm thick. The detailed information about the fabrication of the graphene oxide membrane can be found elsewhere [148, 149].

Figure 4.4: Picture of the graphite oxide membrane procured from Graphenea S.A.

UV-visible absorption spectroscopy

The optical absorption spectroscopy comprises the ultraviolet-visible-near infrared electromagnetic light spectrum. It is used to study the electronic absorption of atoms, molecules, liquids and solids. The graphene oxide monolayer is transparent in this region due to its atomically thin nature [150]. The typical optical absorption spectrum of graphene oxide has shown in the following figure 4.5 a). The broad absorption peak in the 225-275 nm spectral region is attributed to the $\pi \longrightarrow \pi^*$ transitions of sp^2 hybridized carbon atoms [151].

Another peak appears as a shoulder around 300 nm is often attributed to the $n \longrightarrow \pi^*$ transitions of C=O carbonyl group. In our case, we used graphite oxide films which had an average thickness of 13.5 μm, so that it is highly opaque in the spectral region 140 -480 nm. The absorption spectrum below 140 nm cannot be measured due to the technical

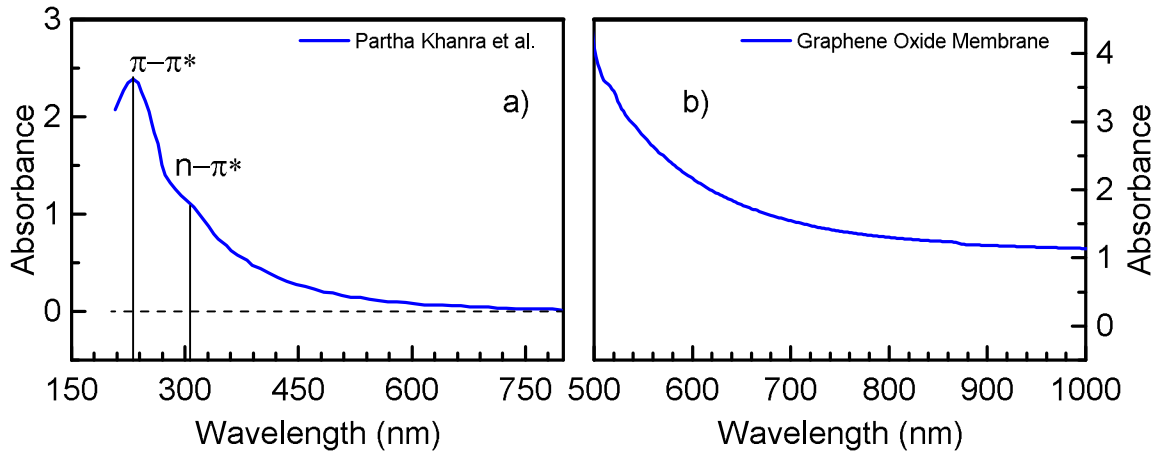

Figure 4.5: Optical absorption spectrum of a) a graphene oxide dispersion in water (3 mg/ml) adapted from Partha et al. [151] and b) a 13 μm thick graphene oxide membrane.

limitations of the UV-Visible-NIR spectrometer.

Li et al. had reported that the overall intensity of absorption spectrum of graphene oxide increases when exposed to reduction mechanism using hydrazine. With increase in the reaction time of the reduction mechanism the ascension in the strong absorption peak observed which gradually shifts from 230 to 270 nm, which is a clear indication of the formation of new sp^2 carbon regions [152]. However, Becerril et al. have shown that, with increase in the graphene oxide film thickness from 9 nm to 41 nm the transmittance of the graphene oxide film drops from 90 to 20 % [153].

Infrared absorption spectroscopy

Like optical absorption spectroscopy, infrared absorption spectroscopy is one of the important tool to study static absorption of mid-infrared electromagnetic waves by graphite oxide. It is mainly used to assign functional groups. Due to oxidation of graphite various oxygen functionalities are attached to the two dimensional single layer of graphene. The infrared absorption spectrum of graphite oxide membrane has shown in the following figure 4.6 and the assignment of functional groups has given in the table 4.1.

Let's categorize the graphene oxide infrared absorption spectrum into five distinctive part. First, the peak at 1050 cm^{-1} is assigned to the C-O-C stretching mode of the epoxide

group. Secondly, the C-OH group vibrational mode frequency is centered at 1380 cm^{-1}. Thirdly, the peak at 1620 cm^{-1} attributed to the bending vibrations of hydroxyl group from the intercalated water and oxidized carbon atoms. The aromatic C=C stretching peak at 1580 cm^{-1} is suppressed due to strong and broad hydroxyl groups. Fourthly, the ketonic vibration mode of C=O is assigned around 1736 cm^{-1}. Lastly, the broad peak centered around 3470 cm^{-1} is assigned to the symmetric and antisymmetric vibrational mode contributions of C-OH, -COOH and H_2O [100]. In addition to the functional group, the electronic contribution over a wide infrared spectral range exist due to graphene-like domains in graphene oxide [59, 154].

The understanding of graphene oxide reduction mechanism using infrared absorption spectroscopy provide insights on the systematic removal of oxygen functionalities [100,155] . Mucik et al. has shown that the removal of COOH, -C-OH functional and H_2O resulted into increase of the peak intensity of C=C vibrational band during the reduction of multi-layered graphene oxide using infrared absorption spectroscopy. However, Krishnmoorthy et al. [156] observed that the gradual increase in absorption bands of oxygen functional groups with increase in degree of oxidation of graphene oxide.

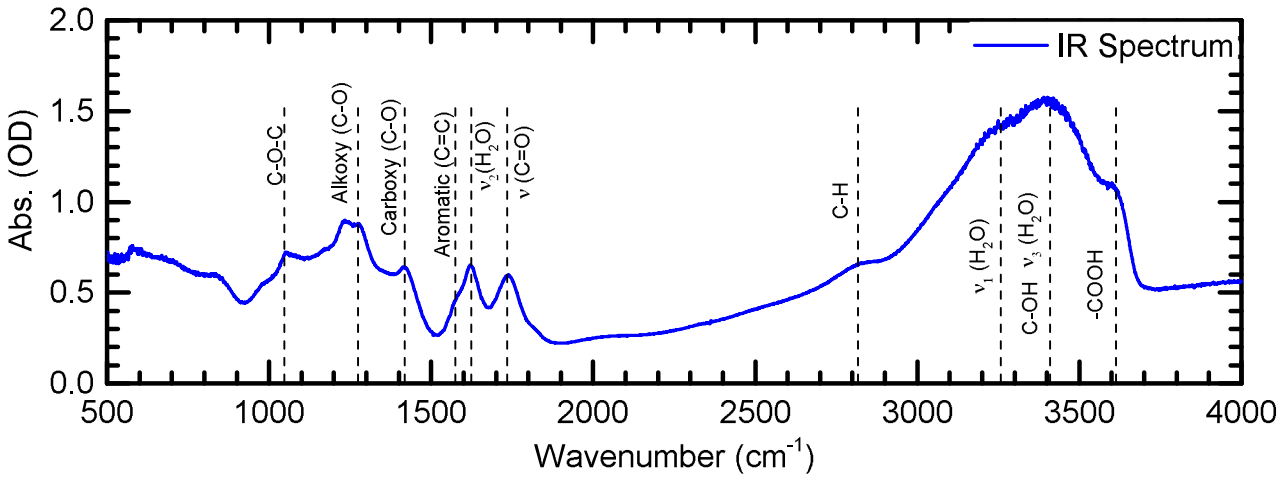

Figure 4.6: Infrared absorption spectrum of graphite oxide membrane.

Functional Group / Mode	Vibrational Mode	Frequency (cm^{-1})
Regions of spectral overlap involving mostly C-O and C=O contributions (850-1500 cm^{-1}) classified into three regions	lactol, peroxide, dioxolate, hydroxyl, C=O contribution, carboxyl and epoxide	900-1100
	C=O contribution, peroxide, ether lactol, anhydride and epoxide	1100-1280
	Ether, epoxide and C=O contribution	1280-1500
IR-active	$^{B}1_{u}$	580
Epoxide (C-O-C)	bend	850
	asymmetric stretch	1230-1320
sp^2 hybridized (C=C)	in plane vibrations	1500-1600
Carboxyl (-COOH)	C-OH vibration	1049 1650-1750 3050-3800
Ketonic species	C=O	1600-1650 1750-1850
Hydroxyl	C-OH with all C-OH vibrations from COOH and water	1070
	bend (water)	1620
	bend + L2 (water)	2048
	asymmetric stretch (water)	3278
	symmetric stretch (water)	3403

Table 4.1: Graphene oxide functional groups from [99, 100].

Femtosecond pump-probe experiment

The femtosecond single color and two color pump-probe measurements were performed using five different pump wavelengths (such as 266 nm, 800 nm, 2000 nm, 2800 nm & 6060 nm) and at the fixed probe spectral windows centered around 1650 cm^{-1} and 3571 cm^{-1} with nearly 250 cm^{-1} spectral bandwidth. The 266 nm laser pulses were generated from a frequency tripler as described in chapter 3. The 800 nm light pulses were used directly from the regenerative amplifier. The 2000 nm pump pulses were used from the idler of one of the two OPAs. The probe pulses centered at 2800 nm and 6060 nm were generated using difference frequency mixing of signal and idler pulses of an OPA in an $AgGaS_2$ crystal. The typical time resolution of the pump-probe instruments was around 150 fs. The graphite oxide sample used for finding zero delay between pump and probe pulses and retrieved approximate time resolution of the experiment. All measurements were carried out by purging the pump-probe set up continuously with dry air to reduce the distortion of mid-infrared probe pulses by water vapor and carbon dioxide absorption lines. The polarization of the 266 nm and 800 nm pump beam was set at magic angle (54.7°) with respect to the probe beam using a half wave plate. The 2000 nm, 2800 nm and 6060 nm pump beam polarization was set parallel to the probe due to the unavailability of half wave plate.

4.6 Humidity effect

Initially, our interest had been to study the intercalated water dynamics in graphite oxide. Here, below in the figure 4.7 results of the humidity effect on graphite oxide measured using static FTIR by purging the sample chamber by dry air are presented. The black curve represents graphite oxide IR absorption spectrum before purging the sample chamber and remaining curves are difference spectrum measured with constant purging of the sample chamber at different hours of time.

The strong peaks at 1622, 1944, 3226, 3382 & 3594 cm^{-1} are observed in the difference spectrum correspond to the water absorption peaks. It clearly indicates the purging of

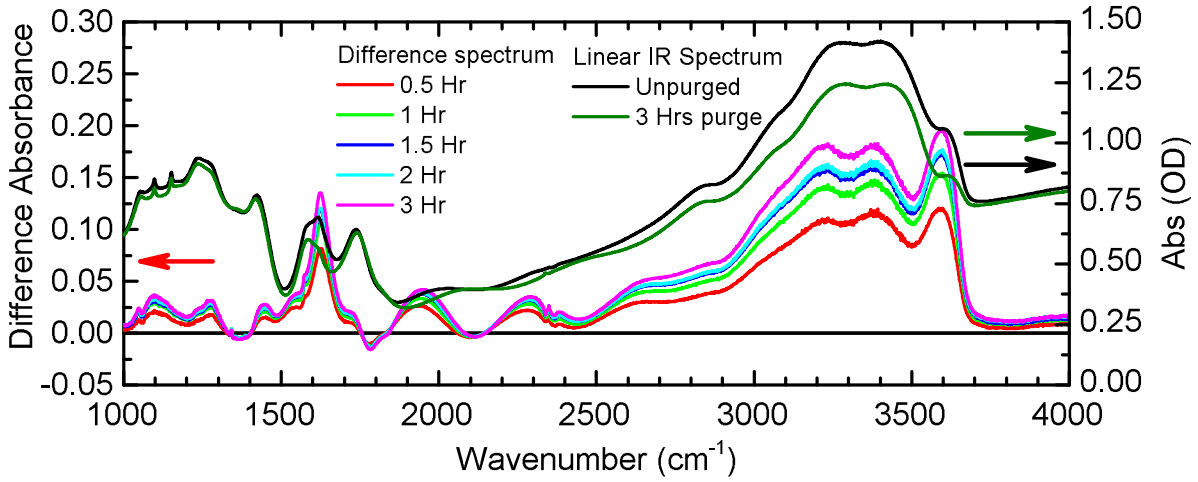

Figure 4.7: Humidity dependent difference absorption infrared spectra of graphene oxide measured at different hours of time. The black curve is linear absorption infrared spectrum of graphite oxide membrane when sample chamber was unpurged. The red, green, blue, cyan and magenta curves are the difference absorption spectra of graphene oxide measured at different hours time.

the graphite oxide film lose water absorbed on the surface. Complete desorption of water molecules in the intercalated layers is debatable as water molecules are strongly confined between the graphite oxide layers [157].

4.7 Graphite-like dynamical behavior of graphite oxide

The wavelength dependent transient absorption measurements were performed using pump-probe set-up to understand the role of C=C stretching and carbonyl (C=O) vibration on the ultrafast dynamics of graphite oxide.

4.7.1 Wavelength dependent transition absorption spectra

The transient absorption changes in graphite oxide were measured using four different pump wavelengths such as 266 nm, 800 nm, 2000 nm and 6060 nm. When 266 nm, 800

nm and 2000 nm were used as a pump, it might excite the system electronically. However, when laser pulses centered at 1650 cm^{-1} (6.06 μm) is used as a pump, it excites resonantly the graphite oxides carbonyl stretch (C=O, 1742 cm^{-1}), water bend (-OH, 1619 cm^{-1}), hydroxyl (-OH) group of graphite oxide and C=C stretching (1573 cm^{-1}) vibrations of aromatic carbon ring along with graphene like regions in the graphite oxide. The graphite oxide comprises the graphene like regions and graphene has electronic absorption tail in the mid-infrared spectral region. The ground-state absorption spectrum of a 2-layered epitaxially grown graphene film has shown in the figure 4.8 along with the theoretically predicted absorption spectrum of single layer graphene [154, 158].

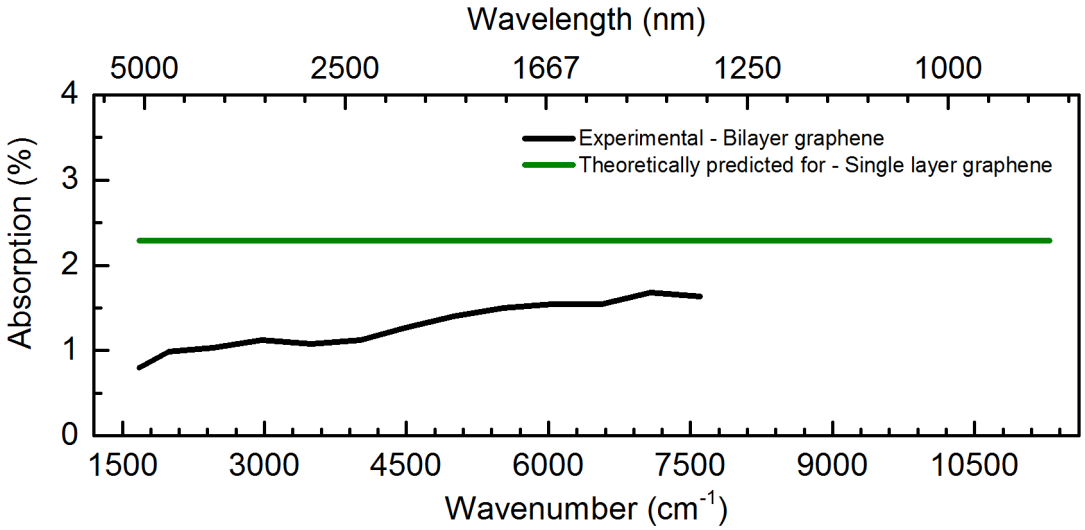

Figure 4.8: The black curve is a ground state absorption spectrum of epitaxially grown two layer graphene adapted from [158]. The green curve is a theoretically predicted one which reveals constant absorption of 2.3 % for single layer graphene adapted from [154].

The band gap varies with shape and size of the material, so we expect for our graphite oxide sample the bandgap could be different at different locations on the film due to the inhomogeneity of its structural composition.

The transient absorption spectra of the graphite oxide measured for four different pump wavelengths at fixed probe spectral window and at different pump-probe delays has been shown in the figure 4.10. For the single color pump-probe measurements, the

scattered pump propagates with probe beam and interferes onto the detector and forms fringe pattern while moving pump beam to create delay between the pump and probe pulses, which is solved by using the phase cycling routine specified in the appendix A. The as measured transient absorption curves are smoothed using Savitzky-Golay filter. The detail information has been provided in the appendix B. In all the transient curves the spectral features are very common. There are two prominent broad spectral features at 1580 cm^{-1} and at 1675 cm^{-1} which are coincident with aromatic C=C stretch and enones C=O stretch vibrations respectively [159]. It is very interesting to note here, in transient spectra we do not observe any peak around 1740 cm^{-1} which corresponds to the in-plane carbonyl (C=O) stretching vibrations in linear infrared spectrum of graphite oxide. However, we have noticed bleach-like peak at 1675 cm^{-1} which is seen in the transient absorption spectra is assigned to the molecular carbonyl group i.e. enone's carbonyl (C=O) stretching vibrations [159]. The enone structure is shown in the following figure:

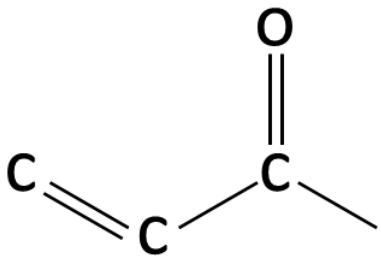

Figure 4.9: Simple enone structure of Methyl vinyl ketone.

It is still unclear why the molecular enones signal is appeared in transient absorption spectrum. The more apparent observation in spectral features is when the pump wavelength changed from 266 nm to 800 nm, the features in the spectral range 1500 cm^{-1} to 1800 cm^{-1} becomes more prominent for early delays. The rest part of the transient curves apart from these features are linearly ascending. The nature of these transient absorption curves are similar for all the pump probe delays, pump wavelengths and pump fluences employed. After 500 ps of pump probe delay the spectral features become faded away.

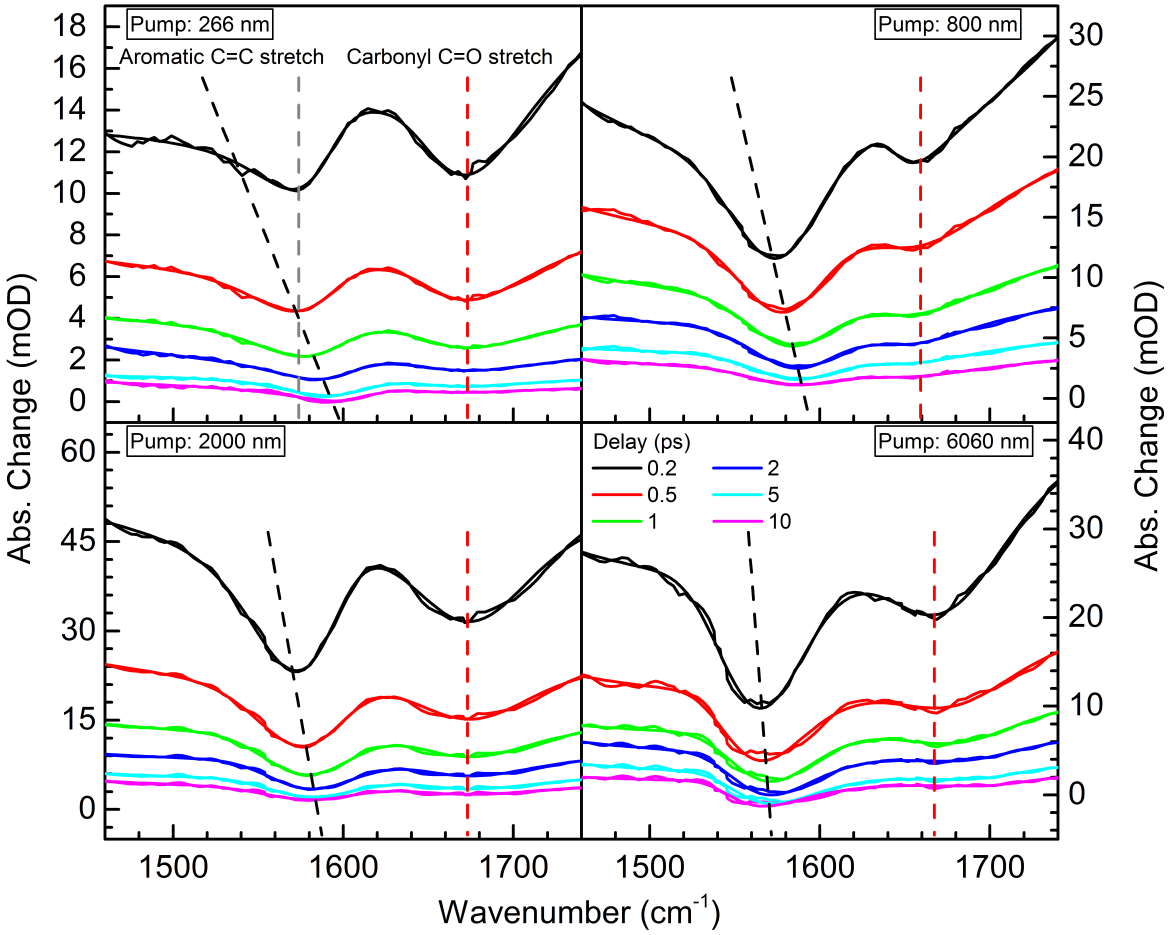

Figure 4.10: Transient absorption spectra of graphite oxide measured with four different pump excitation wavelengths such as 266 nm, 800 nm, 2000 nm and 6060 nm and the sample response measured at the fixed probe spectral window from 1460 cm^{-1} to 1740 cm^{-1}. The six transient absorption curves at 0.2, 0.5, 1, 2, 5, and 10 ps pump-probe delay correspond to the curves in black, red, green, blue, cyan and magenta colors respectively. The pumps 266 nm, 800 nm, 2000 nm and 6060 nm used for pump-probe measurements of fluences were set at 0.7, 3.9, 1.97 and 2.88 mJ/cm^2 respectively.

The *in situ* measured static linear infrared absorption spectrum of graphite oxide in the pump-probe set-up is given below in figure 4.11 for comparison with graphite oxide static linear infrared absorption spectrum measured in the FTIR spectrometer along with one of the transient absorption curve.

The pump-probe set-up was purged very strongly compared to the FTIR sample cham-

ber. The infrared absorption spectrum of graphite oxide measured in *in-situ* position shows a decrease in absorption of the water bending peak at position 1620 cm^{-1} and becomes apparent as a small hump. The appearance of C=C stretching vibrations is becoming more prominent at 1570 cm^{-1}. The transient absorption spectra is difficult to understand as the combination of various functional groups plays major role in the spectral domain from 1500 cm^{-1} to 1800 cm^{-1}.

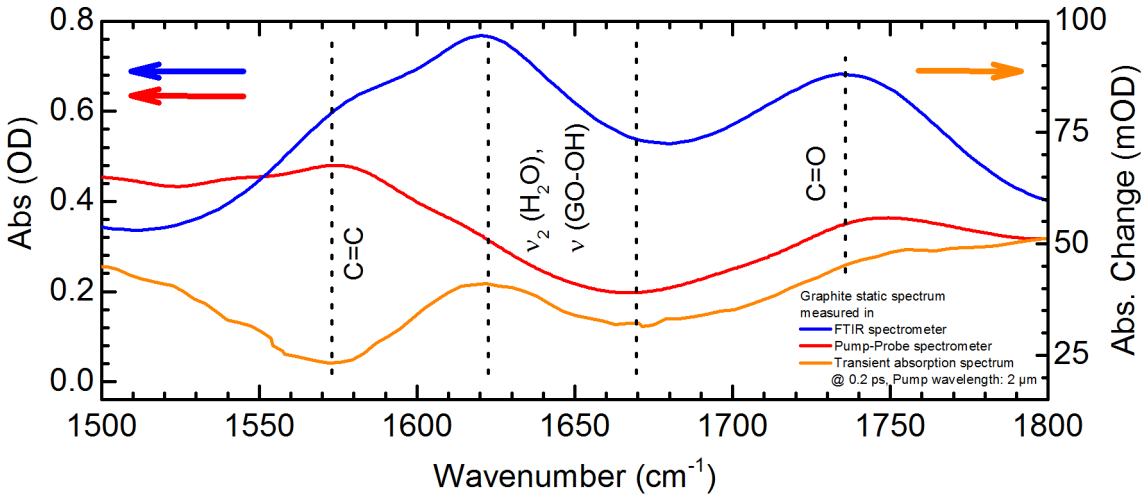

Figure 4.11: Comparison of linear absorption spectra of graphite oxide measured in pump-probe set-up (red curve) and FTIR spectrometer (blue curve). The orange color curve is a transient absorption curve.

The graphite oxide is a three dimensional structure of carbon atoms decorated with oxygen functionalities along with localized graphene like domains. So when we probe or excite the graphene oxide in the spectral domain of 4000 cm^{-1} to 1000 cm^{-1}, we are probing electronic bands and oxygen functional groups simultaneously. This complicates the understanding of the transient absorption spectra measured in the mid-infrared spectral range. There are almost no reports on the ultrafast dynamics of the graphite oxide measured in the mid-infrared spectral region. Most of the studies are focused onto the understanding of the graphene oxide carrier relaxation mechanism using optical pump probe spectroscopy [137, 139]. Mostly, it is a suspension of single layer graphene oxide in water used for ultrafast relaxation dynamics studies. We are probing the spectral domain of the graphite oxide where the vibrational bands of C=C stretch, -OH hydroxyl bend of

intercalated water and graphite oxide and carbonyl stretch C=O overlaps resonantly over a wide spectral range.

To understand the transient absorption, it is imperative to unravel the electronic and vibrational band structure of graphite oxide. From the transient absorption curves we might assign the spectral feature occurrences to the combined effect of C=C stretching, hydroxyl bend of water and graphene oxide along with enones carbonyl (C=O) stretching vibrational absorption bands. The transient absorption is always found positive that is called induced absorption which could be attributed to the carrier absorption due to the existence of sp^3 hybridized carbon atoms. So, in essence the graphite oxide we measured could be an epitome of the combined attribution of electronic and vibrational response to the pump probe signal. The electronic contribution is so strong that it always maintains a positive sign of the pump-probe signal and the contribution of oxygen functionalities and water convolve with it. So, we could interpret transient absorption of graphite oxide with its spectral features as interference between the electronic and vibrational bands. If we attempt to view in the light of the electronic energy level the picture of graphite oxide, the pumps of wavelengths 266 nm, 800 nm and 2000 nm excite carriers from the valence band to trapping states generated between the valence and conduction band due to oxygen functionalities attached to the carbon atoms of graphene layer. As the graphite oxide is an insulator, the band gap is reported to be in the range of 3.1 to 4.1 eV which depends upon the degree of oxidation [101, 160]. Our graphite oxide sample should have band gap between 3.6-4 eV when compared to the data reported by Muge Acik et al. [60] on the basis of C/O ratio vs bandgap. When we excite graphite oxide with a pump of wavelength 266 nm, we are exciting the carriers from the valence band to the conduction band but when we used 800 nm, 2000 nm and 6060 nm as a pump we were exciting carriers from the valence band not to the conduction band but to the lower energy mid-gap trapping states. While, there is an apparent possibility of electronic transitions. There are still no reports to make clear and correct interpretation about the spectral features observed in the 1500 to 1800 cm^{-1} spectral range of transient absorption curve. A detailed theoretical study on ultrafast dynamics of the graphite oxide in the mid-infrared spectral range needs to be carried out. One more study would like to propose here is to measure transient absorption

changes on gradually reduced graphene oxide samples, the reduction of graphene oxide removes oxygen functionalities attached to the carbon [100], hence a systematic study on graphite oxide samples with varying O/C ratio would corroborate which species of the functional groups or maybe intercalated water contribute to the special features appeared in the transient absorption curve. It would help to understand and generate correct pathways of energy transfer between carriers, lattice and vibrational bands of oxygen functionalities.

4.7.2 Line-shape fitting model for transient absorption spectrum of graphite oxide

The transient curves in figure 4.10 were fitted using the following equation:

$$\begin{aligned}\Delta A = y_0 + \frac{1}{2}\cdot k\cdot(\omega-\omega_p)^2 + \frac{A_{C=C}}{w_{C=C}\sqrt{\frac{\pi}{4\ln(2)}}}\cdot\exp\left[\frac{-4\ln(2)(\omega-\omega_{C=C})^2}{w_{C=C}^2}\right] \\ + \frac{A_{C=O}}{w_{C=O}\sqrt{\frac{\pi}{4\ln(2)}}}\cdot\exp\left[\frac{-4\ln(2)(\omega-\omega_{C=O})^2}{w_{C=O}^2}\right]\end{aligned} \tag{4.2}$$

Where, y_0 - is the baseline

ω_p - is the center frequency of the parabola,

ω - is the frequency axis of the transient absorption curve,

k - is the stretching constant of the parabola,

A - is the area of the C=C or C=O band which has asymmetric Gaussian shape,

and w - is the line-width of the C=C or C=O band.

The C=C and C=O bands are best fitted with asymmetric Gaussian function, the symmetric Gaussian function is modified to fit the asymmetric Gaussian bands with a slight modification to the line-widths of C=C and C=O vibration bands as follows [161] :

$$w = \frac{2w_0}{1+\exp[a\cdot(\omega-\omega_C)]} \tag{4.3}$$

where, a is the asymmetry parameter

ω_C - is the peak position of the C=C or C=O band

w_0 - is the FWHM of the C=C or C=O band measured from static infrared spectrum. For C=C stretching band we used $w_0 = 58$ cm^{-1} and for carbonyl $w_0 = 70$ cm^{-1} from the linear infrared absorption spectrum of graphite oxide. It is assumed here the graphite oxide is a semiconductor or insulator material in which line-width of C=C stretching does not change upon excitation by external field [162].

The time dependent parameters of the equation 4.2 were retrieved by fitting the transient absorption curves in the figure 4.10. The time evolution of these time dependent parameters (y_0, $A_{C=C}$ and, $A_{C=O}$ and $\omega_{C=C}$) are presented in the following figures 4.12 and 4.13.

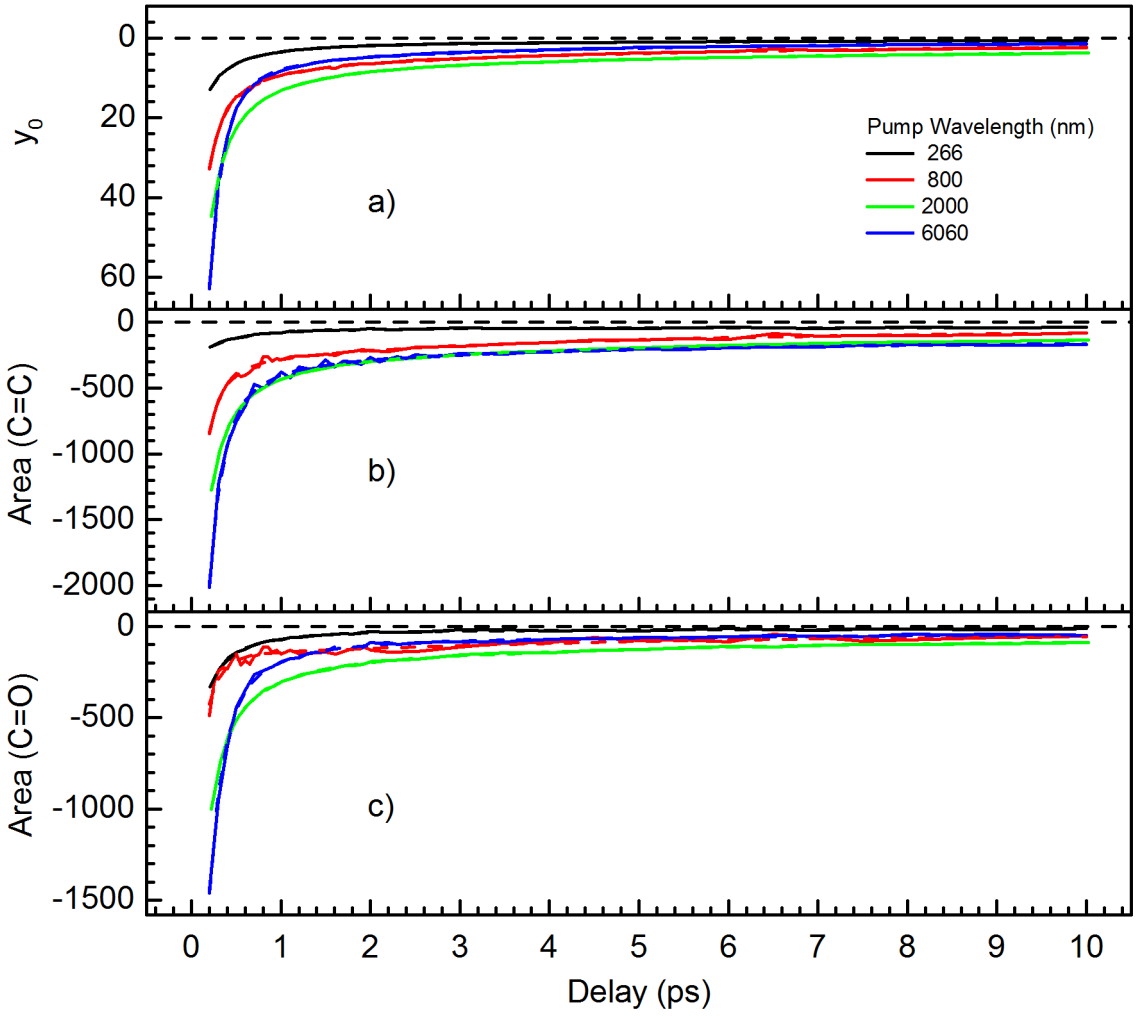

Figure 4.12: The pump-wavelength dependent time evolution of a) baseline (y_0), b) area ($A_{C=C}$) of C=C stretching band, and c) area ($A_{C=O}$) of enones C=O stretching band.

The baseline parameter (y_0) here treated as an electronic background of graphene-like domains as a function of pump-probe delay. Since, we observed only positive change in absorption, the graphene-like regions should be contributing significantly. The parabolic function (k, ω_p parameters of the equation 4.2) support best fitting to the transient absorption curves, though we do not have yet clear understanding of it. The parabolic function should also be in some way connected to the graphene-like response of the signal in the 1500-1750 cm^{-1} spectral region.

The two or three exponential models were fitted to the time-dependent parameters (y_0, $A_{C=C}$, $A_{C=O}$ and $\omega_{C=C}$), which rendered the time constant values as shown in the

tables 4.2 and 4.3. The first, second and third time constant values observed on the times scales of τ_1 = 104-160 fs, τ_2 = 0.31-0.58 ps and τ_3 = 2.41-3.66 ps respectively. The fast time constant τ_1 in graphite materials is assigned to the carrier-phonon scattering, the second and third time constants τ_2 and τ_3 should be assigned to the phonon-phonon scattering [163].

Pump Wavelength (nm)	τ_1 (fs)	τ_2 (ps)
266	170 ± 1	0.84 ± 43
800	140 ± 9	2.47 ± 300
2000	220 ± 4	1.90 ± 62
6060	173 ± 4	1.51 ± 108

Table 4.2: Time constants retrieved by global fitting of two exponential model onto the time dependent components $A_{C=C}$ and $A_{C=O}$ of the line shape fitting parameter.

Pump (nm)	τ_1 (fs)	τ_2 (ps)	τ_3 (ps)
266	160 ± 14	0.58 ± 0.007	3.60 ± 0.89
800	106 ± 21	0.375 ± 0.090	3.03 ± 0.64
2000	158 ± 3	0.56 ± 0.029	3.33 ± 0.19
6060	104 ± 6	0.314 ± 0.030	2.41 ± 0.21

Table 4.3: Three time constants retrieved by fitting three exponential model onto the time dependent baseline component (y_0) of the line shape fitting parameter.

4.7.3 Blue-shift in C=C stretching vibration

We observed, the time-dependent frequency blue-shift for C=C stretching vibration as shown in the following figure 4.13. The frequency shift takes place at different time scales for the excitation wavelengths used. We see the fastest time constants for the pump wavelengths 800 nm and 2000 nm are almost similar (table 4.4). However, for the pumps

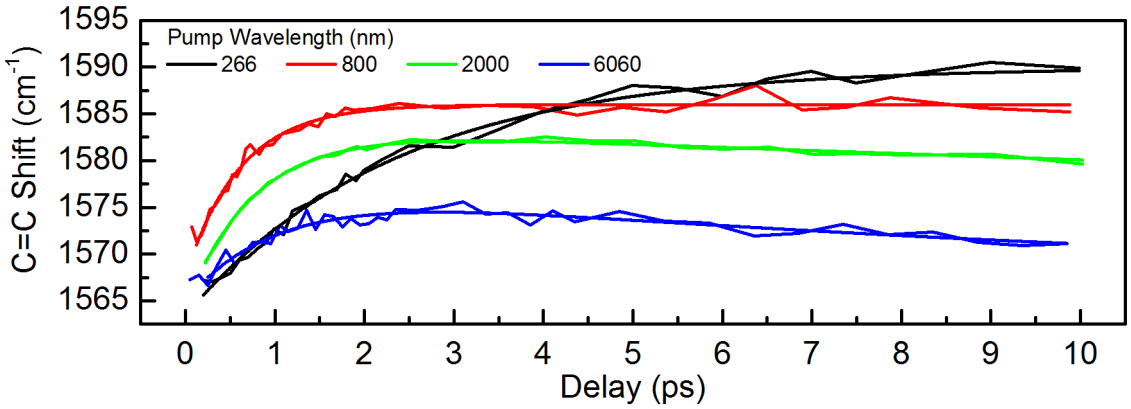

Figure 4.13: The pump-wavelength dependent time evolution in the peak positions of a C=C stretching vibration for the four different pump wavelengths.

266 nm and 6060 nm the fastest time constant becomes slower (table 4.4). These time constants can be related to the excitation wavelength as the 266 nm pump can do carriers to pump into the conduction band then carier-phonon coupling mechanism could be slowed down due to the mid-gap states generated due the oxygen functionalities attached to the graphene structure. From figure 4.10, observed the enones (C=O) vibration frequency does not shift. The average 15 cm^{-1} blue-shift in peak position of $\omega_{C=C}$ is observed.

Pump Wavelength (nm)	τ_1 (ps)	τ_2 (ps)
266	2.44 ± 0.119	–
800	0.66 ± 0.390	–
2000	0.68 ± 0.038	10 (intractable)
6060	1.35 ± 0.640	6.7 ± 108 (intractable)

Table 4.4: Time constants retrieved by fitting mono and bi-exponential models onto the time dependent center frequency $\omega_{C=C}$ of the C=C stretching vibrational band.

The absolute values of blue-shift in the C=C stretching vibration for the pump wavelengths used are tabled as follows:

Pump Wavelength (nm)	C=C Blue-shift (cm^{-1})
266	23
800	15
2000	11
6060	3

Table 4.5: Pump wavelength and C=C frequency blue-shift.

The common observation here is that the C=C stretching gets stronger with lower pump wavelengths used for the graphene oxide excitation. It clearly implies the optical phonons associated with C=C stretching (also know G-mode phonon or zone centered phonons) are strongly coupled over longer pump-probe delays. It cools in few picoseconds (lifetimes are given in the table 4.4). These optical phonons are responsible for coupled electronic excitations. The pump wavelength dependent increased blueshift illustrates the C=C stretching stiffens which implies a high electronic temperature and decrease in

electron-phonon coupling which results into renormalization of C=C vibration frequency /G-phonon energy [162–164].

4.7.4 Time resolved traces

The femtosecond time resolved pump-probe kinetic traces selected for the particular frequencies of C=C stretching, -OH bending and enones carbonyl groups are shown in the figure 4.14. We observed the cross phase modulation in the pump-probe signal induced by the strong pump before and during pump probe pulse overlap. Around the center frequency of the pulse spectrum the cross phase modulation is less pronounced but elongates the instantaneous rise time of the graphite oxide response. At the edges of the probe pulse spectrum the influence of cross phase modulation is more prominent.

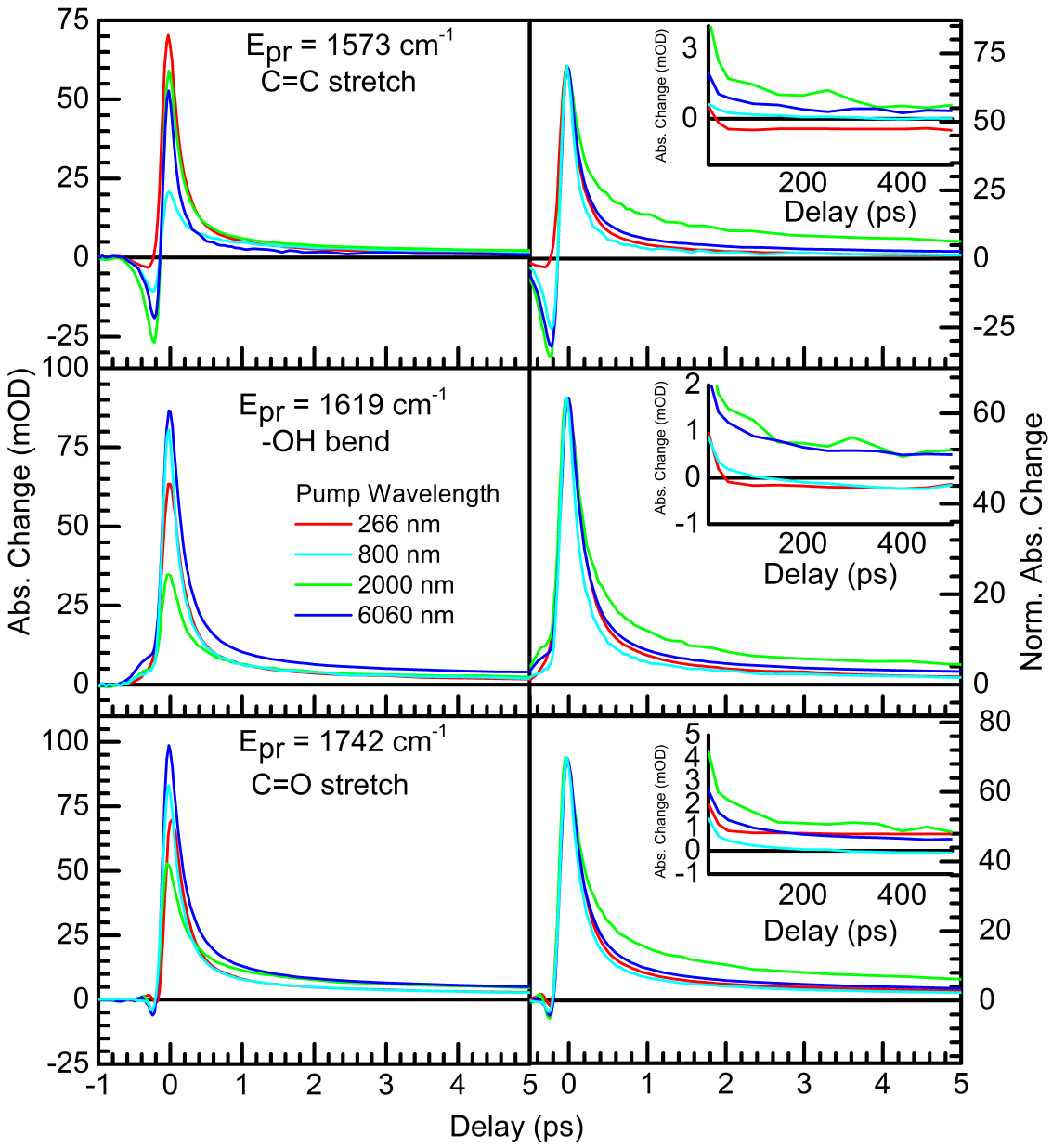

Figure 4.14: Measured kinetic curves of graphite oxide at three different probe frequencies a) 1573 cm^{-1} b) 1619 cm^{-1} c) 1742 cm^{-1} are shown in the left panel. The pump wavelengths 266 nm, 800 nm, 2000 nm and 6060 nm correspond to the red, green, blue and cyan curves respectively. In the table 4.6, the relaxation time constants calculated using sum of four exponential models are given. On the right side of the panel the curves are normalized to the red 266 nm pump curve. In the inset the slow dynamics is zoomed in to get the idea of the decay at longer pump-probe delays. The pumps 266 nm, 800 nm, 2000 nm and 6060 nm used for pump-probe measurements of fluences were set at 0.7, 3.9, 1.97 and 2.88 mJ/cm^2 respectively.

The time resolved pump-probe traces were fitted using the following equation:

$$\Delta A = \frac{1}{2} \cdot \left[1 + \mathrm{erf}\left(\frac{t - t_0}{\sqrt{2} \cdot \sigma}\right)\right] \cdot \left[\sum_{n=1}^{4} A_n \cdot \exp(\frac{-(t - t_0)}{\tau_n}) + C\right] \tag{4.4}$$

Where, ΔA is the change in absorption & erf is the error function,

t_0 is the pump-probe delay offset,

σ is the cross-correlation factor,

A_n is the amplitudes of the exponential function,

τ_n is the time constant,

C is the term which represents intractable amplitude and time constant at longer pump-probe delays.

A sum of four exponential fit well to full range of the pump probe delay. The assignment of these time constant is a complicated task. The processes in graphite oxide should be occurring at different time scales and with different pathways due to the defect induced states by oxygen functionalities [69].

	τ_1 (fs)		
Pump (nm)	1572 (cm^{-1})	1618 (cm^{-1})	1741 (cm^{-1})
266	136 ± 22	156 ± 16	159
800	129 ± 14	156 ± 14	165
2000	135 ± 10	150 ± 7	161
6060	109 ± 24	123 ± 13	137 ± 33
	τ_2 (ps)		
266	1 ± 0.58	1 ± 0.35	1*
800	1*	1*	1*
2000	1*	1*	1*
6060	1 ± 0.53	1 ± 0.33	1 ± 0.46
	τ_3 (ps)		
266	13.58 ± 100900	12.66 ± 68.8	15.11 ± 12.34
800	9.4 ± 4.3	9.9 ± 8.8	7.58 ± 3.52
2000	17.67 ± 43	23.53 ± 44	14.17 ± 14.26
6060	21 ± 238	27.44 ± 105300	15.38 ± 61.79
	τ_4 (ps)		
266	13.31 ± 2043000	33.96 ± 33.43	5930 ± 8484000
800	203.6 ± 516.7	120.90 ± 314.85	106.1 ± 157.6
2000	159.7 ± 1694.5	235.3 ± 2418.3	146.7 ± 428.4
6060	150.1 ± 2566.41	27.72 ± 437800	89.21 ± 935.8

Table 4.6: Time constants retrieved by fitting the model equation 4.4 on the time pump-probe curves in the figure 4.19. * indicates fixed parameters.

The fast time constant in our measurements vary with the probe frequency in the time range of 100-165 fs for all pump wavelengths used in the measurement. Breusing et al. has reported the Fermi-Dirac distribution of electrons occurring on 250 fs time scale in single layer graphene due to carrier-carrier scattering and phonon induced intra-band processes [72]. From C/O ratio of our graphite oxide sample, it can be expected the bandgap could be around 4 eV. So when the graphite oxide excited by the pump of wavelength 266 nm, we certainly excite the carriers to the conduction band. However, relaxation of the carriers could be occurring via multiple pathways. The oxygen functionalities and surface of graphite oxide introduces multiple trapping states between the valence and conduction band [69]. Hence, creates different pathways for carrier relaxation into the valence band. The existence of trapping states was studied by using fluorescence study on graphene oxide [165]. At other pump wavelengths, we are exciting the electrons below the band gap in the trapping states. Where the first time constant should be assigned to the scattering of carriers into the available bands [166]. The second time constant we determined was in the range of 1 ps time scale. It could be assigned to the carrier phonon scattering in graphene [22, 78, 167, 168]. Shang et al. reported hot optical phonon relaxation by optical-acoustic phonon scattering in 1.2 ps in CVD grown graphene [165]. The slowest time constants τ_3 & τ_4 are spanning from few tens of picoseconds to nanosecond could be attributed to the slowest excited states rather than trapped states by [136,165]. The phonon cooling creates electron-hole pairs at low energy level which live on longer time scales of few hundred picoseconds to nanosecond [165]. In our case, we are using graphite oxide membrane of 13 μm thickness, manufactured by vacuum filtration method. Therefore, the graphite oxide layers are arranged in a random way in films making it highly inhomogeneous all over its sample length. So, the little change in time constant could be due to the pump probe traces measured at different locations on the graphite oxide membrane are not having similar composition everywhere.

When all curves were scaled to the maximum absorption change of 266 nm pump wavelength kinetic trace, the fast decay for all the curves observed below 500 fs for all the probe frequencies. The trend of the pump-probe signal is the same for all pump and probe frequencies. The long living component exist for all curves which never decay completely

to zero and have slower time scale than 100 ps. A common pattern is observed for all probe frequencies. The absorption signal of 800 nm pump trace decay faster than the other kinetic traces during the initial 10 ps time scale. Afterwards it slows down and decays completely for probe frequencies of 1573 & 1742 cm^{-1}. However at the probe frequency 1619 cm^{-1}, it has a negative absorption after 150 ps. The absorption signal induced by a pump of wavelength 2000 nm decays slower than the rest of the pump induced pump-probe signals. At 1619 cm^{-1} probe frequency, the dynamics of 2000 nm pump induced signal matches with dynamics of the signal induced by a pump of wavelength 6060 nm. For all the probe frequencies, the signals induced by pumps of 266 nm and 6060 nm, the dynamics coincident at 10 ps timescale and afterwards the decay of longer living states is different for each one.

Over all, the major contributions to the pump-probe signal could be interpreted as follows: the fast time constants should be from the carrier-carrier scattering and carrier-phonon coupling. The long living signal is attributed to the existence of low energy electronic state above the valence band and hot phonons which lose energy to carriers and generate electron-hole pairs which decays over several picoseconds time scale.

4.8 Fluence dependent response of C=C and enones carbonyl (C=O) stretching vibrations in graphite oxide

The effect of pump fluence on the C=C stretching and carbonyl (C=O) species of graphite oxide are discussed in this section.

4.8.1 Fluence dependent transient absorption spectra

The excitation dependent transient changes in graphene oxide were studied. The 800 nm pump was used with four fluences such as 3.9, 13.1, 19.6, and 26.2 mJ/cm^2 and a fixed probe spectral window was centered at 1650 cm^{-1} with FWHM of 250 cm^{-1}. The transient absorption spectra were measured at four different pump fluences are presented in the following figure 4.15. The tilted dashed black lines represents the evolution in the C=C stretching frequency which is blue shifted for longer pump-probe delays. The vertical

dashed red lines represents evolution in the enones carbonyl (C=O) stretching vibration band. The important feature observed here is that we see the loss of spectral band which coincident with enones carbonyl stretch spectral position with increase in pump fluence. When line shape function described in the subsection 4.7.2 applied to these curves, we clearly observe on 200 fs timescale the enones carbonyl (C=O) spectral band in transient absorption spectra for the pump fluence 26.2 mJ/cm^2 decays almost completely.

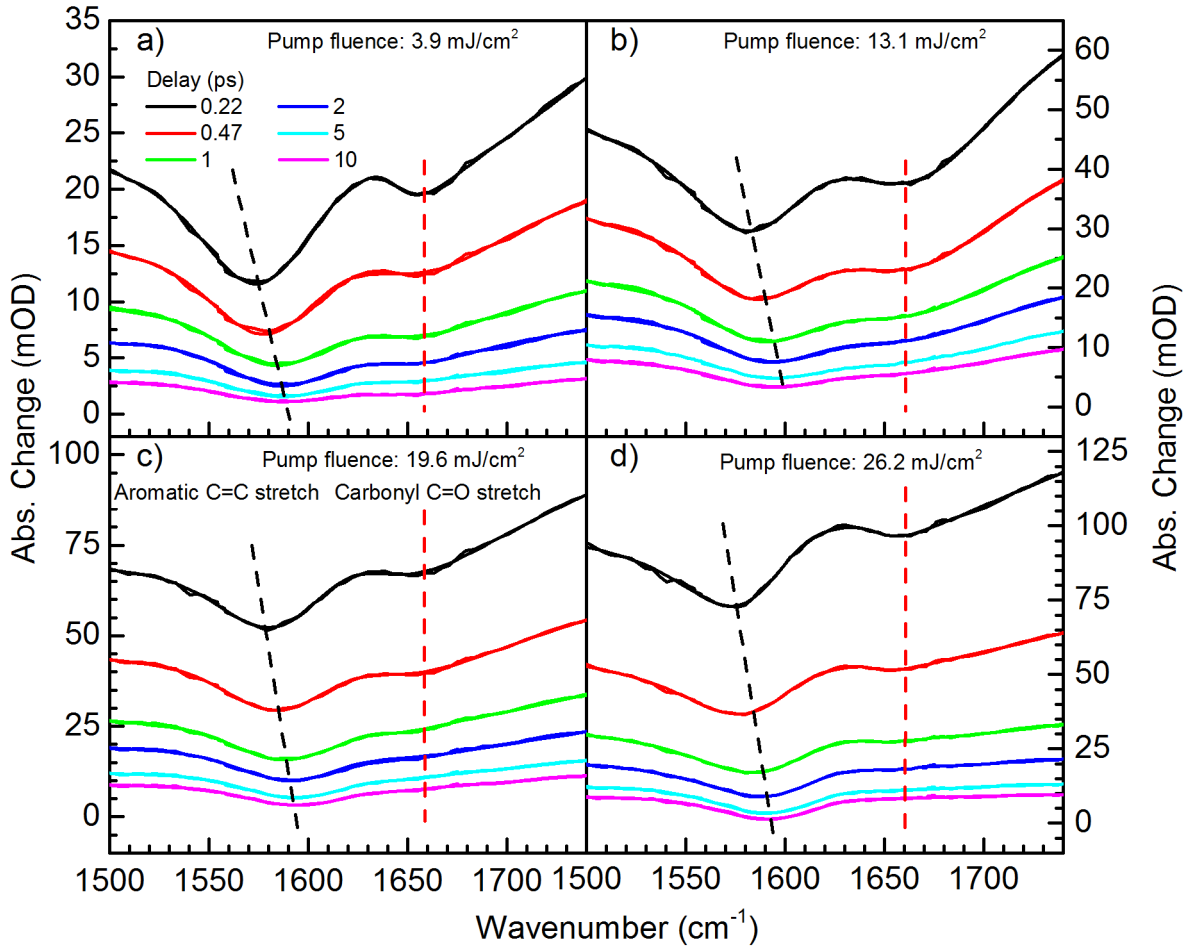

Figure 4.15: Transient absorption spectra of graphite oxide measured with four different pump fluences such as a) 3.9, b) 13.1, c) 19.6, and d) 26.2 mJ/cm^2 and at a fixed probe spectral window. The six transient absorption curves at 0.2, 0.5, 1, 2, 5, and 10 ps pump-probe delay correspond to curves in black, red, green, blue, cyan and magenta colors respectively.

4.8.2 Line shape analysis of transient absorption spectra

The time-dependent parameters (y_0, $A_{(C=C)}$, $A_{(C=O)}$ and ω_{CC} (center frequency of the C=C stretching band) of the line shape function are retrieved from the transient absorption curves (cf. figure 4.15) are plotted in the following figures 4.16 and 4.17.

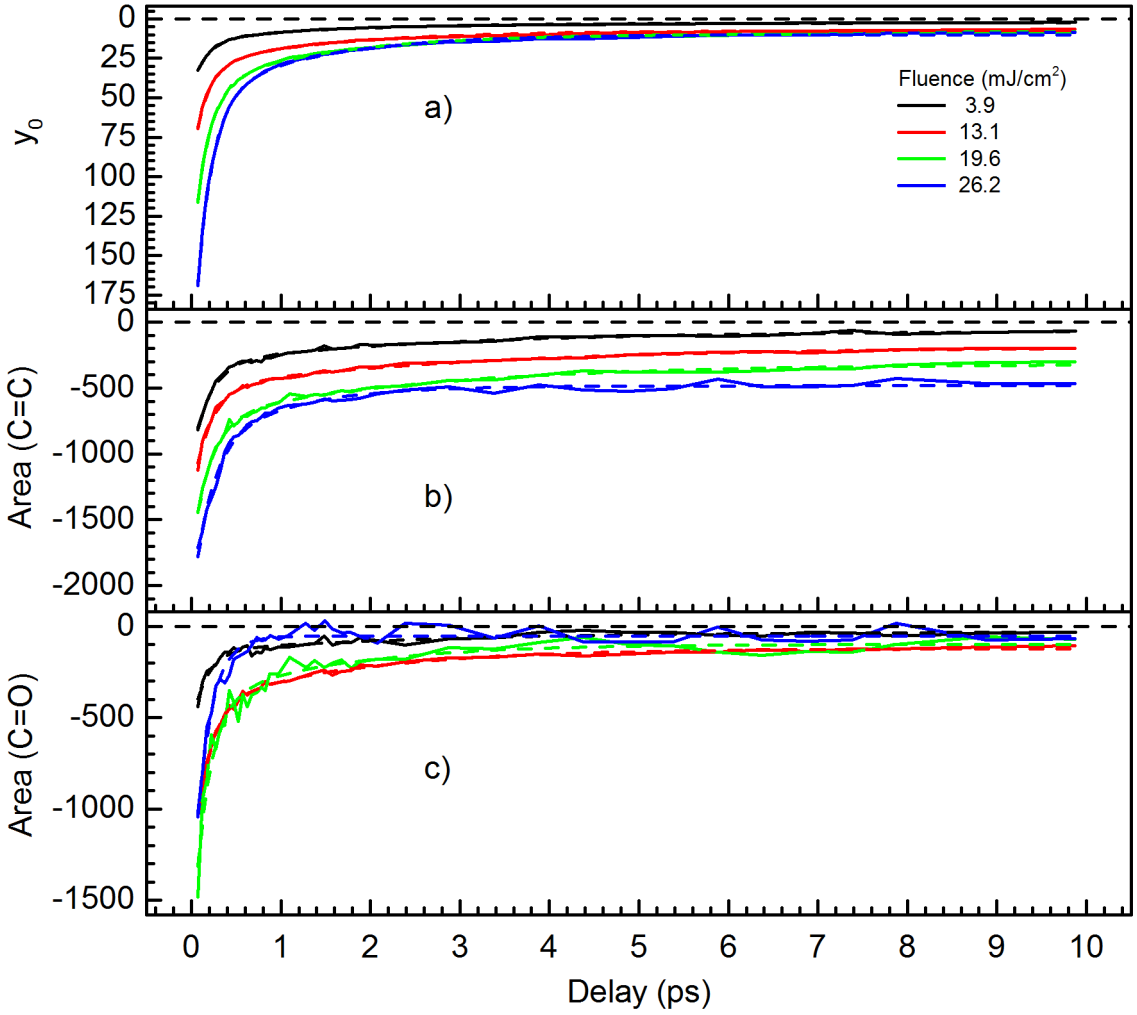

Figure 4.16: The pump-fluence dependent time evolution of a) baseline, (y_0) b) area ($A_{C=C}$) of C=C stretching band, and c) area ($A_{C=O}$) of enones carbonyl (C=O) stretching band. The dashed lines are the fits to the curves.

The modified sum of exponential model used for fitting time dependent fitting parameters retrieved by applying line shape fitting function to the transient absorption spectra at various pump-probe delays.

The modified sum of exponentials model used is as follows:

$$x = y_0 + (A_1 \cdot \exp(-(t - t_0)/\tau_1) + A_2 \cdot \exp(-(t - t_0)/\tau_2) + C) \tag{4.5}$$

where, y_0 is the baseline parameter,

t_0 - is the pump-probe delay offset,

t - is the pump-probe delay,

τ_1 and τ_2 - are the first and second time constants,

C - is the parameter which is intractable component of the curves at longer pump-probe delays.

The sum exponential model applied to retrieve associated time constants of the parameters (baseline (y_0), area ($A_{C=C}$) and area ($A_{C=O}$) (figure 4.16)) of the line shape fitting function applied to the transient absorption curves.

Pump (mJ/cm^2)	τ_1 (ps)	τ_2 (ps)	C
3.9	0.17 ± 0.005	1.55 ± 0.083	2.58 ± 0.097
13.1	0.15 ± 0.005	1.48 ± 0.075	7.46 ± 0.188
19.6	0.16 ± 0.005	1.42 ± 0.077	9.42 ± 0.293
26.2	0.17 ± 0.004	1.21 ± 0.064	10.0 ± 0.3

Table 4.7: The time constants derived by applying modified sum of exponential function to the baseline y_0 parameter of the line shape function applied to the fluence dependent transient absorption curves.

The three exponential model fits well to the baseline (y_0) parameter. The three time constants: first time constant is in the range of 0.15-0.17 ps, second time constant is

in the range of 1.21-1.55 ps and third time constant is in the range of 2.58-10 ps. The important observation here is that the second time constant decreases from 1.55 ps to the 1.21 ps with increasing pump fluence. However, the third constant component increases from the 2.58 ps to the 10 ps with increasing pump fluence. The fast time constant we assign to the carrier-phonon scattering. And second and third time constants to phonon-phonon relaxation might be happening either through two different relaxation pathways or through two branches of phonon modes.

The modified sum of exponential temperature model (as described in equation 4.5) fits very well to the area ($A_{C=C}$) and ($A_{C=O}$) parameters. From the table 4.8, we see the trend of ascension in the first and second time constants of C=C stretching with increase in pump fluence. The third time constant is intractable. But, it can be concluded the third time constant also increase with pump fluence.

Pump (mJ/cm^2)	τ_1 (ps)	τ_2 (ps)	C
3.9	0.16 ± 0.010	2.04 ± 0.22	-76 ± 6.23
13.1	0.15 ± 0.007	2.16 ± 0.17	-206 ± 6.18
19.6	0.20 ± 0.013	2.40 ± 0.307	-319 ± 0.12.1
26.2	0.28 ± 0.02	2.64 ± 1.14	-455 ± 20.98

Table 4.8: The time constants derived by applying sum exponential functions to the area (C=C) parameter of the line shape function applied to the fluence dependent transient absorption curves.

From the table 4.9, which represents the time constants of enones carbonyl (C=O) group. We observed the first time constant increase with fluence but the second time constant vanishes. It is also clear from the transient absorption spectra where we observed with increase in pump-probe delays and with increase in pump fluences decrease in enones carbonyl (C=O) band at 1660 cm^{-1} in transient absorption spectrum.

Pump (mJ/cm^2)	τ_1 (ps)	τ_2 (ps)	C
3.9	0.1 ± 0.015	1.77 ± 0.44	-34 ± 7.31
13.1	0.17 ± 0.009	1.73 ± 0.166	-120 ± 5.32
19.6	0.15*	1.31 ± 0.37	-98 ± 20.6
26.2	0.20 ± 0.012	—-	-42

Table 4.9: The time constants derived by applying sum exponential functions to the area (C=O) parameter of the line shape function applied to the fluence dependent transient absorption curves. * is the fixed parameter.

4.8.3 Blue shift in C=C stretching Vibration

The evolution in the center frequency of C=C stretching vibration of graphite oxide is plotted as a function of pump-probe delays. We have observed the C=C band peak frequency is blue shifted. For all the pump fluence used we observed average 15 cm^{-1} blueshift. The meaning of blueshift of the peak position of the C=C stretching could be the C=C stretching vibration gets stronger. It implies that the stiffening of C=C stretching or G-phonon mode is pump fluence independent but is sensitive or dependent to the pump wavelength used in the pump-probe experiments.

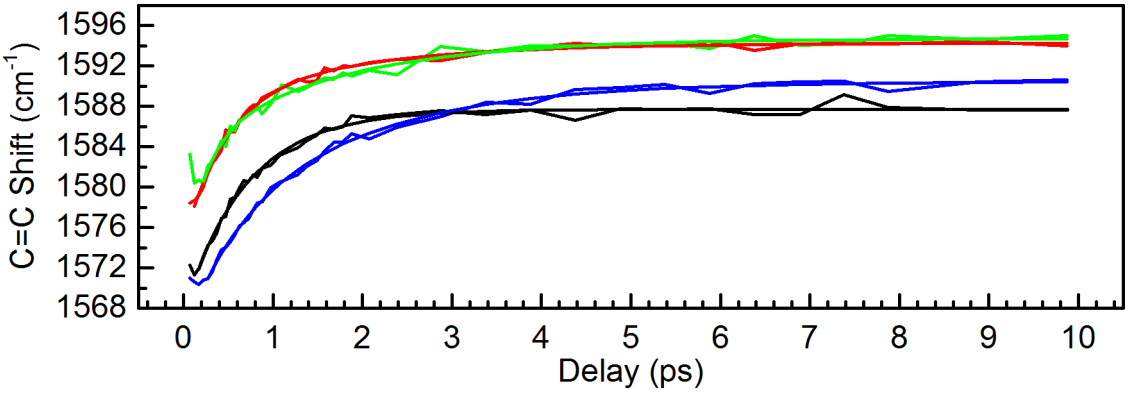

Figure 4.17: The time dependent frequency shift in the peak position of C=C stretching vibration for the pump fluences 3.9, 13.1, 19.6 and 26.2 mJ/cm^2 represented by black, red, green and blue curves respectively.

The mono and bi-exponential models fit well to the pump-probe delay dependent C=C

stretching vibrational frequency. The mono and bi-exponential models fit very well to the curves in the figure 4.17. However, I would like to discuss only mono-exponential time constants with the processes described by Hugen Yan et al. [163]. The mono-exponential time constants could be assigned to the lifetime of the C=C stretching vibrational band. The life-time of the C=C stretching vibration increases with increase in pump fluences (table 4.10). The increase in life times might be implying the the C=C stretching vibrations are getting hot and that may be the reason we see C=C bleach signal at longer pump-probe delays in figure 4.18.

Pump (mJ/cm^2)	τ (ps)
3.9	0.70 ± 0.02
13.1	0.73 ± 0.027
19.6	1.03 ± 0.066
26.2	1.28 ± 0.037

Table 4.10: Life-times of the C=C stretching vibration as a function of pump fluences retrieved by applying mono-exponential model to the curves in the figure 4.17

4.8.4 Transient absorption curves at longer pump-probe delays

At longer pump-probe delays for the pump fluences 3.9, 13.1, 19.6 and 26.2 mJ/cm^2 the bleach signal at C=C stretch vibrations still exist (figure 4.18) but we observed no trace of enones carbonyl (C=O) stretching band existence at 1660 cm^{-1}.

For the highest pump fluence 26.2 mJ/cm^2 used in the pump-probe experiment, we see the C=C stretching bleach signals becomes stronger compared to the rest pump fluences. It has been observed that the C=C stretching band or G-phonon mode becomes red-shifted for all the pump-probe delays shown in the figure 4.18 compared to the rest other transient absorption curves at lower pump fluences. It might be due to the renormalization of phonon energy is sensitive to pump fluence and contributing to the improvement of electron-phonon coupling [162, 164].

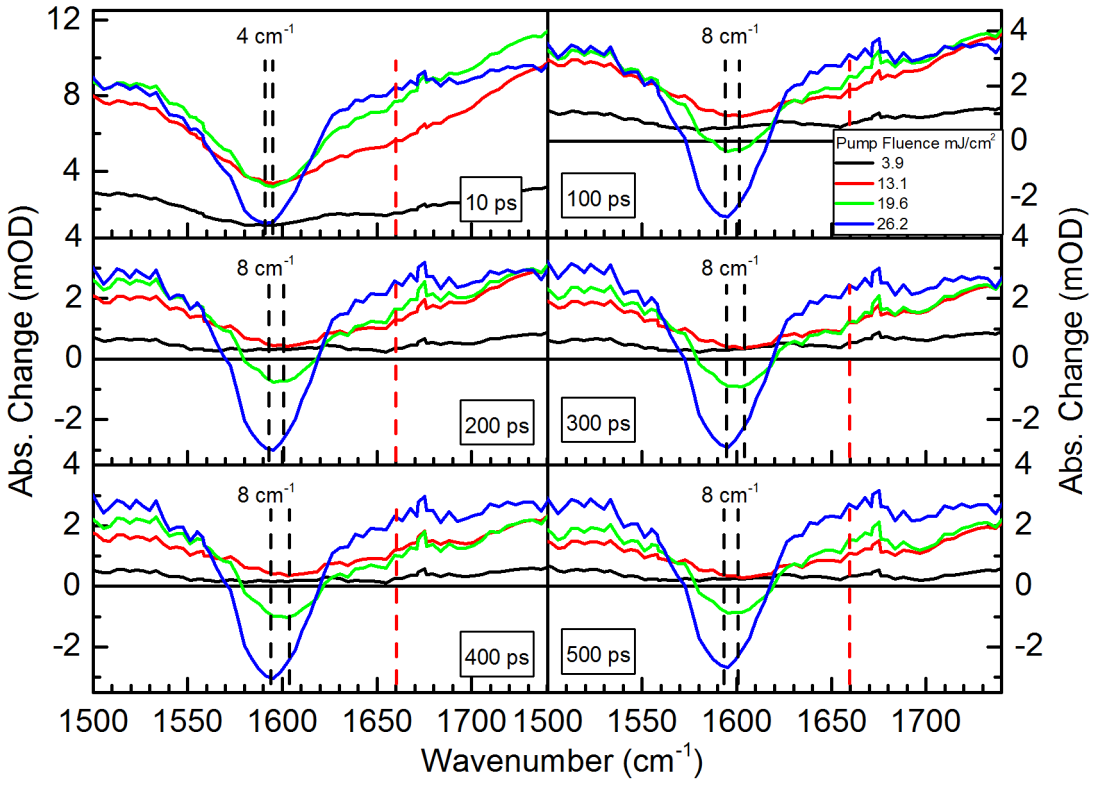

Figure 4.18: The transient absorption curves at longer pump-probe delays at pump fluences 3.9, 13.1, 19.6 and 26.2 mJ/cm^2.

4.8.5 Fluence dependent time resolved spectra

The effect of the pump fluence on the absorption change of graphite oxide is studied. The pump probe traces were measured at four different pump fluences. In the following figure 4.19 a) the measured traces are given and in figure 4.19 b) the kinetic traces are scaled to the highest fluence. We observed that with the increase in pump fluence, absorption change increases which is an indication of multiphoton absorption in graphite oxide. In the inset of figure 4.19 a) the pump fluence with maximum absorption change observed at pump-probe overlap is plotted. The parabola fits very well to the curve in the inset. The reason of increase in absorption with corresponding fluence could be due to the presence of mid gap states which allows the carriers transition to higher energy trapping states. In the inset of figure 4.19 b) the kinetics are scaled to the higher fluence kinetic curve. We observed that the initial fast kinetics happens on $<$ 250 fs time scale for all the fluence

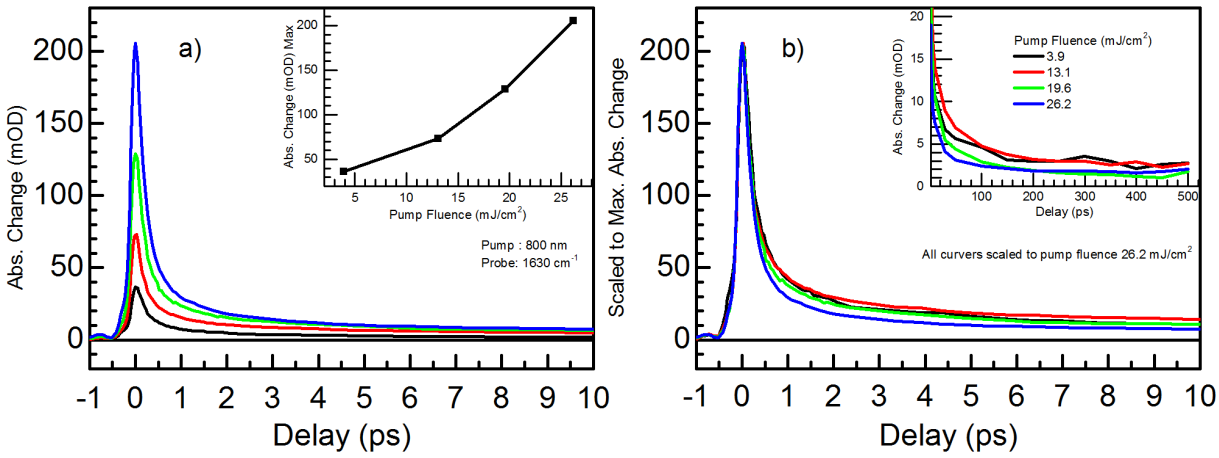

Figure 4.19: Pump fluence dependent kinetic traces. a) kinetic traces measured at four different pump fluences. The inset show pump fluence vs. Max. absorption change observed in each kinetic curve. b) The kinetic curves are scaled to the maximum pump fluence curve. The inset shows the absorption change signal at longer pump-probe delays.

curves. The slow kinetic species decays faster with increase in pump fluence. The multi-photon absorption property of graphite oxide has been used in the fabrication of graphite oxide based semiconductor saturable absorber (SESAM). In the next chapter pump-probe measurement on SESAM are going to be discussed.

4.9 Ultrafast intercalated water dynamics in graphite oxide

The structural dynamics of water is influenced by restricting its degrees of freedom of motion in nano-confined environments which is ubiquitous in natural and engineered environments [128]. Due to the hydrophilic and hygroscopic nature, the graphite oxide is an ideal system for intercalating water molecules between graphene oxide layers. In section 4.6, linear differential spectra of graphite oxide is presented with conclusion that with the purging of the graphite oxide environment with dry air, we observe desorption of water molecules. However, there are some reports which claimed the complete loss of intercalated water molecules in graphene oxide is debatable [157]. We have performed single and two-color pump-probe spectroscopy on graphite oxide membrane in heavily purged environment of experimental set-up at probe beam centered at 1650 cm^{-1} with FWHM of 250 cm^{-1} (section 4.7.1). There we almost loss water bending vibration peak when measured graphite oxide linear infrared absorption spectrum in pump-probe set-up. But however, the OH stretching region suggests that intercalated water is not lost from layered GO.

In this section, preliminary results of single color pump-probe experiment performed on the graphite oxide at 2.8 μm wavelength are presented. The transient absorption change measured as a function of pump-probe delays is shown in the following figure 4.20. In transient absorption spectrum, we observed broad band signal with some features coinciding with symmetric and asymmetric stretching vibrations of water molecules and carboxylic group. However, there is also a possibility of overlap of intercalated water and graphite oxide's hydroxyl group in the same spectral domain. In figure 4.20 b)-d) we see the spectral band of carboxylic group (-COOH) flattens in 500 fs and recovers in 1 ps. Similarly, for asymmetric stretching vibrations of water (maybe intercalated) flattens in 500 fs but unlike carboxylic group it losses its spectral shape. We are still working on these pump-probe results of graphite oxide. The pump-probe time traces at the probe frequencies 3276, 3489, 3628 and 3659 cm^{-1} are shown in the following figure 4.20. The frequencies 3276, 3489 and 3628 cm^{-1} correspond to the symmetric, asymmetric vibration of OH stretch and carboxylic functional group respectively.

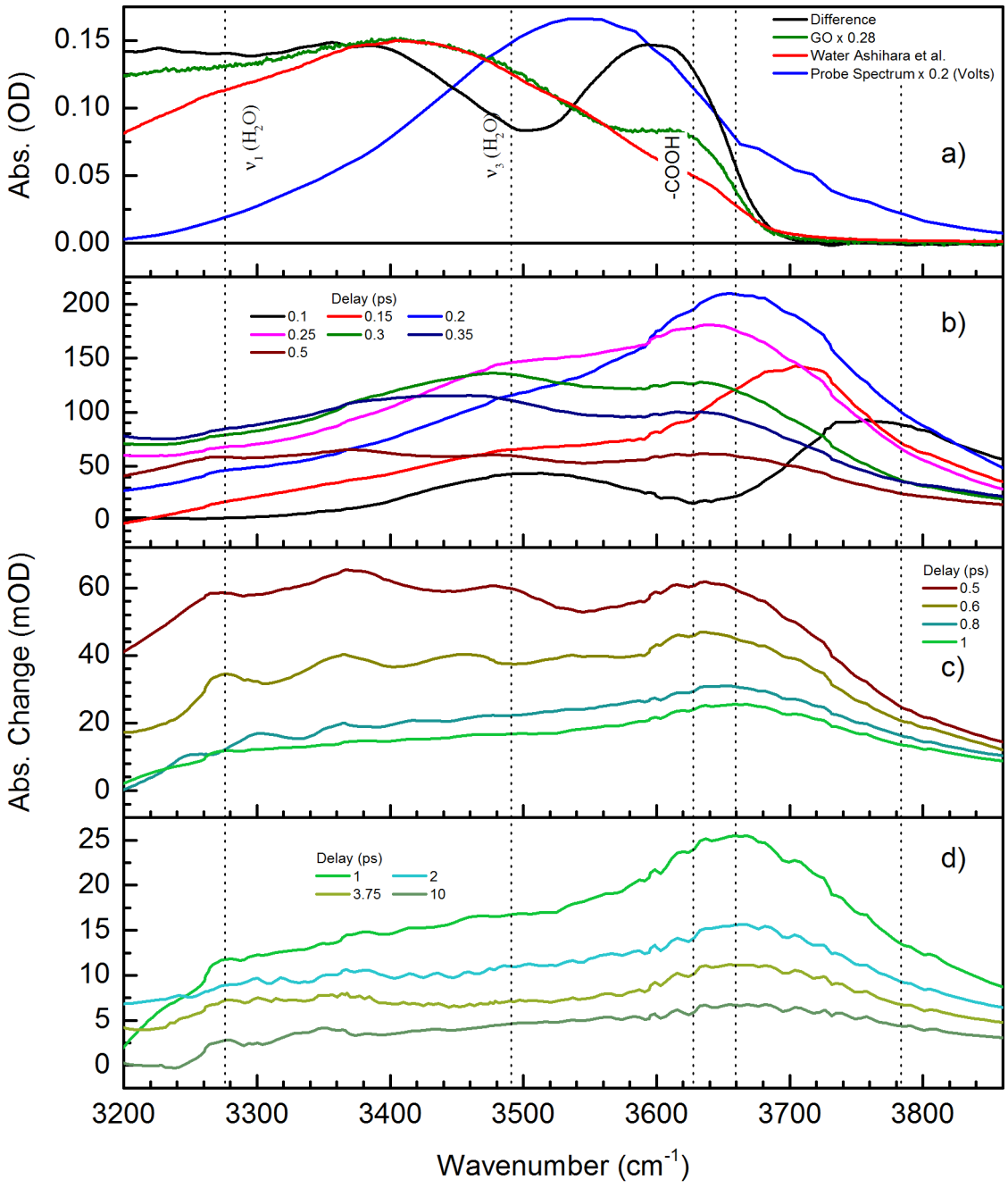

Figure 4.20: a) Linear infrared spectrum of graphite oxide membrane (green curve). The difference between the unpurged and purged graphite oxide linear absorption spectrum has shown in black curve. The red curve represents water spectrum. The blue curve is the probe spectrum. Frequency resolved transient absorption changes in graphite oxide measured using single color pump-probe spectroscopy at 2.8 μm wavelength and at pump-probe delays from b) 0.1-0.5 ps, c) 0.5-1.0 ps, and c) 1-10 ps.

After fitting the equation 4.4 to the pump-probe time traces, we retrieved relaxation time constants as given in the inset of the figure 4.21. We observed that the fast and slow time constants decrease with increase in probe frequency. There could be a possibility that the carboxylic group might be losing energy to symmetric and asymmetric OH stretch vibrations. The Fermi resonance between the OH stretching and overtone of OH bending mode might also be part of this energy relaxation mechanism. There is also a third time constant which exists but is intractable. The OH bending coupling with OH stretching is a planned experiment. The detail understanding of results will be published in coming months.

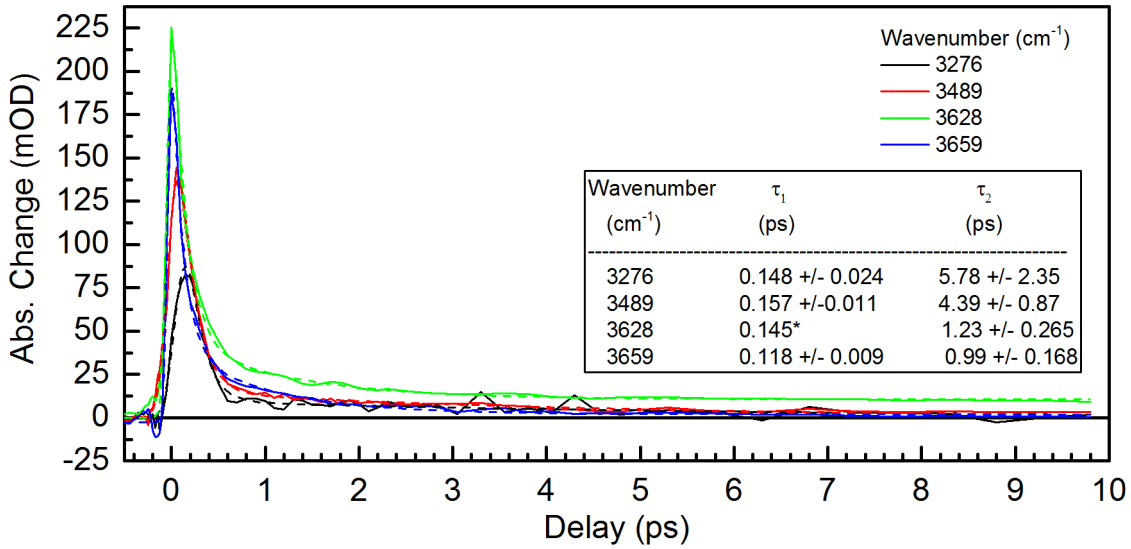

Figure 4.21: Pump-probe time traces measured using single color pump-probe experiment. The pump and probe pulses were centered at 3500 cm^{-1}. The dashed curves are the fits. In the inset the table of the time constants is given. * represents the fixed parameter.

4.10 Conclusions

In this chapter, we used single and two color pump-probe spectroscopy to study ultrafast dynamics of graphite oxide. Frequency resolved transient absorption changes show unique features of carbon C=C stretching vibration at 1573 cm^{-1} and enone's carbonyl (C=O) stretching band at 1660 cm^{-1}. It should be noted that the molecular carbonyl is showing

bleaching-like signal around 1660 cm^{-1} deviating from the carbonyl peak recorded in linear infrared spectrum. It clearly implies the molecular in-plane carbonyl stretching motions are mostly predominant after pump induced excitation. The line-shape analysis of transient absorption curves shows evolution in the center frequency of the in-plane C=C stretching band (also known as G-phonon mode) which should have significant role in the carriers cooling. The pump pulses induce stiffening of in-plane C=C stretching vibration which is directly linked to the increase of the electron temperature which is responsible for the reduction in the electron-phonon coupling in the graphite oxide. We have noted that the stiffening of C=C stretching is pump wavelength dependent and loosely independent of the pump fluences used. In fluence dependent transient absorption spectrum we observed the in-plane enones carbonyl (C=O) stretching vibration vanishes on 200 fs time scale which might be linked to the in-plane C=C stretching vibrations. The pump fluence dependence pump-probe signal corroborates multiphoton absorption process which is useful for nonlinear optical applications. The time resolved pump-probe traces fitted with multi-exponential model provides upto four time constants. The very fast time constant 100-168 fs is attributed to the carrier-phonon scattering. The second time constant on the time scale of 1 ps could be assigned to the optical phonon relaxation. The third and fourth time constants could attributed to the life time of electrons in the the low energy states above the valence band which are generated due to attachment of oxygen functionalities to the carbon.

To unravel the intercalated water dynamics in graphite oxide we have recorded humidity dependent differential absorption and single color pump probe spectra. The differential absorption spectra show loss in water absorption bands implies hydrophilic nature of graphite oxide. In transient absorption spectra, the complicated dynamics showing rapid spectral diffusion to lower frequencies when exciting the OH stretching region which may point to coupling between charge carriers and OH stretching modes of the polar water molecules.

Chapter 5

Carrier dynamics of In-GaAs: A semiconductor saturable absorber mirror

5.1 Introduction

In this chapter, pump-probe results on the relaxation dynamics of charge carriers in semiconductor saturable absorber mirror (SESAM) are presented. Semiconductor saturable absorbers are used for the purpose of mode-locking in laser cavities (figure 5.1) to generate ultrashort laser pulses. The mode-locking of laser pulses is achieved by

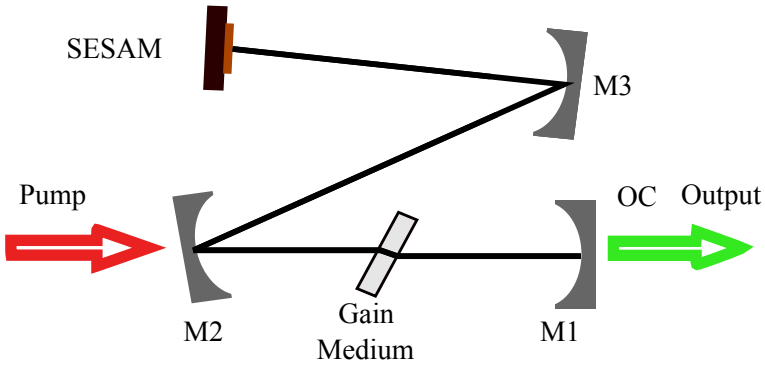

Figure 5.1: Schematic of laser cavity with SESAM as one of the end mirror which acts as a passive device to generate mode-locked laser pulses. M1, M2, and M3 are curve mirrors.

active and passive techniques. The active technique requires an external signal to modulate intra-cavity laser pulses. The active techniques include acousto-optic, electro-optic,

Mach-Zehnder integrated-optic and semiconductor electro-absorption modulators. However, passive mode locking does self modulation of the intra-cavity laser pulses, which makes it more demanding compared to the active techniques due to its ease of incorporation into various laser cavities. The passive mode-locking exploits the property of saturable absorption of a semiconductor material where the absorption of laser pulses decreases with increasing intensity. The first use of semiconductor nonlinearities to passively mode-lock a semiconductor laser had reported by Ippen et al. in 1980 to generate a 5 ps short pulses using heterostructure GaAlAs semiconductor material in an extended resonator [169]. Ten years after, in 1989, Islam et al. used a multiple quantum well saturable absorber structure to generate a 275 fs transform limited pulses from a passively mode locked NaCl solid state color-center laser [170]. Islam, Knox and Keller are considered to be the pioneers of semiconductor saturable absorbers [170–172]. The semiconductor saturable absorber can be made to operate over wide wavelength range by selecting appropriate material composition and band structure engineering.

This chapter has presented the carrier relaxation dynamics of Indium doped gallium arsenide (GaAs) semiconductor material. It was used to generate mode-locked laser output at 2 μm wavelength from the Ho:YLF based gain medium of laser amplifier cavity by our collaborator group of Prof. Franz Kaertner at the Center for Free Electron Laser Science, Hamburg. The carrier dynamics of SESAM measured to compare its suitability for such peculiar laser cavity which is explained by performing degenerate pump-probe spectroscopy at 2 μm wavelength in the result and discussion section.

5.2 SESAM structure

The SESAM mainly consists of three main components, a semiconductor saturable absorber layer, a mirror, and a substrate. The structure of SESAM is illustrated in figure 5.2. The semiconductor absorber layer is embedded in a Bragg mirror structure. The Bragg-mirror is made up of alternating layers of AlAs/GaAs on a semiconductor wafer like GaAs. The semiconductor wafers act as a substrate to hold the SESAM structure and generally are attached to a copper mount to sink the heat generated while used in

for mode-locking the laser cavities. The saturable absorber layer is fabricated from semiconductor material such as InGaAs. Using semiconductor technology, the composition of semiconductor can be easily tailored in order to tune the band gap of the absorber which enables a wide range of absorption wavelengths, renders the advantage to control the absorber parameters such as absorption, saturable fluence, modulation depth, carrier relaxation time, reflection and absorption bandwidth and non-saturation losses. The lasers are developed for different applications having different gain spectrum, differing loss, internal cavity power, etc. So, SESAM are designed according to the need of the laser cavities for mode-locking application. Typically, SESAM can be constructed with two types of structures such as resonant and anti-resonant. In resonant structure, the antinode of the standing wave inside the laser cavity overlaps at the front surface of the SESAM structure. It causes high field enhancement inside the device, resulting in low saturation fluence. However, on the contrary, in anti resonant structure the standing wave has a node at the front surface of the SESAM structure.

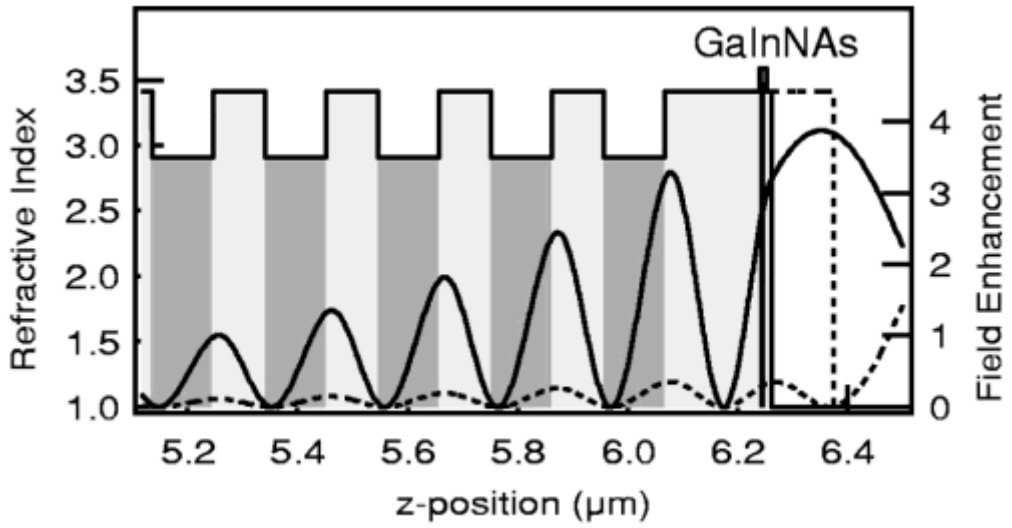

Figure 5.2: SESAM structure. The Bragg-mirror is formed of alternating layers of GaAs(grey)/AlAs(dark) material. The resonant and anti-resonant SESAM structure has been shown using solid and dashed lines respectively. The GaInAs absorber layer is represented by a vertical black line in SESAM structure. The figure is adapted from the Liverini et al. [173].

Our collaborator group had procured SESAM from Batop GmbH and its structure has been shown in the figure 5.3. This structure is quite unusual in the construction of SESAM. The dielectric mirror is deposited onto the heat sink over which the absorber layer is deposited and then GaAs wafer has been added onto it. This SESAM had been used for mode-locking of Ho:YLF laser amplifier cavity to generate stable 2 μm wavelength laser pulses by our collaborator group. However, it was an unsuccessful experiment, the stable mode-locked laser pulses from the cavity could not achieved. To understand this dilemma, the idea of measuring carrier relaxation time constants sparked to compare it with pulse duration of the intra-cavity laser pulses to find out feasibility of this particular SESAM for application into the Ho:YLF laser cavity.

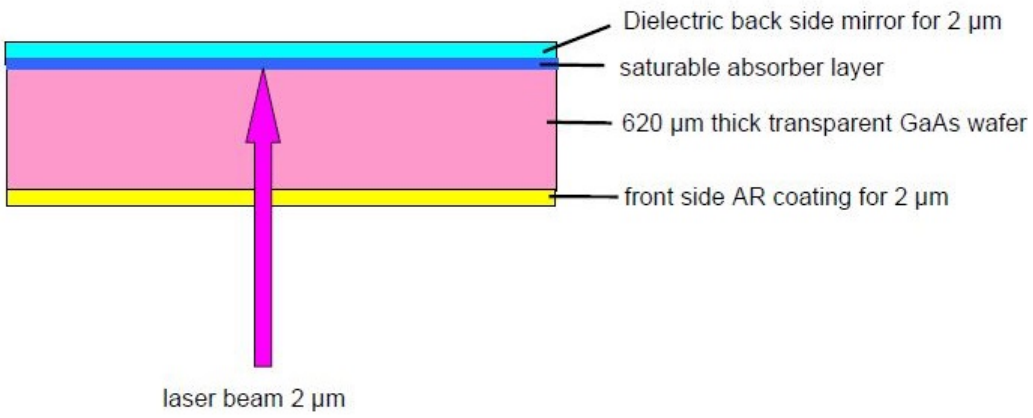

Figure 5.3: The structure of SESAM procured from Batop GmbH.

5.3 Working principle of SESAM

The SESAM absorbs low intensity light and allows to pass only high intensity light with little loss due to transition of carriers into the conduction band. When a high fluence light pulse interact with semiconductor absorption layer, the low intensity part of the pulses generate depletion in the ground state absorption. The high intensity part of the pulse pass through the saturable layer and reflect back from the mirror with little loss. As a result of which the pulse duration gets shortened due to absorption of weak intensity

part of pulses. At low pulse fluences, the absorption of pulse reduces possible Q-switched mode-loking. In figure 5.4 the typical relaxation dynamics of the carriers into the excited states is explained in cartoons [174].

The carrier dynamics of the SESAM is measured using the pump-probe spectroscopy. The carriers are excited to the conduction band using a high fluence pump and the relaxation of carriers is monitored using weak probe pulse as a function of a change in delay between them. The carriers that are excited into the conduction band generally relax with two different time constants. The fast time constant is usually on the time scale of 60-300 fs and slow time constants on the time scale of a few picoseconds to nanoseconds. The fast time constants correspond to the thermalization due to Fermi-Dirac distribution of carriers in conduction band and starts partial recovery of the absorption. The longer time constants correspond to recombination of carriers from the conduction band or mid gap trapping states with the holes in the valence band. The fast time constants allow effective shaping of subpicosecond pulses whereas the reduced saturation intensity on long time constant scale allows self starting of mode locking.

5.4 Experimental

SESAM details

The SESAM sample procured from Batop GmbH had the following specifications:

- Laser wavelength: $\lambda = 2000$ nm
- High reflection band (R > 96 %): $\lambda = 1700$ .. 2150 nm
- Absorbance: $A_0 = 2$ %
- Modulation depth: $\Delta R = 1.2$ %
- Non-saturable loss: $A_{ns} = 0.8$ %
- Saturation fluence: $\Phi_{sat} = 70$ μJ/cm^2

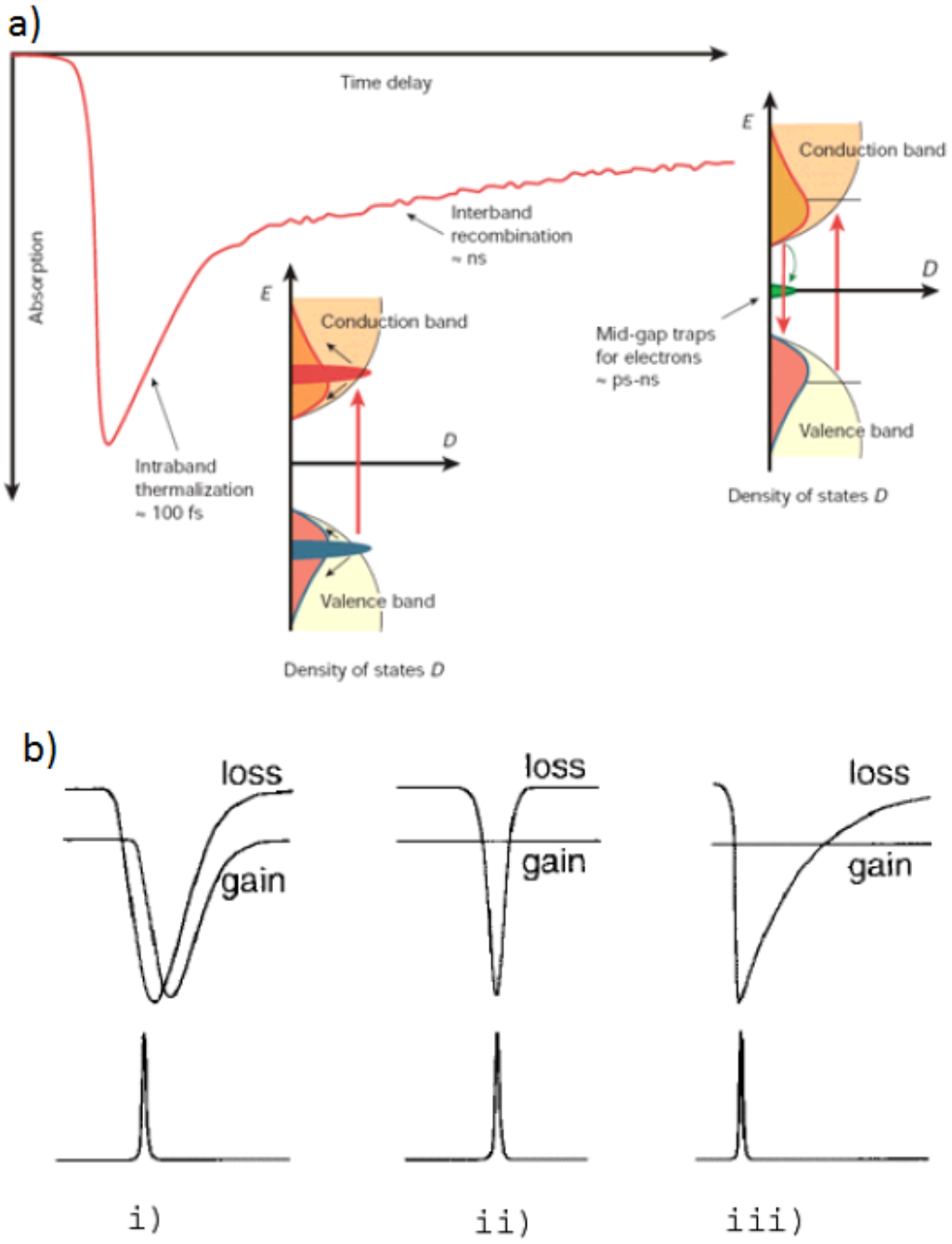

Figure 5.4: a) Relaxation dynamics of SESAM measured using the pump probe spectroscopy. The pictorial representation of carrier evolution after excitation has been shown in cartoons adapted from [174]. b) Mode locking models with dynamic gain saturation using i) passive mode-locking with a slow saturable absorber ii) mode-locking with fast saturable absorber, and iii) soliton mode-locking adapted from [175]

- Relaxation time constant: $\tau \sim 10$ ps
- Damage threshold: $\Phi = 4$ mJ/cm^2
- Chip area: 4mm x 4mm; chip thickness 625 μm
- Design: laser beam goes through the AR coated GaAs substrate

The linear reflectance spectrum of the SESAM has shown in the figure 5.5. It has a broad spectral reflection in the wavelength range from 1700 to 2150 nm, higher than 96% practically suitable for 2 μm laser cavity end mirror application to generate ultrashort pulses. The semiconductor material GaAs (Galium Arsenide) is used for the saturable absorption layer embedded in the Bragg mirror. However, pristine GaAs is not a suitable material for 2 μm laser application. So, the band gap of GaAs was engineered by doping In (indium) atoms/ions. The band gap can be tuned from 1.45 eV to 0.36 eV by changing the dopant concentration 'x' of indium in $In_xGa_{1-x}As$ alloy. At room temperature the band gap as a function of x concentration of indium in $In_xGa_{1-x}As$ had been calculated using the following equation 5.1 [176]:

$$E_g(x) = 1.425 - 1.501 \cdot x + 0.436 \cdot x^2 \qquad (eV) \tag{5.1}$$

Where, $E_g(x)$ is the direct band gap

and x is the doping fraction of indium.

For 2 μm laser application the band gap was tuned to 2 μm by doping 0.65 fraction of indium in $In_xGa_{1-x}As$ alloy.

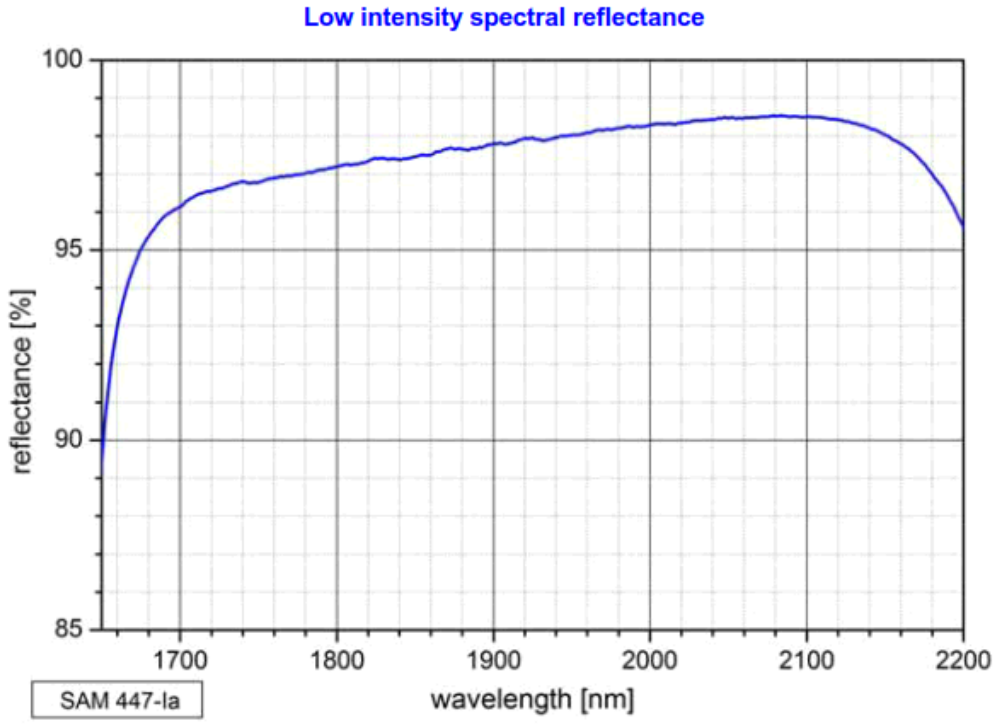

Figure 5.5: Linear intensity reflectance spectrum of the SESAM procured from Batop GmbH for 2 μm laser cavity end mirror application.

Reflective mode pump-probe set-up

The pump-probe schematics has shown in the figure 5.6. We modified our transmission mode pump-probe set up into reflectance mode by changing some optics in the existing setup. The laser pulses at 2 μm wavelength and 100 fs pulse duration at 3 kHz repetition rate were used by tuning the frequency of the idler in OPA. The 2 μm idler pulses were split into pump, probe and reference using a BaF_2 (barium fluoride) window. The BaF_2 window reflects 4% fraction of the main pulse from the front and back surfaces due to the Fresnel reflection mechanism. The beam-sizes of probe and reference were enlarged 1.5 times using 2:3 telescope so when it were focused onto the sample rendered smaller spot sizes than the pump beam spot size. The telescope consist of two spherical mirrors of focal lengths 100 and 150 mm respectively. The high power main pulse transmitted through BaF_2 wedge is used as a pump, which is passed over a sensitive electronically controlled translation stage to create the delay between the pump and probe pulses at the

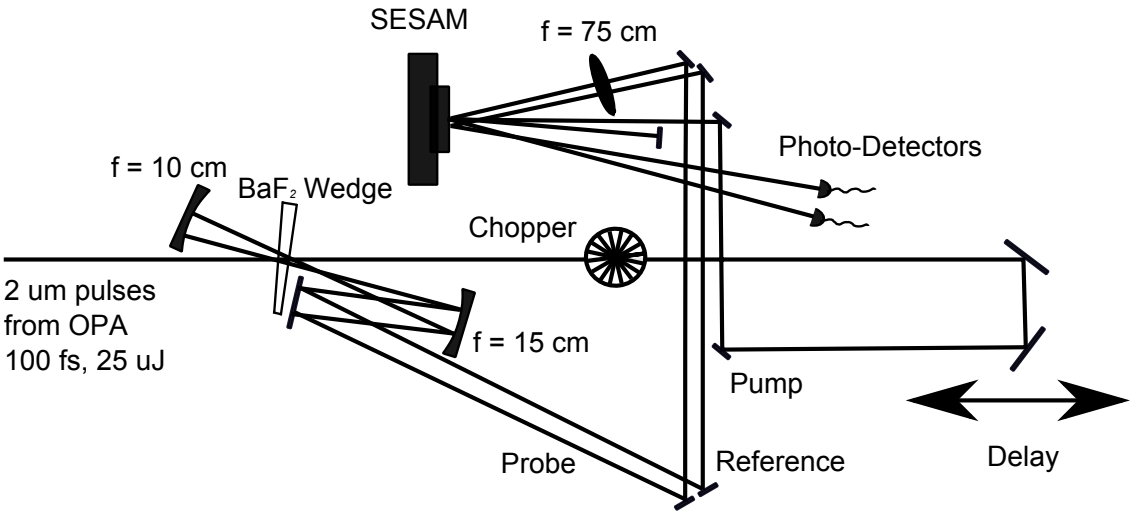

Figure 5.6: Single color pump-probe set-up to measure the differential reflectance changes in SESAM at 2 μm wavelength. The reference beam reflected from a plane mirror which is housed just below the SESAM.

sample position. The pump and probe polarization directions were set parallel to each other. The optical chopper was set such that it was running at half the pulse repetition rate of the regenerative amplifier to modulate the pump beam so it would block every second pump pulse. The probe beam reflected from the SESAM and the reference beam reflected from the plane mirror below the SESAM were detected on slow photo-diodes procured from the Thorlabs GmbH. The differential reflection of probe when the pump is blocked and unblocked were measured using the following equation:

$$\frac{\Delta R}{R_0} = \left(\frac{R}{R_0} - 1\right) \cdot \left(\frac{R_{PumpOFF}}{R_{PumpON}}\right) \tag{5.2}$$

where, ΔR is differential reflectance change

R is probe reflection when pump is On

R_0 is probe reflection when pump is Off

R_{PumpON} is reference reflection when pump is On

$R_{PumpOFF}$ is reference reflection when pump is Off

5.5 Result and discussion

The ultrafast pump-probe measurements of SESAM had performed at varying the pump fluences as shown in the figure 5.7. In general, for all the pump-probe traces, the observed signal decays faster than the instantaneous response of the SESAM sample. The signal for pump fluences below 300 $\mu J/cm^2$ decays in 450 fs and for fluences 350 $\mu J/cm^2$ and 400 $\mu J/cm^2$ decays even faster on 200 fs timescale. For fitting the pump-probe trace following equation 5.3 was used.

$$\begin{aligned}\frac{\Delta R}{R_0} = A_1 \cdot \exp(-(t - t_0)^2/(2 \cdot \tau_1^2)) \\ + A_2 \cdot \exp(-(t - t_0)/\tau_2) \\ + A_3 \cdot \exp(-(t - t_0)/\tau_3)\end{aligned} \tag{5.3}$$

Where, ΔR is differential reflectance of probe

A_1, A_2 and A_3 are the amplitudes

t_0 is time zero between pump and probe pulses

τ_1, τ_2 and τ_3 are the time constants

The first term in the pump-probe trace fitting model is a Gaussian function. As after peak the curve decay faster than initial rise time, the Gaussian function was applied there. The second and third terms are exponential decay functions. However, for fitting the pump-probe trace, we need only one exponential term except for pump-probe trace measured at pump fluence of 50 $\mu J/cm^2$. The average Gaussian width used was an autocorrelation width 50 $\pm$ 5 fs of 2 μm of laser pulse width duration and then the subsequent fast decay observed at 130 fs.

The decay edge of the signal is faster than the instantaneous rise time of the carriers from the valence to the conduction band. It might be due to the property of the semiconductor absorber layer. When pump and probe pulses temporally overlap in absorbing layer, the probe pulse is not affected due to pump pulses which generates carriers. As it starts coming after pump with some delay the lower intensity part of the probe pulse gets absorbed by absorbing layer in the SESAM. So, we could assign this observed asymmetric Gaussian response of the absorbing layer to the absorption property of the semiconducting InGaAs layer. There could be a possibility that the pulse-shape of pump and probe beams

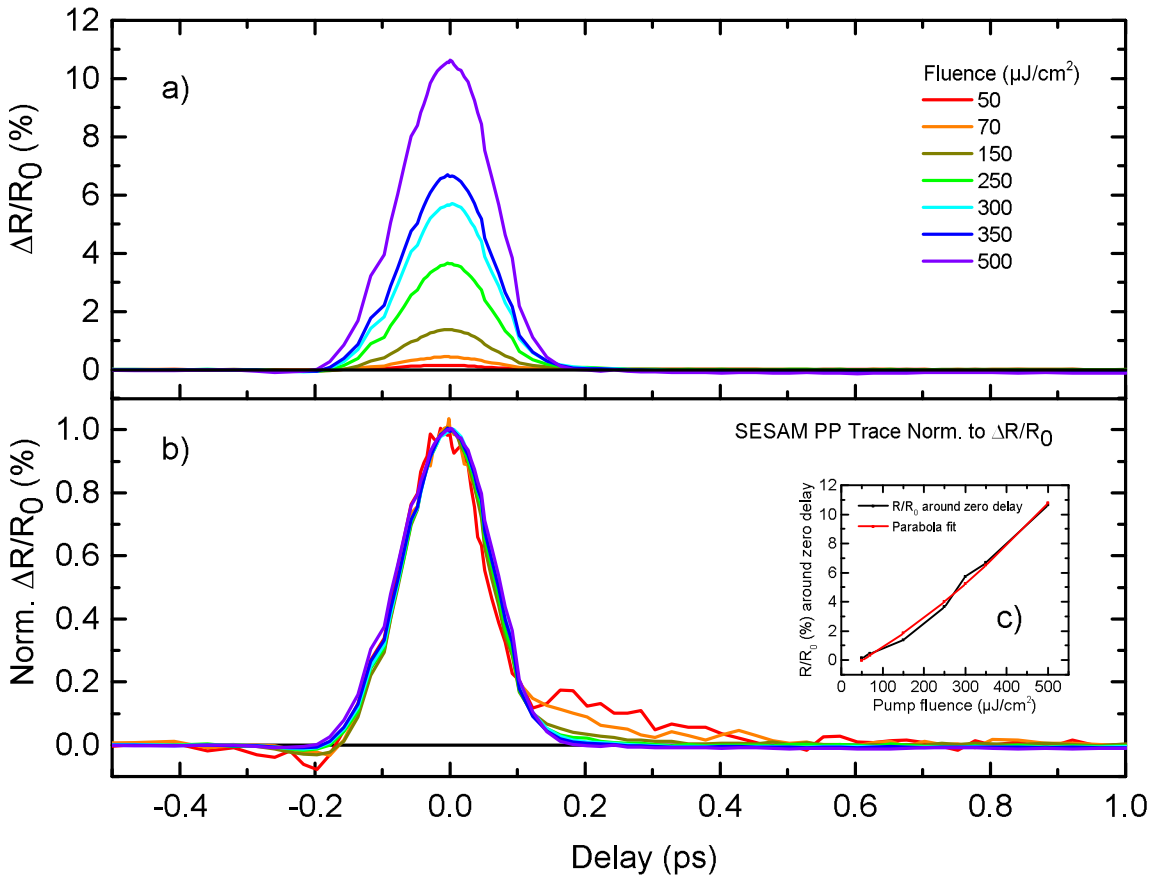

Figure 5.7: Pump-probe time resolved traces measured at six different pump fluences. a) Real measured pump probe traces b) Pump-probe traces normalized to 1. Red, orange, grey, green, cyan, blue and purple color pump-probe traces correspond to the 50, 70, 150, 250, 300, 350 and 500 $\mu J/cm^2$ pump fluences respectively. c) The maximum differential reflection change versus pump fluence around zero delay. The parabola fits reasonably to the curve.

might be asymmetric. It has been reported the pulses interacting with the SESAM gets shorter as a function of intra-cavity pulse fluence [177] which could also be influencing early fast response of the SESAM as evident from the pump probe time traces figure 5.7.

As observed from the pump-probe signal, the decay of the signal contains one time constant term which is so fast. At a such fast time scale carrier thermalization due to Fermi-Dirac distribution was reported [175]. This pump-probe measurement has significant role to understand why the laser cavity of Ho:YLF laser was unstable to mode-lock

intra-cavity laser pulses at 2 µm wavelength. Since, the gain medium Ho:YLF of the amplifier laser cavity has a very narrow gain bandwidth and has non-Lorentzian profile at 2051 nm and 2060 nm as shown in the figure 5.8, the narrow gain bandwidth does not support pulse duration shorter than 500 fs and hence the recovery lifetime of the SESAM has to be more than 500 fs. Hence, we need the SESAM which has a recov-

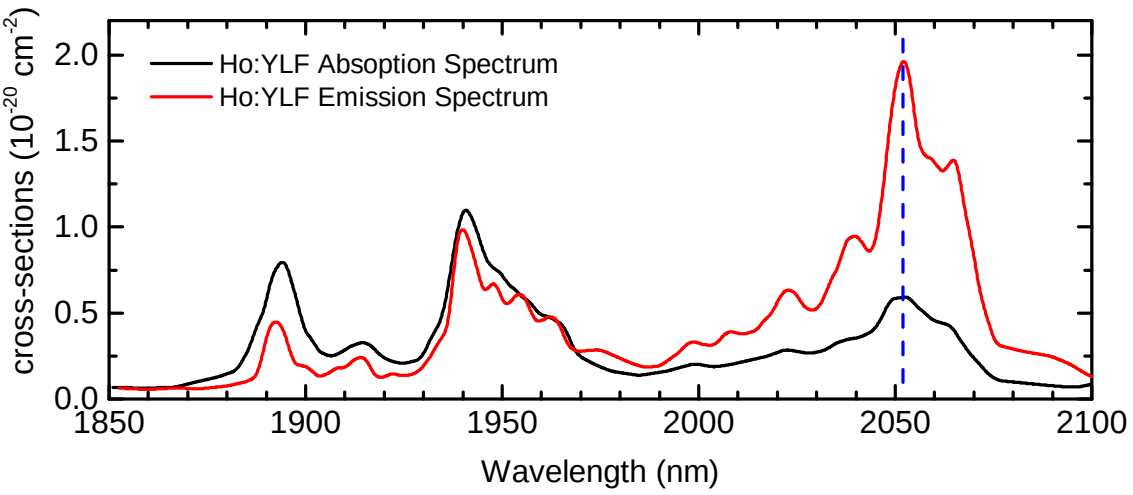

Figure 5.8: Absorption and emission cross sections of Ho:YLF gain medium adapted from [178].

ery time longer than 1 ps which makes the SESAM from Batop GmbH unsuitable for Ho:YLF cavity. Also, the light should be shed upon the structure of the SESAM (cf. figure 5.3). The SESAM structure could be doubtful. The SESAM layer had been grown on Bragg-mirror, which was deposited on the 620 µm thick transparent GaAs wafer with anti-reflection (AR) coating on the top. Usually, the GaAs wafer is used as substrate over which Bragg-mirror, SESAM layer and AR coating is designed respectively. This is one flaw in the SESAM construction for 2 µm wavelength laser. The second flaw need to check the right fraction of In is doped in $In_xGa_{1-x}As$ alloy. However, it was not my concern, I was only entitled to measure the pump-probe dynamics of the SESAM to determine the carrier relaxation life time to help our collaborator to understand this peculiar SESAM is suitable for the Ho:YLF laser cavity to use it as one of the end cavity mirror to generate the stable mode-locked pulses or not.

5.6 Conclusions

In conclusion, we studied the carrier relaxation dynamics of SESAM procured from Batop GmbH. The relaxation time constant of SESAM in excited state were found to be around 130 fs, which entails the SESAM could not support cavity mode-locking due to gain bandwidth of Ho:YLF gain material, which makes it unsuitable to generate mode locked femtosecond pulses at the 2 μm wavelength. The light should also be shed upon the SESAM structure. It could be reconstructed to suit to such particular Ho:YLF laser cavity, which was the another aspect of this study.

Chapter 6

Summary and future perspective

The time-resolved mid-infrared spectroscopy is a powerful technique to explore the ultrafast processes such as chemical exchange, hydrogen bond dynamics, orientational dynamics of molecules, vibrational dynamics of aqueous systems, solvation dynamics, polarization anisotropic effects, electronic processes in materials, liquid interfaces etc. The main objectives of this thesis were to construct the light sources in the mid-infrared spectral region and the time resolved infrared spectrometer to perform ultrafast pump-probe measurements on graphite oxide and semiconductor saturable absorber.

The thesis work had included the construction of non-linear optical set-ups such as the pair of optical parametric amplifiers with subsequent difference frequency stage of capacity to generate tunable mid-infrared light pulses in the spectral region of 1-20 μm, frequency tripler to generate UV light pulses at 266 nm and the time resolved two color reflective optics pump-probe spectrometer. The OPA had two pumping stages to amplify signal and idler. However, its our observation, the OPA efficiency decreases when signal and idler tuned to generate mid-infrared wavelengths above 7 μm, this can be improved by adding a third pumping stage in the OPA to amplify the intensity of signal and idler to get sufficient output power of mid-infrared pulses from the difference frequency stage. Also, the software programs have been developed to control the mechanical delay stages, the monochromator and the data acquisition system. The pump-probe spectrometer had been built in a way to convert it into two dimensional infrared spectrometer in pump-

probe geometry by adding Mach-Zehnder interferometer in pump path in near future. Due to lack of time, the installation of the Mach-Zehnder interferometer had been put on hold and the mid-infrared ultrafast time resolved pump-probe experiments on graphite oxide and semiconductor saturable absorber were carried out.

In the graphite oxide project, our initial interest was to unravel the dynamics of intercalated water molecules between the layers of graphite oxide. The hydrophilic and hygroscopic nature of graphite oxide enables it to absorb water molecules which is quite evident from some studies that reported the interlayer distance between the graphite oxide sheets depends on the degree of humidity in it's surrounding. The static FTIR measurements did show supporting results to this arguments. The difference absorbance FTIR spectra of graphite oxide clearly indicated evolution in the enhancement of water peaks and pronouncement in the appearance of C=C stretching vibration peak at 1573 cm^{-1} which was suppressed by broad absorption of water bending vibration. However, in the pump-probe set-up due to strong purging of the experimental set-up by dry air we see almost complete loss of water bending vibrational band. The single color and two color time resolved transient absorption spectra did show signatures of C=C and enones C=O stretching bands. The understanding of these signatures demands theoretical support to discern the actual mechanism in the signal generation processes. The sum of exponentials was used for fitting time traces. The first two time constants were typically in the range of 100-165 fs and 1-10 ps which are attributed to the carrier-phonon scattering and phonon-phonon scattering respectively. The third and fourth time constants are assigned to the lifetime of the electrons trapped in the low energy states generated due to attachment of oxygen functionalities to the 2-dimensional layered structure of graphene. The slow time constants could be taken as confirmation to the existence of mid-gap states between the conduction and valence band of graphene oxide. The graphite oxide sample used in the experiment had an average thickness of 13 μm, the signal response has been contributed by many inhomogeneous layers of graphene oxide. The time resolved experiments should be performed in controlled manner on single to multilayer thin films to get comprehensive knowledge of C=C stretching band mechanism in the transient absorption spectrum. Also, we should try out reduced graphene oxide films of different degrees of oxidation/reduction.

This will help to monitor behavior of C=C stretching response with change in the degree of reduction of graphite oxide. The reduction of graphene oxide generates more sp^2 carbon (C=C) / graphene like regions which are directly linked to the C=C stretching.

In the SESAM project, we measured carrier relaxation dynamics of a product procured from 'BATOP GmbH'. It was used in the Ho:YLF based cavity as one of the end mirror to generate mode locked output at 2 µm wavelength. The problem which occurred in mode locking output of the amplifier was studied by measuring relaxation times and it was found to be shorter than the pulse duration of the laser pulse inside the cavity making it unsuitable to generate passively mode locked output at 2 µm using Ho:YLF laser gain medium. This led us to the conclusion that the SESAM should be redesigned by engineering carrier relaxation time constants for such a particular application.

Appendices

Appendix A

Phase Cycling routine

For the single color pump probe measurements, we detected interference pattern on to the detector as a function of pump-probe delay. The figure A.1 a) shows the recorded interference pattern. The obvious reason to form the interference pattern onto the detector while moving pump beam to create a delay between pump and probe pulses is that the pump scattered off from the graphite oxide sample and was propagating collinearly with probe and interfered onto the detector. To remove the fringes and get the smooth pump-probe traces we used a technique called as a phase cycling routine. We have introduced this technique into the data acquisition and processing section of our Labview program. The smoothed pump-probe traces after implementation of the phase cycling routine has shown in the following figure A.1 b). The phase cycling routine is an easy method. We take the center frequency of the pump or probe pulse. Calculate the period of it and divide it by some feasible number n. Its gives the small incremental delay step Δx.

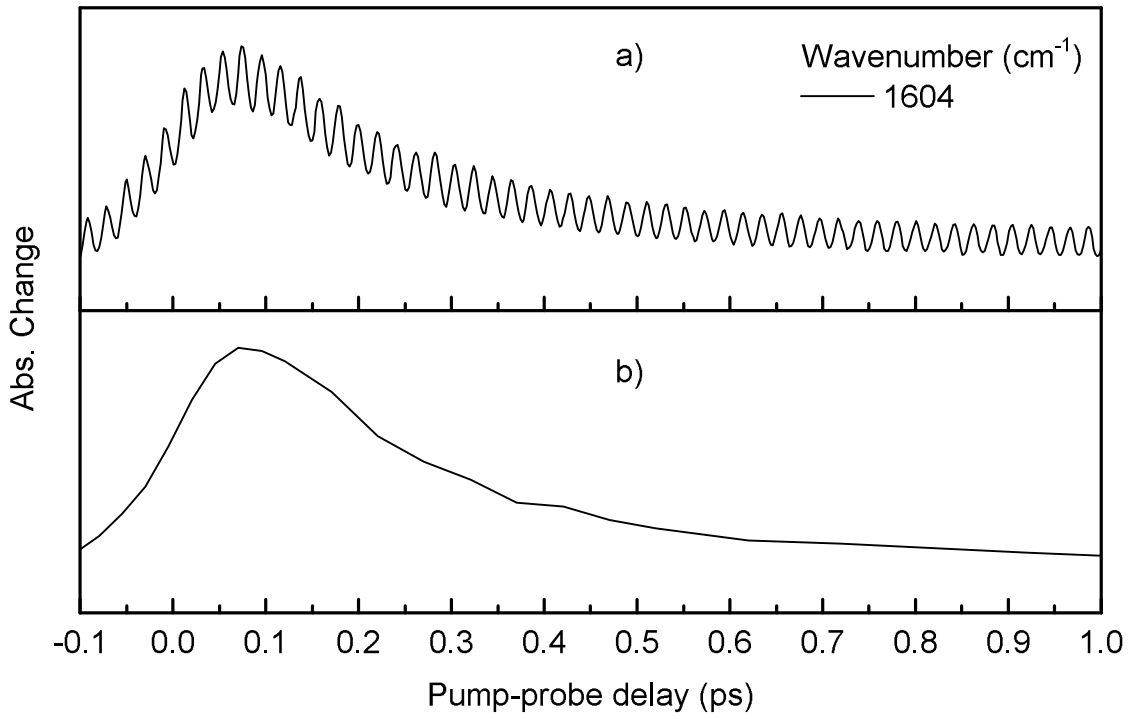

Figure A.1: Single color pump-probe time traces measured at frequency 1604 cm^{-1} a) without phase cycling and b) with phase cycling routine.

Then for each pump-probe delay 'd', we recorded the signal for the delays points as $\left(\mathrm{d} + \sum_{\mathrm{i}=-\mathrm{n}/2}^{\mathrm{n}/2} \mathrm{i} \cdot \Delta\mathrm{x}\right)$. The signal is then averaged by number 'n' we have mentioned it earlier and assigned it to the specified pump-probe delay 'd'.

Appendix B

Smoothing of Transient Absorption Spectra

The infrared detector for infrared light measurement records only 32 spectral components. To measure the full pulse spectrum we move the grating so that all the frequencies in the pulse are scanned across the detector. While measuring the transient absorption spectrum we stitch together 4 chunks of the different spectral pieces. In doing this we observed some spectral chunks are shifted along the y-axis i.e. Absorbance change. To stitch all the spectral chunks together we have developed a Matlab code which is added at the end of this section. The stitching of spectral chunks we call pixel correction. The observed transient absorption spectra had some spikes. Those spikes could be due to the probe beam scattered from the sample and scatter propagates in the direction of probe pulse and forms interference pattern onto the detector. Also the water vapors contribute to the spiky features in the transient absorption spectrum. We smoothed the pixel corrected transient absorption curves using Savitzky-Golay filter. In figure B.1, the comparison between the as measured data, pixel corrected data and data smoothed using Savitzky-Golay filter has been shown.

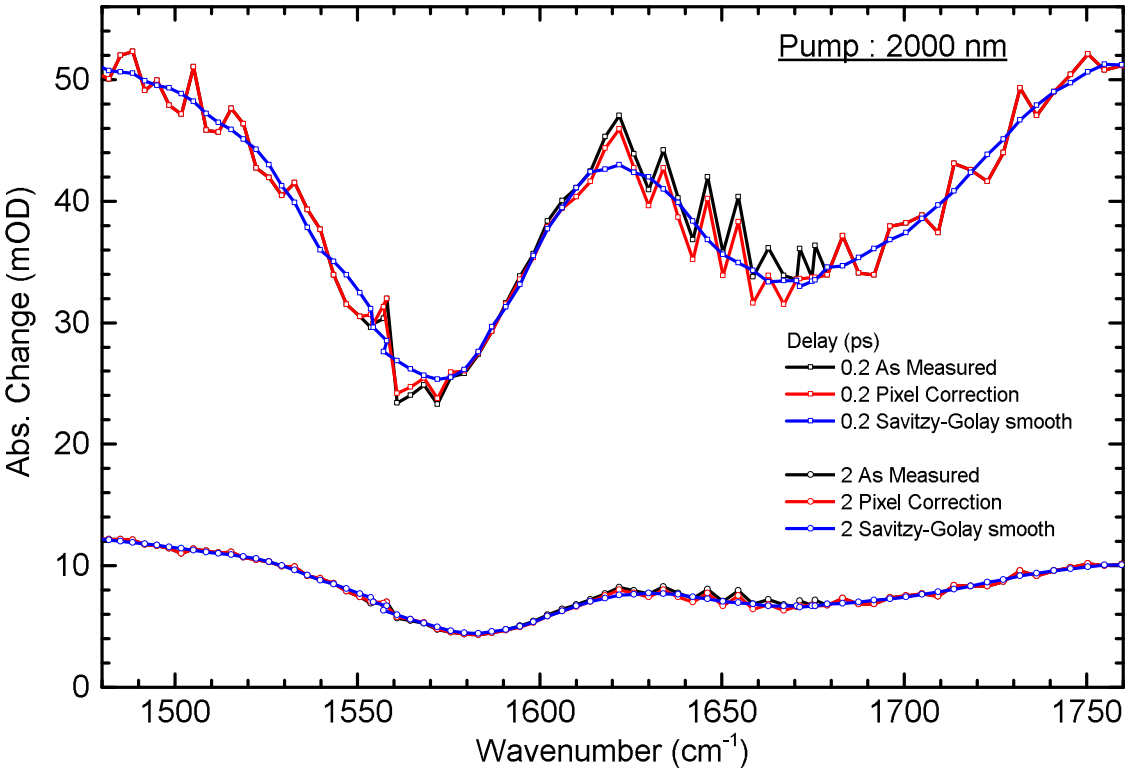

Figure B.1: The comparison between the as measured transient absorption spectrum (black curve), pixel corrected (red curve) transient absorption and pixel corrected transient absorption curves smoothed using Savitzky-Golay filter (blue curve).

Pixel Correction Code

```
% after stepping pixel in PP measurement found shift in signal height
    which need to be corrected

clc;
clear all;
close all;

% load files 1 2 3 4

dr  = 'D:\MPSD\Data\Project\GO Membrane\PP Data\2000 Pump\161117\PP\
    PP-Pump2um\00-03\Bkg corrected\New folder\';    % Directory path
```

```
10 fn  = '00-03';
11 ext = '.dat';
12 filelist = ls([dr,'*.dat']);
13 %Nof = size(filelist(:,1),1);  % # of files
14
15                                                  % columns to be deleted
                                                        % rows to be
                                                    deleted
16 TMP1 = transpose(load([dr,filelist(4,:)])); TMP1(34:121,:) = []; %
       TMP1(:,83:83) = [];
17 TMP2 = transpose(load([dr,filelist(3,:)])); TMP2(34:121,:) = []; %
       TMP2(:,83:83) = [];
18 TMP3 = transpose(load([dr,filelist(2,:)])); TMP3(34:121,:) = []; %
       TMP3(:,83:83) = [];
19 TMP4 = transpose(load([dr,filelist(1,:)])); TMP4(34:121,:) = []; %
       TMP4(:,83:83) = [];
20
21 % Time axis
22
23 Time_ax = TMP1(1,2:size(TMP1,2));
24 LT_ax = size(Time_ax,2);
25 %-----------------------------------------------------------------
26 TMP1(1,:) = []; TMP2(1,:) = []; TMP3(1,:) = []; TMP4(1,:) = [];
27 %-----------------------------------------------------------------
28
29 % Frequency axis
30 Freq_ax = cat(1, TMP1(:,1), TMP2(:,1), TMP3(:,1), TMP4(:,1));
31
32 for k = 1:1:5000;  % iteration for correction
33
34 for j = 2:LT_ax;
35
```

```
36 d1_2    = TMP1(31:32,j) - TMP2(1:2,j);    d1_2 = mean (d1_2);
       d12 (j)  = d1_2;
37 d31_32 = TMP3(1:2,j) - TMP2(31:32,j);    d31_32 = mean (d31_32);
       d3132(j) = d31_32;
38 D1_2    = TMP3(31:32,j) - TMP4(1:2,j);    D1_2 = mean (D1_2);
       D12(j)   = D1_2;
39
40 end
41
42 for j = 2:LT_ax; % delay row
43     for i = 1:32; % pixel correction% delay row
44
45     TMP2(i,j) = TMP2(i,j) + d12(j)*((32-i)/32) + d3132(j)*(i/32);
46
47     TMP4(i,j) =  TMP4(i,j) + D12(j)*((32-i)/32);
48
49
50     end
51 end
52 %plot(TMP(:,1),TMP(:,2:12:LT_ax)); hold on
53 end
54
55 %TMP = cat(1,TMP1(2:33,1:j), TMP2(2:33,1:j), TMP3(2:33,1:j), TMP4
       (2:33,1:j));
56 TMP = cat(1,TMP1, TMP2, TMP3, TMP4);
57
58 plot(TMP(:,1),TMP(:,2:12:LT_ax),'-r');
59
60 h = size(TMP);
61 TMP(2:h(:,1)+1,1:h(:,2)) = TMP;
62 TMP(1,2:h(:,2)) = Time_ax;
63 save ([dr,fn,'_pix_corr_5000-test',ext],'TMP','-ASCII', '-tabs');
```

Bibliography

[1] T. van Oudheusden, E. F. de Jong, S. B. van der Geer, W. P. E. M. Op 't Root, O. J. Luiten, and B. J. Siwick. Electron source concept for single-shot sub-100 fs electron diffraction in the 100 keV range. *Journal of Applied Physics*, 102(9):093501, nov 2007.

[2] Alan R. Fersht. From the first protein structures to our current knowledge of protein folding: delights and scepticisms. *Nature Reviews Molecular Cell Biology*, 9(8):650–654, jun 2008.

[3] P. Bernado, L. Blanchard, P. Timmins, D. Marion, R. W. H. Ruigrok, and M. Blackledge. A structural model for unfolded proteins from residual dipolar couplings and small-angle x-ray scattering. *Proceedings of the National Academy of Sciences*, 102(47):17002–17007, nov 2005.

[4] Michael Woerner, Flavio Zamponi, Zunaira Ansari, Jens Dreyer, Benjamin Freyer, Mirabelle Prémont-Schwarz, and Thomas Elsaesser. Concerted electron and proton transfer in ionic crystals mapped by femtosecond x-ray powder diffraction. *The Journal of Chemical Physics*, 133(6):064509, aug 2010.

[5] Sebastian Doniach. Changes in biomolecular conformation seen by small angle x-ray scattering. *Chemical Reviews*, 101(6):1763–1778, jun 2001.

[6] Nora Bergmann, Sébastien Bonhommeau, Kathrin M. Lange, Stefanie M. Greil, Stefan Eisebitt, Frank de Groot, Majed Chergui, and Emad F. Aziz. On the enzy-

matic activity of catalase: an iron l-edge x-ray absorption study of the active centre. *Physical Chemistry Chemical Physics*, 12(18):4827, 2010.

[7] Anup L. Dadlani, Orlando Trejo, Shinjita Acharya, Jan Torgersen, Ioannis Petousis, Dennis Nordlund, Ritimukta Sarangi, Peter Schindler, and Fritz B. Prinz. Exploring the local electronic structure and geometric arrangement of ALD zn(o, s) buffer layers using x-ray absorption spectroscopy. *J. Mater. Chem. C*, 3(47):12192–12198, 2015.

[8] L. X. Chen, X. Zhang, and M. L. Shelby. Recent advances on ultrafast x-ray spectroscopy in the chemical sciences. *Chem. Sci.*, 5(11):4136–4152, 2014.

[9] Pramod Kumar Verma, Andreas Steinbacher, Alexander Schmiedel, Patrick Nuernberger, and Tobias Brixner. Excited-state intramolecular proton transfer of 2-acetylindan-1, 3-dione studied by ultrafast absorption and fluorescence spectroscopy. *Structural Dynamics*, 3(2):023606, mar 2016.

[10] Emil W. Fu, Paul P. Dymerski, and Robert C. Dunbar. The photodissociation and high resolution laser photodissociation of halogen-substituted toluene cations. *Journal of the American Chemical Society*, 98(2):337–342, jan 1976.

[11] Steven M. Arrivo, Thomas P. Dougherty, W.Tandy Grubbs, and Edwin J. Heilweil. Ultrafast infrared spectroscopy of vibrational CO-stretch up-pumping and relaxation dynamics of w(CO)6. *Chemical Physics Letters*, 235(3-4):247–254, mar 1995.

[12] Matthew J. Nee, Carlos R. Baiz, Jessica M. Anna, Robert McCanne, and Kevin J. Kubarych. Multilevel vibrational coherence transfer and wavepacket dynamics probed with multidimensional IR spectroscopy. *The Journal of Chemical Physics*, 129(8):084503, aug 2008.

[13] C. J. Fecko. Ultrafast hydrogen-bond dynamics in the infrared spectroscopy of water. *Science*, 301(5640):1698–1702, sep 2003.

[14] John C. Deàk, Stuart T. Rhea, Lawrence K. Iwaki, and Dana D. Dlott. Vibrational energy relaxation and spectral diffusion in water and deuterated water. *The Journal of Physical Chemistry A*, 104(21):4866–4875, jun 2000.

[15] Editor Michael D. Fayer. Ultrafast infrared vibrational spectroscopy. *CRC Press, Taylor & Francis Group*, March 2013.

[16] Janne Savolainen, Frank Uhlig, Saima Ahmed, Peter Hamm, and Pavel Jungwirth. Direct observation of the collapse of the delocalized excess electron in water. *Nature Chemistry*, 6(8):697–701, jul 2014.

[17] T. H. MAIMAN. Stimulated optical radiation in ruby. *Nature*, 187(4736):493–494, aug 1960.

[18] Franz X. Kärtner. Few-cycle laser pulse generation and its applications. *Springer*, 2004.

[19] M. Hentschel, R. Kienberger, Ch. Spielmann, G. A. Reider, N. Milosevic, T. Brabec, P. Corkum, U. Heinzmann, M. Drescher, and F. Krausz. Attosecond metrology. *Nature*, 414(6863):509–513, nov 2001.

[20] Oksana Graef. Phd thesis: Femtosecond photoelectron spectroscopy for observation of chemical reactions. *UniversitÃdt Kassel*, 2005.

[21] Régis Y. N. Gengler, Daniel S. Badali, Dongfang Zhang, Konstantinos Dimos, Konstantinos Spyrou, Dimitrios Gournis, and R. J. Dwayne Miller. Revealing the ultrafast process behind the photoreduction of graphene oxide. *Nature Communications*, 4, oct 2013.

[22] Pradeep Kumar, Sungho Han, and H Eugene Stanley. Anomalies of water and hydrogen bond dynamics in hydrophobic nanoconfinement. *Journal of Physics: Condensed Matter*, 21(50):504108, nov 2009.

[23] Buchsteiner, Anton Lerf, and Jörg Pieper. Water dynamics in graphite oxide investigated with neutron scattering. *The Journal of Physical Chemistry B*, 110(45):22328–22338, nov 2006.

[24] Marie-Claire Bellissent-Funel, Ali Hassanali, Martina Havenith, Richard Henchman, Peter Pohl, Fabio Sterpone, David van der Spoel, Yao Xu, and Angel E Garcia. Water determines the structure and dynamics of proteins. *Chemical Reviews*, 116(13):7673–7697, jul 2016.

[25] J. J. Gilijamse, A. J. Lock, and H. J. Bakker. Dynamics of confined water molecules. *Proceedings of the National Academy of Sciences*, 102(9):3202–3207, feb 2005.

[26] Adriaan M. Dokter, Sander Woutersen, and Huib J. Bakker. Anomalous slowing down of the vibrational relaxation of liquid water upon nanoscale confinement. *Physical Review Letters*, 94(17), may 2005.

[27] Yutaka Nagasawa. Ultrafast photon echo experiments in condensed phase: Detection of solvation dynamics, coherent wavepacket motions and static inhomogeneity. *Journal of Photochemistry and Photobiology C: Photochemistry Reviews*, 12(1):31–45, mar 2011.

[28] M. L. Cowan, B. D. Bruner, N. Huse, J. R. Dwyer, B. Chugh, E. T. J. Nibbering, T. Elsaesser, and R. J. D. Miller. Ultrafast memory loss and energy redistribution in the hydrogen bond network of liquid h2o. *Nature*, 434(7030):199–202, mar 2005.

[29] Shaul Mukamel. Principles of nonlinearoptics. *Oxford University Press, Inc.*, ISBN-13: 978-0195132915, 1995.

[30] Robert W. Boyd. Nonliar optics. *Elsevier Inc.*, ISBN:978-0-12-369470-6, 2008.

[31] Nils Huse. Multidimensional vibrational spectroscopy of hydrogen-bonded systems in the liquid phase: Coupling mechanisms and structural dynamics. *Humboldt-Universität zu Berlin*, Ph.D Thesis, 2006.

[32] John David Jackson. Classical electrodynamics. *John Wiley & Sons, Inc.*, 1962.

[33] Peter Hamm. Principles of nonlinear optical spectroscopy: A practical approach, lectures of virtual european university on lasers, marie curie chair virtual university on laser science: Lectures, 2010-08-06. 2005.

[34] P. Hamm. Coherent effects in femtosecond infrared spectroscopy. *Chemical Physics*, 200(3):415–429, nov 1995.

[35] A. Einstein. The quantum theory of radiation. *Physikalische Zeitschrift*, **18**, 121, March 1917.

[36] J. P. Gordon, H. J. Zeiger, and C. H. Townes. The maser—new type of microwave amplifier, frequency standard, and spectrometer. *Phys. Rev.*, 99:1264–1274, Aug 1955.

[37] F. J. McClung and R. W. Hellwarth. Giant optical pulsations from ruby. *Journal of Applied Physics*, 33(3):828–829, 1962.

[38] J. A. Armstrong. Measurement of picosecond laser pulse widths. *Applied Physics Letters*, 10(1):16–18, 1967.

[39] E. P. Ippen and C. V. Shank. Dynamic spectroscopy and subpicosecond pulse compression. *Applied Physics Letters*, 27(9):488–490, 1975.

[40] J.-C. Diels, E. Van Stryland, and G. Benedict. Generation and measurement of 200 femtosecond optical pulses. *Optics Communications*, 25(1):93 – 96, 1978.

[41] R. L. Fork, B. I. Greene, and C. V. Shank. Generation of optical pulses shorter than 0.1 psec by colliding pulse mode locking. *Applied Physics Letters*, 38(9):671–672, 1981.

[42] A. Baltuska et al. Attosecond control of electronic processes by intense light fields. *Nature*, *421*, 611, 2003.

[43] Donna Strickland and Gerard Mourou. Compression of amplified chirped optical pulses. *Optics Communications*, 56(3):219 – 221, 1985.

[44] P. F. Moulton. Spectroscopic and laser characteristics of ti:al2o3. *J. Opt. Soc. Am. B*, 3(1):125–133, Jan 1986.

[45] P. Albers, E. Stark, and G. Huber. Continuous-wave laser operation and quantum efficiency of titanium-doped sapphire. *J. Opt. Soc. Am. B*, 3(1):134–139, Jan 1986.

[46] T. Wilhelm, J. Piel, and E. Riedle. Sub-20-fs pulses tunable across the visible from a blue-pumped single-pass noncollinear parametric converter. *Opt. Lett.*, 22(19):1494–1496, Oct 1997.

[47] Ida Z. Kozma, Peter Baum, Stefan Lochbrunner, and Eberhard Riedle. Widely tunable sub-30 fs ultraviolet pulses by chirped sum frequency mixing. *Opt. Express*, 11(23):3110–3115, Nov 2003.

[48] Robert A. Kaindl, Matthias Wurm, Klaus Reimann, Peter Hamm, Andrew M. Weiner, and Michael Woerner. Generation, shaping, and characterization of intense femtosecond pulses tunable from 3 to 20 µm. *J. Opt. Soc. Am. B*, 17(12):2086–2094, Dec 2000.

[49] Extending opportunities. *Nature Photonics*, 6(7):407–407, jun 2012.

[50] D. E. Spence, P. N. Kean, and W. Sibbett. 60-fsec pulse generation from a self-mode-locked ti:sapphire laser. *Optics Letters*, 16(1):42, jan 1991.

[51] Bob Proctor, Erik Westwig, and Frank Wise. Characterization of a kerr-lens mode-locked ti:sapphire laser with positive group-velocity dispersion. *Optics Letters*, 18(19):1654, oct 1993.

[52] Richard L. Sutherland. Handbook of nonlinear optics. *CRC Press Taylor & Francis Group*, 2003.

[53] Katrin Adamczyk PhD Thesis. Ultrafast charge transfer processes in solution. *Humboldt-UniversitÃdt zu Berlin*, 2010.

[54] Wu Hong Wang Yan-Ling, Zhou Xu-Gui and Ding Liang-En. Efficient collinear frequency tripling of femtosecond laser with compensation of group velocity delay. *IOP SCIENCE*, 18(10):1654, 2009.

[55] Audrius Dubietis, Gintaras TamoÅąauskas, Rosvaldas ÅăuminasÅăuminas, Vytautas Jukna, and Arnaud Couairon. Ultrafast supercontinuum generation in bulk condensed media (invited review). *arXiv:1706.04356*, jun 2017.

[56] B. C. Brodie. On the atomic weight of graphite. *Philosophical Transactions of the Royal Society of London*, 149(0):249–259, jan 1859.

[57] William S. Hummers and Richard E. Offeman. Preparation of graphitic oxide. *Journal of the American Chemical Society*, 80(6):1339–1339, mar 1958.

[58] L. Staudenmaier. Verfahren zur darstellung der graphitsÃ̆dure. *Ber. Dtsch. Chem. Ges.*, 31:1481, 1898.

[59] Daniela C. Marcano, Dmitry V. Kosynkin, Jacob M. Berlin, Alexander Sinitskii, Zhengzong Sun, Alexander Slesarev, Lawrence B. Alemany, Wei Lu, and James M. Tour. Improved synthesis of graphene oxide. *ACS Nano*, 4(8):4806–4814, aug 2010.

[60] Muge Acik and Yves J Chabal. A review on reducing graphene oxide for band gap engineering. *Journal of Materials Science Research*, 2(1), dec 2012.

[61] Cui Zhang, Daniel M. Dabbs, Li-Min Liu, Ilhan A. Aksay, Roberto Car, and Annabella Selloni. Combined effects of functional groups, lattice defects, and edges in the infrared spectra of graphene oxide. *The Journal of Physical Chemistry C*, 119(32):18167–18176, aug 2015.

[62] Edgar Jimenez-Cervantes, Juventino López-Barroso, Ana Laura Martínez-Hernández, and Carlos Velasco-Santos. Graphene-based materials functionalization with natural polymeric biomolecules. In *Recent Advances in Graphene Research*. InTech, oct 2016.

[63] P. R. Wallace. The band theory of graphite. *Physical Review*, 71(9):622–634, may 1947.

[64] Nathan O. Weiss, Hailong Zhou, Lei Liao, Yuan Liu, Shan Jiang, Yu Huang, and Xiangfeng Duan. Graphene: An emerging electronic material. *Advanced Materials*, 24(43):5782–5825, aug 2012.

[65] Neil R. Wilson, Priyanka A. Pandey, Richard Beanland, Robert J. Young, Ian A. Kinloch, Lei Gong, Zheng Liu, Kazu Suenaga, Jonathan P. Rourke, Stephen J. York,

and Jeremy Sloan. Graphene oxide: Structural analysis and application as a highly transparent support for electron microscopy. *ACS Nano*, 3(9):2547–2556, sep 2009.

[66] D. Pandey, R. Reifenberger, and R. Piner. Scanning probe microscopy study of exfoliated oxidized graphene sheets. *Surface Science*, 602(9):1607–1613, may 2008.

[67] Siegfried Eigler, Christoph Dotzer, Ferdinand Hof, Walter Bauer, and Andreas Hirsch. Sulfur species in graphene oxide. *Chemistry - A European Journal*, 19(29):9490–9496, jun 2013.

[68] Jaeseok Kim, Juyeong Oh, Chihun In, Yun-Shik Lee, Theodore B. Norris, Seong Chan Jun, and Hyunyong Choi. Unconventional terahertz carrier relaxation in graphene oxide: Observation of enhanced auger recombination due to defect saturation. *ACS Nano*, 8(3):2486–2494, mar 2014.

[69] Sreejith Kaniyankandy, S. N. Achary, Sachin Rawalekar, and Hirendra N. Ghosh. Ultrafast relaxation dynamics in graphene oxide: Evidence of electron trapping. *The Journal of Physical Chemistry C*, 115(39):19110–19116, oct 2011.

[70] Yan Shen, Songbo Yang, Peng Zhou, Qingqing Sun, Pengfei Wang, Li Wan, Jing Li, Liangyao Chen, Xianbao Wang, Shijin Ding, and David Wei Zhang. Evolution of the band-gap and optical properties of graphene oxide with controllable reduction level. *Carbon*, 62:157–164, oct 2013.

[71] F. Barroso-Bujans, S. Cerveny, R. Verdejo, J.J. del Val, J.M. Alberdi, A. Alegría, and J. Colmenero. Permanent adsorption of organic solvents in graphite oxide and its effect on the thermal exfoliation. *Carbon*, 48(4):1079–1087, apr 2010.

[72] Markus Breusing, Claus Ropers, and Thomas Elsaesser. Ultrafast carrier dynamics in graphite. *Physical Review Letters*, 102(8), feb 2009.

[73] Guichuan Xing, Hongchen Guo, Xinhai Zhang, Tze Chien Sum, and Cheng Hon Alfred Huan. The physics of ultrafast saturable absorption in graphene. *Optics Express*, 18(5):4564, feb 2010.

[74] Chun Hung Lui, Kin Fai Mak, Jie Shan, and Tony F. Heinz. Ultrafast photoluminescence from graphene. *Physical Review Letters*, 105(12), sep 2010.

[75] Jhih-An Yang, Stephen Parham, Daniel Dessau, and Dmitry Reznik. Novel electron-phonon relaxation pathway in graphite revealed by time-resolved raman scattering and angle-resolved photoemission spectroscopy. *Scientific Reports*, 7:40876, jan 2017.

[76] Kwangu Kang, Daner Abdula, David G. Cahill, and Moonsub Shim. Lifetimes of optical phonons in graphene and graphite by time-resolved incoherent anti-stokes raman scattering. *Physical Review B*, 81(16), apr 2010.

[77] Zhi-Bo Liu, Xin Zhao, Xiao-Liang Zhang, Xiao-Qing Yan, Ying-Peng Wu, Yong-Sheng Chen, and Jian-Guo Tian. Ultrafast dynamics and nonlinear optical responses from sp2- and sp3-hybridized domains in graphene oxide. *The Journal of Physical Chemistry Letters*, 2(16):1972–1977, aug 2011.

[78] Libai Huang, Gregory V. Hartland, Li-Qiang Chu, Luxmi, Randall M. Feenstra, Chuanxin Lian, Kristof Tahy, and Huili Xing. Ultrafast transient absorption microscopy studies of carrier dynamics in epitaxial graphene. *Nano Letters*, 10(4):1308–1313, apr 2010.

[79] Jingzhi Shang, Ting Yu, Jianyi Lin, and Gagik G. Gurzadyan. Ultrafast electron-optical phonon scattering and quasiparticle lifetime in CVD-grown graphene. *ACS Nano*, 5(4):3278–3283, apr 2011.

[80] Dong Sun, Zong-Kwei Wu, Charles Divin, Xuebin Li, Claire Berger, Walt A. de Heer, Phillip N. First, and Theodore B. Norris. Ultrafast relaxation of excited dirac fermions in epitaxial graphene using optical differential transmission spectroscopy. *Physical Review Letters*, 101(15), oct 2008.

[81] A. C. Betz, F. Vialla, D. Brunel, C. Voisin, M. Picher, A. Cavanna, A. Madouri, G. Fève, J.-M. Berroir, B. Plaçais, and E. Pallecchi. Hot electron cooling by acoustic phonons in graphene. *Physical Review Letters*, 109(5), aug 2012.

[82] Denis L Nika and Alexander A Balandin. Two-dimensional phonon transport in graphene. *Journal of Physics: Condensed Matter*, 24(23):233203, may 2012.

[83] Haining Wang, Jared H. Strait, Paul A. George, Shriram Shivaraman, Virgil B. Shields, Mvs Chandrashekhar, Jeonghyun Hwang, Farhan Rana, Michael G. Spencer, Carlos S. Ruiz-Vargas, and Jiwoong Park. Ultrafast relaxation dynamics of hot optical phonons in graphene. *Applied Physics Letters*, 96(8):081917, feb 2010.

[84] Jingzhi Shang, Suxia Yan, Chunxiao Cong, Howe-Siang Tan, Ting Yu, and Gagik G. Gurzadyan. Probing near dirac point electron-phonon interaction in graphene. *Optical Materials Express*, 2(12):1713, nov 2012.

[85] Andrea Tomadin, Daniele Brida, Giulio Cerullo, Andrea C. Ferrari, and Marco Polini. Nonequilibrium dynamics of photoexcited electrons in graphene: Collinear scattering, auger processes, and the impact of screening. *Physical Review B*, 88(3), jul 2013.

[86] D. Brida, A. Tomadin, C. Manzoni, Y. J. Kim, A. Lombardo, S. Milana, R. R. Nair, K. S. Novoselov, A. C. Ferrari, G. Cerullo, and M. Polini. Ultrafast collinear scattering and carrier multiplication in graphene. *Nature Communications*, 4, jun 2013.

[87] Long Ju, Baisong Geng, Jason Horng, Caglar Girit, Michael Martin, Zhao Hao, Hans A. Bechtel, Xiaogan Liang, Alex Zettl, Y. Ron Shen, and Feng Wang. Graphene plasmonics for tunable terahertz metamaterials. *Nature Nanotechnology*, 6(10):630–634, sep 2011.

[88] Kai Yang, Shuchang Liu, Sara Arezoomandan, Ajay Nahata, and Berardi Sensale-Rodriguez. Graphene-based tunable metamaterial terahertz filters. *Applied Physics Letters*, 105(9):093105, sep 2014.

[89] Z. Fei, A. S. Rodin, G. O. Andreev, W. Bao, A. S. McLeod, M. Wagner, L. M. Zhang, Z. Zhao, M. Thiemens, G. Dominguez, M. M. Fogler, A. H. Castro Neto,

C. N. Lau, F. Keilmann, and D. N. Basov. Gate-tuning of graphene plasmons revealed by infrared nano-imaging. *Nature*, jun 2012.

[90] Marco Polini, Reza Asgari, Giovanni Borghi, Yafis Barlas, T. Pereg-Barnea, and A. H. MacDonald. Plasmons and the spectral function of graphene. *Physical Review B*, 77(8), feb 2008.

[91] H Pfnür, T Langer, J Baringhaus, and C Tegenkamp. Multiple plasmon excitations in adsorbed two-dimensional systems. *Journal of Physics: Condensed Matter*, 23(11):112204, mar 2011.

[92] Farhan Rana, Jared H. Strait, Haining Wang, and Christina Manolatou. Ultrafast carrier recombination and generation rates for plasmon emission and absorption in graphene. *Physical Review B*, 84(4), jul 2011.

[93] Chun Hung Lui, Kin Fai Mak, Jie Shan, and Tony F. Heinz. Ultrafast photoluminescence from graphene. *Physical Review Letters*, 105(12), sep 2010.

[94] Wei-Tao Liu, S. W. Wu, P. J. Schuck, M. Salmeron, Y. R. Shen, and F. Wang. Nonlinear broadband photoluminescence of graphene induced by femtosecond laser irradiation. *Physical Review B*, 82(8), aug 2010.

[95] Donghe Du, Haiou Song, Yuting Nie, Xuhui Sun, Lei Chen, and Jianyong Ouyang. Photoluminescence of graphene oxide in visible range arising from excimer formation. *The Journal of Physical Chemistry C*, 119(34):20085–20090, aug 2015.

[96] Colin Hong An Wong and Martin Pumera. Stripping voltammetry at chemically modified graphenes. *RSC Advances*, 2(14):6068, 2012.

[97] Jianchang Li, Xiangqiong Zeng, Tianhui Ren, and Emile van der Heide. The preparation of graphene oxide and its derivatives and their application in bio-tribological systems. *Lubricants*, 2(3):137–161, sep 2014.

[98] Tayyebeh Soltani and Byeong-Kyu Lee. A benign ultrasonic route to reduced graphene oxide from pristine graphite. *Journal of Colloid and Interface Science*, 486:337–343, jan 2017.

[99] M. Acik, G. Lee, C. Mattevi, M. Chhowalla, K. Cho, and Y. J. Chabal. Unusual infrared-absorption mechanism in thermally reduced graphene oxide. *Nature Materials*, 9(10):840–845, sep 2010.

[100] Muge Acik, Geunsik Lee, Cecilia Mattevi, Adam Pirkle, Robert M. Wallace, Manish Chhowalla, Kyeongjae Cho, and Yves Chabal. The role of oxygen during thermal reduction of graphene oxide studied by infrared absorption spectroscopy. *The Journal of Physical Chemistry C*, 115(40):19761–19781, oct 2011.

[101] Akshay Mathkar, Dylan Tozier, Paris Cox, Peijie Ong, Charudatta Galande, Kaushik Balakrishnan, Arava Leela Mohana Reddy, and Pulickel M. Ajayan. Controlled, stepwise reduction and band gap manipulation of graphene oxide. *The Journal of Physical Chemistry Letters*, 3(8):986–991, apr 2012.

[102] Shun Mao, Haihui Pu, and Junhong Chen. Graphene oxide and its reduction: modeling and experimental progress. *RSC Advances*, 2(7):2643, 2012.

[103] Daniel R. Dreyer, Sungjin Park, Christopher W. Bielawski, and Rodney S. Ruoff. The chemistry of graphene oxide. *Chem. Soc. Rev.*, 39(1):228–240, 2010.

[104] Péter Forgó Katalin Josepovits Yiannis Sanakis Dimitris Petridis Tamas Szabó, OttÃş Berkesi and Imre DÃľkÃąny. Evolution of surface functional groups in a series of progressively oxidized graphite oxides. *Chem. Mater.*, 18:2740–2749, 2006.

[105] Jia-An Yan and M. Y. Chou. Oxidation functional groups on graphene: Structural and electronic properties. *Physical Review B*, 82(12), sep 2010.

[106] E. C. Mattson, J. E. Johns, K. Pande, R. A. Bosch, S. Cui, M. Gajdardziska-Josifovska, M. Weinert, J. H. Chen, M. C. Hersam, and C. J. Hirschmugl. Vibrational excitations and low-energy electronic structure of epoxide-decorated graphene. *The Journal of Physical Chemistry Letters*, 5(1):212–219, jan 2014.

[107] K. Andre Mkhoyan, Alexander W. Contryman, John Silcox, Derek A. Stewart, Goki Eda, Cecilia Mattevi, Steve Miller, and Manish Chhowalla. Atomic and electronic structure of graphene-oxide. *Nano Letters*, 9(3):1058–1063, mar 2009.

[108] Kian Ping Loh, Qiaoliang Bao, Goki Eda, and Manish Chhowalla. Graphene oxide as a chemically tunable platform for optical applications. *Nature Chemistry*, 2(12):1015–1024, nov 2010.

[109] Mark Lundie, Željko Šljivančanin, and Stanko Tomić. Analysis of energy gap opening in graphene oxide. *Journal of Physics: Conference Series*, 526:012003, jun 2014.

[110] R Maiti, A Midya, C Narayana, and S K Ray. Tunable optical properties of graphene oxide by tailoring the oxygen functionalities using infrared irradiation. *Nanotechnology*, 25(49):495704, nov 2014.

[111] Eilho Jung, Seokbae Lee, Seulki Roh, Eunhee Hwang, Junghyun Lee, Hyoyoung Lee, and Jungseek Hwang. Optical properties of graphite oxide and reduced graphite oxide. *Journal of Physics D: Applied Physics*, 47(26):265306, jun 2014.

[112] Pengzhan Sun, Yanlei Wang, He Liu, Kunlin Wang, Dehai Wu, Zhiping Xu, and Hongwei Zhu. Structure evolution of graphene oxide during thermally driven phase transformation: Is the oxygen content really preserved? *PLoS ONE*, 9(11):e111908, nov 2014.

[113] Qin Pan, Ching-Chang Chung, Nanfei He, Jacob L. Jones, and Wei Gao. Accelerated thermal decomposition of graphene oxide films in air via in-situ x-ray diffraction analysis. *The Journal of Physical Chemistry C*, 120(27):14984–14990, jul 2016.

[114] Zhengtang Luo, Patrick M. Vora, Eugene J. Mele, A. T. Charlie Johnson, and James M. Kikkawa. Photoluminescence and band gap modulation in graphene oxide. *Applied Physics Letters*, 94(11):111909, mar 2009.

[115] Goki Eda, Yun-Yue Lin, Cecilia Mattevi, Hisato Yamaguchi, Hsin-An Chen, I-Sheng Chen, Chun-Wei Chen, and Manish Chhowalla. Blue photoluminescence from chemically derived graphene oxide. *Advanced Materials*, 22(4):505–509, jan 2010.

[116] Annemarie L. Exarhos, Michael E. Turk, and James M. Kikkawa. Ultrafast spectral migration of photoluminescence in graphene oxide. *Nano Letters*, 13(2):344–349, feb 2013.

[117] Sesha Vempati and Tamer Uyar. Fluorescence from graphene oxide and the influence of ionic, π–π interactions and heterointerfaces: electron or energy transfer dynamics. *Phys. Chem. Chem. Phys.*, 16(39):21183–21203, aug 2014.

[118] Charudatta Galande, Aditya D. Mohite, Anton V. Naumov, Wei Gao, Lijie Ci, Anakha Ajayan, Hui Gao, Anchal Srivastava, R. Bruce Weisman, and Pulickel M. Ajayan. Quasi-molecular fluorescence from graphene oxide. *Scientific Reports*, 1(1), sep 2011.

[119] Jingzhi Shang, Lin Ma, Jiewei Li, Wei Ai, Ting Yu, and Gagik G. Gurzadyan. The origin of fluorescence from graphene oxide. *Scientific Reports*, 2, nov 2012.

[120] Scott K. Cushing, Ming Li, Fuqiang Huang, and Nianqiang Wu. Origin of strong excitation wavelength dependent fluorescence of graphene oxide. *ACS Nano*, 8(1):1002–1013, jan 2014.

[121] Wenjun He, Chengbing Qin, Zhixing Qiao, Guofeng Zhang, Liantuan Xiao, and Suotang Jia. Two fluorescence lifetime components reveal the photoreduction dynamics of monolayer graphene oxide. *Carbon*, 109:264–268, nov 2016.

[122] Lei Wang, Hai-Yu Wang, Yan Wang, Shou-Jun Zhu, Yong-Lai Zhang, Jun-Hu Zhang, Qi-Dai Chen, Wei Han, Huai-Liang Xu, Bai Yang, and Hong-Bo Sun. Direct observation of quantum-confined graphene-like states and novel hybrid states in graphene oxide by transient spectroscopy. *Advanced Materials*, 25(45):6539–6545, sep 2013.

[123] Xiaoming Wen, Pyng Yu, Yon-Rui Toh, Xiaotao Hao, and Jau Tang. Intrinsic and extrinsic fluorescence in carbon nanodots: Ultrafast time-resolved fluorescence and carrier dynamics. *Advanced Optical Materials*, 1(2):173–178, feb 2013.

[124] Volker Strauss, Johannes T. Margraf, Christian Dolle, Benjamin Butz, Thomas J. Nacken, Johannes Walter, Walter Bauer, Wolfgang Peukert, Erdmann Spiecker, Timothy Clark, and Dirk M. Guldi. Carbon nanodots: Toward a comprehensive understanding of their photoluminescence. *Journal of the American Chemical Society*, 136(49):17308–17316, dec 2014.

[125] Lixia Zhao, Fan Di, Dabin Wang, Liang-Hong Guo, Yu Yang, Bin Wan, and Hui Zhang. Chemiluminescence of carbon dots under strong alkaline solutions: a novel insight into carbon dot optical properties. *Nanoscale*, 5(7):2655, 2013.

[126] Geeta Sharma and S.W. Gosavi. Thermoluminescence properties of graphene–nano ZnS composite. *Journal of Luminescence*, 145:557–562, jan 2014.

[127] A. Lerf, A. Buchsteiner, J. Pieper, S. Schöttl, I. Dekany, T. Szabo, and H.P. Boehm. Hydration behavior and dynamics of water molecules in graphite oxide. *Journal of Physics and Chemistry of Solids*, 67(5-6):1106–1110, may 2006.

[128] Sanket A. Deshmukh, Ganesh Kamath, Gary A. Baker, Anirudha V. Sumant, and Subramanian K.R.S. Sankaranarayanan. The interfacial dynamics of water sandwiched between graphene sheets are governed by the slit width. *Surface Science*, 609:129–139, mar 2013.

[129] S. Zhou, S. Kim, E. Di Gennaro, Y. Hu, C. Gong, X. Lu, C. Berger, W. de Heer, E. Riedo, Y. J. Chabal, C. Aruta, and A. Bongiorno. Film structure of epitaxial graphene oxide on SiC: Insight on the relationship between interlayer spacing, water content, and intralayer structure. *Advanced Materials Interfaces*, 1(3):1300106, feb 2014.

[130] Shujie You, Junchun Yu, Bertil Sundqvist, L. A. Belyaeva, Natalya V. Avramenko, Mikhail V. Korobov, and Alexandr V. Talyzin. Selective intercalation of graphite oxide by methanol in water/methanol mixtures. *The Journal of Physical Chemistry C*, 117(4):1963–1968, jan 2013.

[131] Nikhil V. Medhekar, Ashwin Ramasubramaniam, Rodney S. Ruoff, and Vivek B. Shenoy. Hydrogen bond networks in graphene oxide composite paper: Structure and mechanical properties. *ACS Nano*, 4(4):2300–2306, apr 2010.

[132] Owen C. Compton, Steven W. Cranford, Karl W. Putz, Zhi An, L. Catherine Brinson, Markus J. Buehler, and SonBinh T. Nguyen. Tuning the mechanical properties of graphene oxide paper and its associated polymer nanocomposites by controlling cooperative intersheet hydrogen bonding. *ACS Nano*, 6(3):2008–2019, mar 2012.

[133] Daeok Kim, Dae Woo Kim, Hyung-Kyu Lim, Jiwon Jeon, Hyungjun Kim, Hee-Tae Jung, and Huen Lee. Intercalation of gas molecules in graphene oxide interlayer: The role of water. *The Journal of Physical Chemistry C*, 118(20):11142–11148, may 2014.

[134] K. Rohini, Daniel M. R. Sylvinson, and R. S. Swathi. Intercalation of HF, h2o, and NH3 clusters within the bilayers of graphene and graphene oxide: Predictions from coronene-based model systems. *The Journal of Physical Chemistry A*, 119(44):10935–10945, nov 2015.

[135] Xin Zhao, Zhi-Bo Liu, Wei-Bo Yan, Yingpeng Wu, Xiao-Liang Zhang, Yongsheng Chen, and Jian-Guo Tian. Ultrafast carrier dynamics and saturable absorption of solution-processable few-layered graphene oxide. *Applied Physics Letters*, 98(12):121905, mar 2011.

[136] Qun Zhang, Hongjun Zheng, Zhigang Geng, Shenlong Jiang, Jing Ge, Kaili Fan, Sai Duan, Yang Chen, Xiaoping Wang, and Yi Luo. The realistic domain structure of as-synthesized graphene oxide from ultrafast spectroscopy. *Journal of the American Chemical Society*, 135(33):12468–12474, aug 2013.

[137] Brian A. Ruzicka, Lalani K. Werake, Hui Zhao, Shuai Wang, and Kian Ping Loh. Femtosecond pump-probe studies of reduced graphene oxide thin films. *Applied Physics Letters*, 96(17):173106, apr 2010.

[138] Sunil Kumar, N. Kamaraju, K.S. Vasu, Angshuman Nag, A.K. Sood, and C.N.R. Rao. Graphene analogue BCN: Femtosecond nonlinear optical susceptibility and hot carrier dynamics. *Chemical Physics Letters*, 499(1-3):152–157, oct 2010.

[139] Brian A. Ruzicka, Nardeep Kumar, Shuai Wang, Kian Ping Loh, and Hui Zhao. Two-probe study of hot carriers in reduced graphene oxide. *Journal of Applied Physics*, 109(8):084322, apr 2011.

[140] J. T. Hong, K. M. Lee, B. H. Son, S. J. Park, D. J. Park, Ji-Yong Park, Soonil Lee, and Y. H. Ahn. Terahertz conductivity of reduced graphene oxide films. *Optics Express*, 21(6):7633, mar 2013.

[141] Xiao Xing, Litao Zhao, Zeyu Zhang, Liang Fang, Zhengfu Fan, Xiumei Liu, Xian Lin, Jianhua Xu, Jinquan Chen, Xinluo Zhao, Zuanming Jin, and Guohong Ma. Photoinduced terahertz conductivity and carrier relaxation in thermal-reduced multilayer graphene oxide films. *The Journal of Physical Chemistry C*, 121(4):2451–2458, jan 2017.

[142] Dongwook Lee, Xingquan Zou, Xi Zhu, J. W. Seo, Jacqueline M. Cole, Federica Bondino, Elena Magnano, Saritha K. Nair, and Haibin Su. Ultrafast carrier phonon dynamics in NaOH-reacted graphite oxide film. *Applied Physics Letters*, 101(2):021604, jul 2012.

[143] Shangchao Lin and Markus J. Buehler. Thermal transport in monolayer graphene oxide: Atomistic insights into phonon engineering through surface chemistry. *Carbon*, 77:351–359, oct 2014.

[144] Yong Gang Wang, Hou Ren Chen, Xiao Ming Wen, Wen Feng Hsieh, and Jau Tang. A highly efficient graphene oxide absorber for q -switched nd:GdVO 4 lasers. *Nanotechnology*, 22(45):455203, oct 2011.

[145] Grzegorz Sobon, Jaroslaw Sotor, Joanna Jagiello, Rafal Kozinski, Mariusz Zdrojek, Marcin Holdynski, Piotr Paletko, Jakub Boguslawski, Ludwika Lipinska, and

Krzysztof M. Abramski. Graphene oxide vs reduced graphene oxide as saturable absorbers for er-doped passively mode-locked fiber laser. *Optics Express*, 20(17):19463, aug 2012.

[146] Chin Yong Neo and Jianyong Ouyang. Graphene oxide as auxiliary binder for TiO2 nanoparticle coating to more effectively fabricate dye-sensitized solar cells. *Journal of Power Sources*, 222:161–168, jan 2013.

[147] Remya Narayanan, Melepurath Deepa, and Avanish Kumar Srivastava. Nanoscale connectivity in a TiO2/CdSe quantum dots/functionalized graphene oxide nanosheets/au nanoparticles composite for enhanced photoelectrochemical solar cell performance. *Phys. Chem. Chem. Phys.*, 14(2):767–778, 2012.

[148] Goki Eda, Giovanni Fanchini, and Manish Chhowalla. Large-area ultrathin films of reduced graphene oxide as a transparent and flexible electronic material. *Nature Nanotechnology*, 3(5):270–274, apr 2008.

[149] R. K. Joshi, P. Carbone, F. C. Wang, V. G. Kravets, Y. Su, I. V. Grigorieva, H. A. Wu, A. K. Geim, and R. R. Nair. Precise and ultrafast molecular sieving through graphene oxide membranes. *Science*, 343(6172):752–754, feb 2014.

[150] Kian Ping Loh, Qiaoliang Bao, Goki Eda, and Manish Chhowalla. Graphene oxide as a chemically tunable platform for optical applications. *Nature Chemistry*, 2(12):1015–1024, nov 2010.

[151] Partha Khanra, Tapas Kuila, Nam Hoon Kim, Seon Hyeong Bae, Dong sheng Yu, and Joong Hee Lee. Simultaneous bio-functionalization and reduction of graphene oxide by bakers yeast. *Chemical Engineering Journal*, 183:526–533, feb 2012.

[152] Dan Li, Marc B. Müller, Scott Gilje, Richard B. Kaner, and Gordon G. Wallace. Processable aqueous dispersions of graphene nanosheets. *Nature Nanotechnology*, 3(2):101–105, jan 2008.

[153] Héctor A. Becerril, Jie Mao, Zunfeng Liu, Randall M. Stoltenberg, Zhenan Bao, and Yongsheng Chen. Evaluation of solution-processed reduced graphene oxide films as transparent conductors. *ACS Nano*, 2(3):463–470, mar 2008.

[154] R. R. Nair, P. Blake, A. N. Grigorenko, K. S. Novoselov, T. J. Booth, T. Stauber, N. M. R. Peres, and A. K. Geim. Fine structure constant defines visual transparency of graphene. *Science*, 320(5881):1308–1308, 2008.

[155] Akbar Bagri, Cecilia Mattevi, Muge Acik, Yves J. Chabal, Manish Chhowalla, and Vivek B. Shenoy. Structural evolution during the reduction of chemically derived graphene oxide. *Nature Chemistry*, 2(7):581–587, jun 2010.

[156] Karthikeyan Krishnamoorthy, Murugan Veerapandian, Kyusik Yun, and S.-J. Kim. The chemical and structural analysis of graphene oxide with different degrees of oxidation. *Carbon*, 53:38–49, mar 2013.

[157] Tamás Szabó, Ottó Berkesi, and Imre Dékány. DRIFT study of deuterium-exchanged graphite oxide. *Carbon*, 43(15):3186–3189, dec 2005.

[158] Thomas Limmer. InïňĆuence of carrier density on the ultrafast optical response of graphene and few-layer graphenes. *Ludwig Maximilian University Munich*, PhD Thesis 2012.

[159] Jenée D. Cyran, Jacob M. Nite, and Amber T. Krummel. Characterizing anharmonic vibrational modes of quinones with two-dimensional infrared spectroscopy. *The Journal of Physical Chemistry B*, 119(29):8917–8925, 2015. PMID: 25697689.

[160] Muge Acik and Yves J Chabal. A review on reducing graphene oxide for band gap engineering. *Journal of Materials Science Research*, 2(1), dec 2012.

[161] Aaron L. Stancik and Eric B. Brauns. A simple asymmetric lineshape for fitting infrared absorption spectra. *Vibrational Spectroscopy*, 47(1):66 – 69, 2008.

[162] J. C. Tsang, M. Freitag, V. Perebeinos, J. Liu, and Ph. Avouris. Doping and phonon renormalization in carbon nanotubes. *Nature Nanotechnology*, 2, 10 2007.

[163] Hugen Yan, Daohua Song, Kin Fai Mak, Ioannis Chatzakis, Janina Maultzsch, and Tony F. Heinz. Time-resolved raman spectroscopy of optical phonons in graphite: Phonon anharmonic coupling and anomalous stiffening. *Phys. Rev. B*, 80:121403, Sep 2009.

[164] Jun Yan, Yuanbo Zhang, Philip Kim, and Aron Pinczuk. Electric field effect tuning of electron-phonon coupling in graphene. *Phys. Rev. Lett.*, 98:166802, Apr 2007.

[165] Jingzhi Shang, Lin Ma, Jiewei Li, Wei Ai, Ting Yu, and Gagik G Gurzadyan. Femtosecond pump–probe spectroscopy of graphene oxide in water. *Journal of Physics D: Applied Physics*, 47(9):094008, feb 2014.

[166] Palak Dugar, Mahesh Kumar, Shibin Krishna T. C., Neha Aggarwal, and Govind Gupta. Carrier relaxation dynamics in defect states of epitaxial gan/aln/si using ultrafast transient absorption spectroscopy. *RSC Adv.*, 5:83969–83975, 2015.

[167] Jahan M. Dawlaty, Shriram Shivaraman, Mvs Chandrashekhar, Farhan Rana, and Michael G. Spencer. Measurement of ultrafast carrier dynamics in epitaxial graphene. *Applied Physics Letters*, 92(4):042116, jan 2008.

[168] Ryan W. Newson, Jesse Dean, Ben Schmidt, and Henry M. van Driel. Ultrafast carrier kinetics in exfoliated graphene and thin graphite films. *Optics Express*, 17(4):2326, feb 2009.

[169] E. P. Ippen, D. J. Eilenberger, and R. W. Dixon. Picosecond pulse generation by passive mode locking of diode lasers. *Applied Physics Letters*, 37(3):267–269, aug 1980.

[170] M.N. Islam, E.R. Sunderman, C.E. Soccolich, I. Bar-Joseph, N. Sauer, T.Y. Chang, and B.I. Miller. Color center lasers passively mode locked by quantum wells. *IEEE Journal of Quantum Electronics*, 25(12):2454–2463, 1989.

[171] S. Tsuda, W.H. Knox, S.T. Cundiff, W.Y. Jan, and J.E. Cunningham. Mode-locking ultrafast solid-state lasers with saturable bragg reflectors. *IEEE Journal of Selected Topics in Quantum Electronics*, 2(3):454–464, 1996.

[172] U. Keller. Semiconductor nonlinearities for solid-state laser modelocking and q-switching in semiconductors and semimetals. Vol. 59A, edited by A.Kost and E. Garmire, Academic Press, Boston, 1999.

[173] V. Liverini, S. Schön, R. Grange, M. Haiml, S. C. Zeller, and U. Keller. Low-loss GaInNAs saturable absorber mode locking a 1.3-μm solid-state laser. *Applied Physics Letters*, 84(20):4002–4004, may 2004.

[174] Yule Zhang and Yanrui Zhao. Semiconductor saturable absorber mirror (sesam). *NLO, University of New Mexico*, Spring 2005.

[175] U. Keller, K.J. Weingarten, F.X. Kartner, D. Kopf, B. Braun, I.D. Jung, R. Fluck, C. Honninger, N. Matuschek, and J. Aus der Au. Semiconductor saturable absorber mirrors (SESAM's) for femtosecond to nanosecond pulse generation in solid-state lasers. *IEEE Journal of Selected Topics in Quantum Electronics*, 2(3):435–453, 1996.

[176] R. E. Nahory, M. A. Pollack, W. D. Johnston, and R. L. Barns. Band gap versus composition and demonstration of vegard's law for in1-xGaxAsyP1-y lattice matched to InP. *Applied Physics Letters*, 33(7):659–661, oct 1978.

[177] Jiun-Cheng Wang, Chi-Kuang Sun, and Juen-Kai Wang. Nonlinear pulse-shaping phenomena of semiconductor saturable absorber mirror. *Applied Physics Letters*, 89(23):231106, 2006.

[178] Krishna Murari. PhD Thesis, Hamburg University, Few-cycle high energy mid-infrared pulse from ho ylf laser. 2016.